

**Technoeconomic Analysis of Textured Surfaces for Improved Condenser  
Performance in Thermoelectric Power Plants**

Parisa Daghigh Shoaie

Thesis submitted to the faculty of the Virginia Polytechnic Institute and State University  
in partial fulfillment of the requirements for the degree of

Master of Science

In

Mechanical Engineering

Ranga Pitchumani, Chair

Ali Haghghat

Roop Mahajan

December 10, 2020

Falls Church, Virginia

Keywords: Condenser, Energy, Fouling, SLIPS, Superhydrophobic, Texturing,  
Thermoelectric, Water, Anti-corrosion, Drag, Ice, Fog, Condensation, Electrodeposition  
coating

# **Technoeconomic Analysis of Textured Surfaces for Improved Condenser Performance in Thermoelectric Power Plants**

Parisa Daghigh Shoaie

## **ABSTRACT**

Nonwetting surfaces including superhydrophobic (SHS) and liquid infused surfaces (SLIPS) exhibit diverse exceptional characteristics promoting numerous application opportunities. Engineered textured surfaces demonstrate multiple features including drag reduction, fouling reduction, corrosion resistance, anti-fogging, anti-icing, and condensation enhancement. Integrating these properties, nonwetting surfaces have shown significant potential in improving the efficiency of energy applications. The first part of the thesis work aims at developing a fundamental mathematical understanding of the wetting process on the solid surface followed by presenting fabrication methodologies specifically focused on metallic substrates. The second part of this thesis presents an exhaustive survey on recent advancements and researches about features of nonwetting surfaces that could be implemented in major industrial applications.

To establish how realistically these features could enhance the real-life applications, the third part of this work investigates the dynamic performance and economic benefits of using textured surfaces fabricated using an electrodeposition process for condenser tubes in thermoelectric power plants. The textured surfaces are expected to provide enhanced performance by deterring fouling and promoting dropwise condensation of the steam on the shell side. Using a thermal resistance network of a shell and tube condenser, detailed parametric studies are carried out to investigate the effect of various design parameters on the annual condenser performance measured in terms of its electric energy output of a representative 550 MW coal-fired power plant. A cost modeling tool and a new levelized cost of condenser (LCOC) metric have been developed to evaluate the economic and performance benefits of enhanced condenser designs. The LCOC is defined as the ratio of the lifetime cost of the condenser (and associated costs such as coating, operation & maintenance) to the total electric energy produced by the

thermoelectric power plant. The physical model is coupled with a numerical optimization method to identify the optimal design and operating parameters of the textured tubes that minimizes LCOC. Altogether, the study presents the first effort to construct and analyze enhanced condenser design with textured tube surfaces on annual thermoelectric power plant performance and compares it against the baseline condenser design with plain tubes.

# **Technoeconomic Analysis of Textured Surfaces for Improved Condenser Performance in Thermoelectric Power Plants**

Parisa Daghigh Shoaei

## **GENERAL AUDIENCE ABSTRACT**

Liquid repellent surfaces have attracted lots of attention due to their numerous promising characteristics including promoting condensation, drag reduction, prohibiting fouling/deposition, corrosion, and fog/dew harvesting. These attributes have the potential to inspire a variety of applications for these surfaces in power plants, automotive and aviation industries, oils/organic solvents clean-up, fuel cells, solar panels, membrane distillation, stone/concrete protection, surgical fabrics, and biological applications, to name a few. Some of these applications have reached their potential for real-life implementation and more are still at the research phase needing more experimental and fundamental studies to get them ready.

The first part of this study presents the fundamentals of wetting process. Next, fabrication methods for metallic surfaces have been explored to identify the most scalable and cost-effective approaches which could be administered in large scale industrial applications.

A comprehensive review of recent publications on features of nonwetting surfaces has been carried out and presented in the second part of this thesis. To establish how realistically these features could enhance the real-life applications a thermo-economic performance model is developed for a powerplant condenser in the third section. Through a simple and cost-effective electrodeposition process, the common condenser tubes are modified to achieve textured tubes with superhydrophobic properties. The influence of using textured tubes on the plant's performance and its economic benefits are investigated to predict the potential promises of nonwetting surfaces.

## ACKNOWLEDGEMENTS

I would like to express my appreciation to my advisor, Dr. Ranga Pitchumani, for presenting me with an opportunity to experience research in this exciting field and for providing guidance and feedback throughout this project. I would also like to thank my advisory committee, Dr. Roop Mahajan and Dr. Ali Haghghat for their assistance. I would also like to extend my sincere thanks to Dr. Karthik Nithyanandam for all the insightful discussions we had during our collaboration on this project. Furthermore, I very much appreciate all teachers I have had a chance to learn from during my program at Virginia Tech.

I am also grateful to my husband for believing in me, motivating me, and encouraging me in pursuing my goals. Reaching this milestone would not have been possible without my family and friends, they have always given me the much-needed boost and enjoyment and I value their companionship.

The study reported in this thesis is based upon work supported by the United States Department of Energy under Award Number DE-FE0031556.

# Table of Contents

|   |      |
|---|------|
| Table of Contents .....   | vi   |
| List of Figures .....   | viii |
| List of Tables.....   | ix   |
| Chapter 1. Introduction.....  | 1    |
| 1.1    Fundamentals of Non-Wetting Surfaces .....   | 2    |
| 1.2    Fabrication of SHS/SLIPS .....   | 4    |
| 1.3    Nomenclature.....  | 6    |
| 1.4    References.....  | 7    |
| Chapter 2. Nonwetting Surfaces Applications.....  | 16   |
| 2.1    Drag Reduction .....   | 16   |
| 2.1.1    Drag Reduction for Laminar Flow .....  | 16   |
| 2.1.2    Drag Reduction for Turbulent Flow .....  | 19   |
| 2.1.3    Drag Reduction over SLIPS .....  | 21   |
| 2.2    Fouling Reduction.....   | 22   |
| 2.2.1    Antifouling .....  | 24   |
| 2.2.2    Anti-Scaling .....   | 25   |
| 2.2.3    Anti-Bacterial/Biological Adhesion .....   | 25   |
| 2.2.4    Antifouling for SLIPS .....  | 30   |
| 2.3    Corrosion Resistance .....   | 32   |
| 2.4    Anti-Fogging and Anti-Icing .....  | 33   |
| 2.5    References .....   | 35   |
| Chapter 3. Condensation on Nonwetting Surfaces .....  | 49   |
| 3.1    Condensation over SHS .....  | 50   |
| 3.2    Condensation over Biophilic Surfaces .....   | 56   |
| 3.3    Surface Morphology Effect on Condensation.....   | 60   |
| 3.4    Low Surface Tension Fluids Condensation over SHS .....   | 63   |
| 3.5    Condensation over SLIPS .....  | 65   |
| 3.6    Nomenclature.....  | 75   |
| 3.7    References.....  | 76   |
| Chapter 4: Technoeconomic Analysis of Textured Surfaces for Improved Condenser Performance in<br>Thermoelectric Power Plants..... | 85   |
| 4.1    Introduction.....  | 86   |
| 4.2    Model and Analysis Methodology .....   | 89   |
| 4.2.1    Condenser and Power Plant Performance model .....  | 89   |
| 4.2.2    Cost model .....   | 93   |

|            |                                  |     |
|------------|----------------------------------|-----|
| 4.2.3      | Numerical Procedure.....         | 95  |
| 4.3        | Results and Discussion.....      | 96  |
| 4.3.1      | Model Verification.....          | 96  |
| 4.3.2      | Parametric Studies.....          | 99  |
| 4.3.3      | Numerical Optimization.....      | 112 |
| 4.4        | Conclusions.....                 | 116 |
| 4.5        | Nomenclature.....                | 117 |
| 4.6        | References.....                  | 121 |
| Chapter 5. | Conclusions and Future Work..... | 127 |

## List of Figures

|  |     |
|--|-----|
| <b>Figure 1.</b> Schematic illustration of condenser with textured tubes and SEM morphologies of textured superhydrophobic surfaces fabricated by the electrodepositing process [27]. .....  | 89  |
| <b>Figure 2.</b> Flowchart of the computational procedure for annual thermoelectric power plant performance analysis.....  | 97  |
| <b>Figure 3.</b> Validation of the present numerical model against numerical [42] and measurement [41] data in the literature. ....  | 99  |
| <b>Figure 4.</b> Daily variations in (a) fouling resistance, (b) steam condensing pressure and (c) steam condensation temperature, and (d) net electric power output from the plant. ....  | 100 |
| <b>Figure 5.</b> Monthly variations in (a) net electric energy output from the plant, (b) cooling water inlet and outlet temperature, and (c) number of plant outages.....   | 102 |
| <b>Figure 6.</b> Influence of number of plain titanium tubes in the condenser on (a,c) net annual electric energy output from the plant and (b,d) number of plant outages for condenser cleaning and maintenance for various tube diameters and cooling water velocity ..... | 104 |
| <b>Figure 7.</b> Influence of number of textured titanium tubes in the condenser on (a) net annual electric energy output from the plant and (b) number of plant outages for condenser cleaning and maintenance for various fouling rates. The default tube diameter.....    | 106 |
| <b>Figure 8.</b> Variation in levelized cost of condenser as a function of number of plain titanium tubes for various (a) cooling water velocity and (b) tube diameter. (c) Variation in levelized cost of condenser as a function of number of plain aluminum-brass.....    | 107 |
| <b>Figure 9.</b> Variation in levelized cost of condenser for various fouling rate factors and number of textured tubes of material (a) titanium (Ti) and (b) aluminum-brass (Al-Br). The default tube diameter is 0.025 m and cooling water velocity is 1.85 m/s.....       | 108 |
| <b>Figure 10.</b> Breakdown of total condenser cost for various number of textured tubes fabricated by the electrodeposition process made of material (a) titanium (Ti) and (b) aluminum-brass (Al-Br).....  | 110 |
| <b>Figure 11.</b> Influence of cooling water velocity and tube diameter on (a) minimum levelized cost of condenser and (b) corresponding optimal number of plain titanium tubes. Influence of cooling water velocity and fouling rate factors on (a) minimum leveliz .....   | 112 |
| <b>Figure 12.</b> Variation in (a,c) minimum levelized cost of condenser and (b,d) optimal number of tubes obtained for titanium and aluminum-brass tubes from numerical optimization studies for various fouling rate factors and dropwise heat transfer coefficient .....  | 115 |

## List of Tables

|                   |   |    |
|-------------------|---|----|
| <b>Table 1.1</b>  | Sample of various approaches for SHS/SLIPS surface fabrication.....   | 5  |
| <b>Table 3.1.</b> | Results of pressure increment step size refinement study. The bold-faced row represents the adopted pressure increment step size in this study..... | 98 |

## **Chapter 1. Introduction**

Nonwetting surfaces including superhydrophobic (SHS), liquid infused surfaces (SLIPS), and Superamphiphobic surfaces have attracted lots of attention due to their numerous promising characteristics including promoting condensation/evaporation, drag reduction, prohibiting fouling/deposition, corrosion resistance, fog/dew harvesting, and anti-icing. These attributes could inspire a variety of applications for these surfaces in power/nuclear plants [1], automotive and aviation industries, oils/organic solvents clean-up [2-6], fuel cells [7,8], solar panels [9-11], membrane distillation [12,13], water collection [14,15] stone/concrete protection [16,17], art preservation and printing [18,19], surgical fabrics [20-22] and biological applications [23,24]. Few of these applications have reached their potential for real-life implementation and more are still at the research phase needing more experimental and fundamental studies to get them ready.

In the first part of this thesis, Chapter 1, the fundamentals of nonwetting surfaces have been reviewed and basic models explaining wetting phenomena are presented. Then, fabrication methods for metallic surfaces have been explored to identify the most promising approaches which could be adopted in large scale industrial applications. The second part provides an in-depth literature review for nonwetting surface applications in drag reduction, anti-fouling, corrosion resistance, anti-icing and anti-fogging in Chapter 2. The literature on condensation over nonwetting surfaces is discussed in a separate Chapter 3. In both chapters, a comprehensive review of recent publications regarding the respective aspects has been carried out and is discussed in detail identifying the factors influencing potential applications. The third part of the thesis, Chapter 4, presents a technoeconomic study demonstrating how different benefits of nonwetting surfaces considered in part two are brought together for enhancement of system performance in an application. This chapter investigates the dynamic performance and economic benefits of implementing nonwetting surfaces fabricated via electrodeposition in power plant condensers. A numerical performance model has been developed and the effects of textured surfaces on the thermal performance of the condenser and power plant's efficiency have been analyzed to predict the potential promises. The work reported in this chapter formed the basis for the journal publication: K. Nithyanandam, P. Shoaie and R.

Pitchumani, “Technoeconomic Analysis of Thermoelectric Power Plant Condensers with Superhydrophobic and Liquid Infused Nonwetting Surfaces,” *Energy*, In Review, 2020. The thesis concludes with a summary and potential aspects for further consideration in a future work presented in Chapter 5.

## 1.1 Fundamentals of Non-Wetting Surfaces

Wettability of solid surfaces is identified by the contact angle that a liquid drop makes on the surface. Based on the observed contact angle, the solid surfaces are classified into four categories of superhydrophilic, (if the contact angle is less than 10°), hydrophilic (if the contact angle is between 10° and 90°), hydrophobic (if the contact angle is between 90° and 150°), and superhydrophobic, (if the contact angle is above 150°) [25]. Superhydrophobicity is the tendency of a surface to repel water drops [26-28]. In addition to exhibiting a high apparent contact angle (>150°), a superhydrophobic surface should have low contact angle hysteresis (<10°), low sliding angle (<5°), and high stability of Cassie model state. Surface wettability against a variety of working fluids could be evaluated in the same fashion for example Superamphiphobic surfaces exhibit both superhydrophobic and superoleophobic when exposed to water and oils respectively [29].

To get a better understanding of superhydrophobic surfaces, various models and theories of wetting have been presented. In this section, the basis of surface wetting behavior is introduced to clarify how surface characteristics affect the wetting states. The first wetting model was presented by Young in 1805 [30-32]. For a liquid drop on a perfectly smooth surface, Young’s equation describes the wetting status via the interfacial free energy of solid, liquid, and vapor. The contact angle  $\theta$  could be predicted based on the interfacial free energy as:

$$\cos \theta = \frac{\gamma_{SV} - \gamma_{SL}}{\gamma_{LV}} \quad (1)$$

where  $\gamma$  is the surface stress that characterizes energy per unit area for solid- vapor, solid-liquid, and liquid-vapor interfaces. Young’s contact angle is formed because of a thermodynamic balance of interfacial energy, in the solid-liquid-vapor boundary area. A

real surface usually is not an ideal smooth one, and surface roughness acts as an important factor in the wettability of the solid surface, therefore the contact angle states with Young's equation do not apply to actual conditions. To incorporate the effect of interfacial roughness, in 1936, Wenzel introduced another equation to clarify interfacial roughness and energy correlation, as of the following equation [33]:

$$r(\gamma_{SV} - \gamma_{SL}) = \gamma_{LV} \cos \theta_w^* \quad (2)$$

where  $\theta_w^*$  represents Wenzel's contact angle and is affected by the surface roughness, shown with roughness factor ( $r$ ). Modified Wenzel's equation is defined by the following equation:

$$\cos \theta_w^* = r \cos \theta \quad (3)$$

In Wenzel's formula, liquid penetrates the pores of the surface roughness. This represents a homogeneous wetting [26]. From Wenzel's equation, it can be concluded that roughness can increase both wetting and anti-wetting, reliant on the flat surface features. Thereby, if the smooth surface contact angle is bigger than  $90^\circ$ , surface roughness would increase the contact angle and if the contact angle is less than  $90^\circ$ , increased roughness would result in a lower contact angle.

When dealing with a dual scale surface structure/heterogeneous surfaces, the Wenzel model is not satisfactory and therefore the Cassie-Baxter model was proposed in 1944 [34]. In Cassie-Baxter's model, the drop and the solid are in contact only at the tip of the picks and small air pockets are stocked underneath the liquid. So, it can be considered that the fraction of surface area, in which the air pockets are trapped, doesn't wet by the drop. Cassie-Baxter's equation could be written as below:

$$\cos \theta_{CB} = f_s(\cos \theta_s + 1) - 1 \quad (4)$$

where  $\theta_{CB}$  represents the Cassie-Baxter angle,  $f_s$  is the area portion of the surface with the contact angle of  $\theta_s$ . It should be noted that Cassie-Baxter's model is not always valid for all kinds of surfaces, for example, if a surface owns hydrophilic property then the droplet may immerse into the gap structure. In addition to these basic models, there are more advanced models in the literature to predict specific states of wetting [35–40] few of which will be referenced in the following sections as specific features of nonwetting

surfaces are discussed. The modeling process for a variety of surface structures and wetting states is also reviewed by Chamakos et al. [41] and Parvate et al. [42].

## **1.2 Fabrication of SHS/SLIPS**

The main approaches for the fabrication of superhydrophobic surfaces are roughening the low surface energy materials [43-46] and application of low surface energy materials over rough structures [47-51]. SLIPS are also fabricated through approaches same as what is used for SHS with an additional step to infuse lubricating oils into rough micro/nanostructured substrates. There are several techniques developed for the fabrication of SHS and SLIPS for a variety of materials such as the Sol-gel method [52-55], Electrospinning [56-59], Layer-by-layer [60,61], and Plasma techniques, to name a few [62-64]. However, not all these methods could be applied to metallic surfaces. Fabrication of metallic SHS are reported via Femto/pico/nanosecond laser processing [65,66], Electrical discharge machining [67-69], Electrochemical etching/deposition/anodization [70], Chemical etching/deposition [71] and Spraying method. Also, Femtosecond laser processing [72], Electrochemical anodization [73,74], and chemical etching [75] have been implemented to fabricate SLIPS. There are several review papers published on the fabrication of nonwetting surfaces investigating their challenges and applications. Various fabrication strategies for SHS have been reviewed by Parvate et al. [42] and Jeevahan et al. [76]. Also, the stability and robustness of different SHS fabrication methods have been investigated by Scarratt et al. [77]. Fabrication methods for superoleophobic surfaces have been investigated by Ghaffari et al. in a recent review paper [78]. Lian et al. [29] also provided a comprehensive list of fabrication methods for nonwetting metallic surfaces developed in the last 10 years identifying the main characteristics of as-prepared surfaces. Table 1.1 provides a sample of fabrication methods for metallic SHS and SLIPS surfaces.

There have been significant advancements in the fabrication of SHS and SLIPS over the past decade. However, to make these surfaces ready for applications in the desired conditions, their long-term stability under conditions of wear, shear, pressure, immersion, and exposure to contamination should be tested and reported in a standardized process.

**Table 1.1** Sample of various approaches for SHS/SLIPS surface fabrication

| Methods   | Substrate  | Coating materials                                | Surface structure                                 | CA    | Features                               | Lubricant       | Ref  |
|---|--|--|---|-------|--|-----------------|------|
| LBL assembly                                      | Stainless steel mesh   | PDDA/halloysite                                  | Nanotubes Hierarchical structure                  | 151.5 | Superoleophobic                        | Chloroform      | [80] |
| Femtosecond laser                                 | Aluminum surface   | –  | Hierarchical rough Microstructure                 | 157   | Superoleophobic                        | Dichloroethane  | [72] |
| Electrochemical anodization and LBL self-assembly | Copper Mesh  | TiO <sub>2</sub> /CuO                            | Hierarchical structure                            | 162   | Superoleophobic                        | Dichloromethane | [73] |
| Electrochemical anodization                       | Copper mesh  | CuWO <sub>4</sub> /Cu <sub>2</sub> O             | Hierarchical cauliflower-like structure           | 156   | Superoleophobic                        | Dichloromethane | [74] |
| Electrodeposition                                 | Copper mesh  | Zn/ZnO crystal                                   | Flower-like hierarchical structure                | 155.6 | Superoleophobic                        | DCE             | [81] |
| Electrodeposition                                 | Titanium   | TiO <sub>2</sub> and PTFE composite Film         | Nanocomposite structure                           | 157   | Photocatalytic self-cleaning           | –               | [82] |
| Electrospinning Without Functionalization         | Aluminum foil  | PTFEMA fibers                                    | Re-entrant structure                              | 154.2 | Superoleophobic                        | Hexadecane      | [83] |
| Electropolymerization                             | Gold plate   | Polyedopc3f6                                     |   | 152.2 | Superoleophobic                        | Hexadecane      | [84] |
| Electrochemical etching                           | Titanium alloy   | TiO <sub>2</sub>                                 | Hierarchical micro/nanostructures                 | 158.9 | Superoleophobic                        | Dichloromethane | [85] |
| Chemical acid etching and anodization             | Titanium   | TiO <sub>2</sub>                                 | Hierarchical micro horn/nanopore Structures       | 156.4 | Superoleophobic                        | Hexadecane      | [75] |
| Hydrothermal Process (HT) Chemical Etching (CE)   | Aluminum alloy (HT-Al)<br>Titanium (HT-Ti)<br>Magnesium (HTMg)<br>Aluminum alloy (CE-Al)<br>Titanium (CE-Ti)<br>Magnesium (CEMg) | Perfluoro octyltriethoxy silane (PFOTES)         |   | 162   | Corrosion-resistant                    | –               | [85] |
|   |  |  |   | 155   |  |                 |      |
|   |  |  |   | 157   |  |                 |      |
|   |  |  |   | 160   |  |                 |      |
|   |  |  |   | 162   |  |                 |      |
|   | 160  |  |   |       |  |                 |      |
| Solution immersion-self assembly                  | Copper foil  | Copper Oxide                                     | Hierarchical micro/nano structures                | 155   | Chemical stability                     | Wax solution    | [86] |
| Solution immersion                                | Manganese  | Lauric diethanolamide and stearic acid (LDEA-SA) |   | 124   | Corrosion resistance                   | -               | [87] |
| Spraying  | Steel  | Silica-Fluoropolymer                             | Hybrid Nanoparticles                              | 150   | 40% Optical transmittance reduction    | –               | [88] |
| Magnetic field-induced deposition                 | Copper<br>Nickel<br>Copper-nickel alloy  | Copper<br>Nickel<br>Copper-nickel alloy          | Nanostructures                                    | 152.2 | Ferromagnetic and catalytic properties | –               | [89] |
|   |  |  |   | 151.7 |  |                 |      |
|   |  |  |   | >153  |  |                 |      |
| Electrical discharge machining method             | Copper   |  | T-shaped grooves Micro- and nano-scale structures | 152.5 | Anti-wear ability                      | –               | [67] |

To achieve realistic applications on a large scale, the development of robust and truly applicable super-repellent structured surfaces should shift toward single-step processes with low fabrication costs. Laser processing, electrospinning and chemical deposition methods using a large amount of precious metals such as gold and silver are all expensive and inefficient. Surfaces made by spraying, electrospinning, sol-gel, layer-by-layer self-assembly, and dip-coating methods are mainly mechanically combined, consequently have less mechanical durability and may not withstand harsh industrial environments. On the other hand, fabrication of hierarchical superhydrophobic surfaces through surface oxidation of metals is a simple and cost-effective process. Electrochemical methods are also simple, fast, highly repeatable, and less expensive and offer a feasible way to obtain uniform and large-area superhydrophobic coatings on metal surfaces with different surface morphologies [79]. However, the large amount of chemicals consumed in these processes leads to a negative environmental impact. To limit these environmental impacts, the nanosecond laser processing and electrical discharge machining methods could be considered promising fabrication methods as they are simple, low cost, and produce durable surfaces.

### 1.3 Nomenclature

$f$  Surface area fraction

$r$  Roughness factor

#### *Subscripts and Superscripts*

$s$  Surface

#### *Greek Symbols*

$\theta$  Contact angle

$\theta_{CB}$  Cassie-Baxter angle

$\theta_w^*$  Wenzel's contact angle

$\gamma_{LV}$  Liquid-vapor interfacial free energy

$\gamma_{SL}$  Surface-liquid interfacial free energy

$\gamma_{sv}$  Surface-vapor interfacial free energy

*Acronyms*

*CA* Contact angle

*SHS* Superhydrophobic surface

*SLIPS* Slippery liquid infused porous surface

## 1.4 References

1. Zhang, Y., Ren, F. and Liu, Y., 2018. A superhydrophobic EP/PDMS nanocomposite coating with high gamma radiation stability. *Applied Surface Science*, 436, pp.405-410.
2. Nanda, D., Sahoo, A., Kumar, A. and Bhushan, B., 2019. Facile approach to develop durable and reusable superhydrophobic/superoleophilic coatings for steel mesh surfaces. *Journal of colloid and interface science*, 535, pp.50-57.
3. Xiang, Y., Pang, Y., Jiang, X., Huang, J., Xi, F. and Liu, J., 2018. One-step fabrication of novel superhydrophobic and superoleophilic sponge with outstanding absorbency and flame-retardancy for the selective removal of oily organic solvent from water. *Applied Surface Science*, 428, pp.338-347.
4. Hao, W., Xu, J., Li, R., Zhao, X., Qiu, L. and Yang, W., 2019. Developing superhydrophobic rock wool for high-viscosity oil/water separation. *Chemical Engineering Journal*, 368, pp.837-846.
5. Wang, Y., Chen, A., Peng, M., Tan, D., Liu, X., Shang, C., Luo, S. and Peng, L., 2019. Preparation and characterization of a fluorinated kaolin-modified melamine sponge as an absorbent for efficient and rapid oil/water separation. *Journal of Cleaner Production*, 217, pp.308-316.
6. Luo, Y., Wang, X., Zhang, R., Singh, M., Ammar, A., Cousins, D., Hassan, M.K., Ponnamma, D., Adham, S., Al-Maadeed, M.A.A. and Karim, A., 2020. Vertically oriented nanoporous block copolymer membranes for oil/water separation and filtration. *Soft Matter*, 16(42), pp.9648-9654.
7. Ryzhakov, P.B., Jarauta, A., Secanell, M. and Pons-Prats, J., 2017. On the application of the PFEM to droplet dynamics modeling in fuel cells. *Computational Particle Mechanics*, 4(3), pp.285-295.
8. Tranter, T.G., Stogornyyuk, P., Gostick, J.T., Burns, A.D. and Gale, W.F., 2017. A method for measuring relative in-plane diffusivity of thin and partially saturated porous media: an

- application to fuel cell gas diffusion layers. *International Journal of Heat and Mass Transfer*, 110, pp.132-141.
9. Yilbas, B.S., Al-Sharafi, A. and Sahin, A.Z., 2020. Solar energy harvesting and a water droplet cleaning of micropost arrays surfaces. *International Journal of Energy Research*, 44(3), pp.2072-2083.
  10. Yousaf, M.R., Yilbas, B.S. and Ali, H., 2018. Assessment of optical transmittance of oil impregnated and non-wetted surfaces in outdoor environment towards solar energy harvesting. *Solar Energy*, 163, pp.25-31.
  11. Yang, Z., Xue, X., Dai, J.G., Li, Y., Qin, J., Feng, Y., Qu, J., He, Z., Sun, P., Xu, L. and Zhang, T., 2018. Study of a super-non-wetting self-cleaning solar reflective blue-grey paint coating with luminescence. *Solar Energy Materials and Solar Cells*, 176, pp.69-80.
  12. Sinha Ray, S., Singh Bakshi, H., Dangayach, R., Singh, R., Deb, C.K., Ganesapillai, M., Chen, S.S. and Purkait, M.K., 2020. Recent developments in nanomaterials-modified membranes for improved membrane distillation performance. *Membranes*, 10(7), p.140.
  13. Rosli, A., Ahmad, A.L. and Low, S.C., 2020. Functionalization of silica nanoparticles to reduce membrane swelling in CO<sub>2</sub> absorption process. *Journal of Chemical Technology & Biotechnology*, 95(4), pp.1073-1084.
  14. Park, K.C., Kim, P., Grinthal, A., He, N., Fox, D., Weaver, J.C. and Aizenberg, J., 2016. Condensation on slippery asymmetric bumps. *Nature*, 531(7592), pp.78-82.
  15. Luo, H., Lu, Y., Yin, S., Huang, S., Song, J., Chen, F., Chen, F., Carmalt, C.J. and Parkin, I.P., 2018. Robust platform for water harvesting and directional transport. *Journal of Materials Chemistry A*, 6(14), pp.5635-5643.
  16. Mundo, R.D., Labianca, C., Carbone, G. and Notarnicola, M., 2020. Recent Advances in Hydrophobic and Icephobic Surface Treatments of Concrete. *Coatings*, 10(5), p.449.
  17. Li, Y., Chen, W., Qu, J., Qin, J., Zhang, T. and Zhang, W., 2019, October. A Cost-effective Method to Fabricate a Super-non-wetting Self-cleaning Transparent Emulsion Paint Coating. In *IOP Conference Series: Earth and Environmental Science* (Vol. 330, No. 4, p. 042005). IOP Publishing.
  18. Cao, Y., Salvini, A. and Camaiti, M., 2020. Current Status and Future Prospects of Applying Bioinspired Superhydrophobic Materials for Conservation of Stone Artworks. *Coatings*, 10(4), p.353.
  19. Cui, Z., Zhang, F., Wang, L., Xu, S. and Guo, X., 2010. In situ crystallized zirconium phenylphosphonate films with crystals vertically to the substrate and their hydrophobic, dielectric, and anticorrosion properties. *Langmuir*, 26(1), pp.179-182.

20. Petrusis, D. and Petruyte, S., 2017. Effect of surgical fabrics structure on wetting behaviour. *International Journal of Clothing Science and Technology*.
21. Yilbas, B.S., Hassan, G., Al-Qahtani, H., Al-Aqeeli, N., Al-Sharafi, A., Al-Merbati, A.S., Baroud, T.N. and Adukwu, J.A.E., 2019. Stretchable Hydrophobic Surfaces and Self-Cleaning Applications. *Scientific reports*, 9(1), pp.1-13.
22. Cheng, Y., Zhu, T., Li, S., Huang, J., Mao, J., Yang, H., Gao, S., Chen, Z. and Lai, Y., 2019. A novel strategy for fabricating robust superhydrophobic fabrics by environmentally-friendly enzyme etching. *Chemical Engineering Journal*, 355, pp.290-298.
23. Agrawal, P., Bachus, K.J., Carriere, G., Grouse, P. and Oleschuk, R.D., 2019. An investigation into the kinematics of magnetically driven droplets on various (super) hydrophobic surfaces and their application to an automated multi-droplet platform. *Analytical and bioanalytical chemistry*, 411(21), pp.5393-5403.
24. Li, L., Tian, J., Li, M. and Shen, W., 2013. Superhydrophobic surface supported bioassay—an application in blood typing. *Colloids and Surfaces B: Biointerfaces*, 106, pp.176-180.
25. Koch, K. and Barthlott, W., 2009. Superhydrophobic and superhydrophilic plant surfaces: an inspiration for biomimetic materials. *Philosophical Transactions of the Royal Society A: Mathematical, Physical and Engineering Sciences*, 367(1893), pp.1487-1509.
26. Marmur, A., 2003. Wetting on hydrophobic rough surfaces: to be heterogeneous or not to be?. *Langmuir*, 19(20), pp.8343-8348.
27. Blossey, R., 2003. Self-cleaning surfaces—virtual realities. *Nature materials*, 2(5), pp.301-306.
28. Cassie, A.B.D. and Baxter, S., 1944. Wettability of porous surfaces. *Transactions of the Faraday society*, 40, pp.546-551.
29. Lian, Z., Xu, J., Wang, Z. and Yu, H., 2020. Biomimetic Superlyophobic Metallic Surfaces: Focusing on Their Fabrication and Applications. *Journal of Bionic Engineering*, 17(1), pp.1-33.
30. Young, T., 1805. III. An essay on the cohesion of fluids. *Philosophical transactions of the royal society of London*, (95), pp.65-87.
31. Good, R.J., 1952. A thermodynamic derivation of Wenzel's modification of Young's equation for contact angles; together with a theory of Hysteresis<sup>1</sup>. *Journal of the American Chemical Society*, 74(20), pp.5041-5042.

32. Zhao, N., Xie, Q., Weng, L., Wang, S., Zhang, X. and Xu, J., 2005. Superhydrophobic surface from vapor-induced phase separation of copolymer micellar solution. *Macromolecules*, 38(22), pp.8996-8999.
33. Wenzel, R.N., 1936. Resistance of solid surfaces to wetting by water. *Industrial & Engineering Chemistry*, 28(8), pp.988-994.
34. Hsu, S.H., Woan, K. and Sigmund, W., 2011. Biologically inspired hairy structures for superhydrophobicity. *Materials Science and Engineering: R: Reports*, 72(10), pp.189-201.
35. Erbil, H.Y. and Cansoy, C.E., 2009. Range of applicability of the Wenzel and Cassie–Baxter equations for superhydrophobic surfaces. *Langmuir*, 25(24), pp.14135-14145.
36. Koishi, T., Yasuoka, K., Fujikawa, S., Ebisuzaki, T. and Zeng, X.C., 2009. Coexistence and transition between Cassie and Wenzel state on pillared hydrophobic surface. *Proceedings of the National Academy of Sciences*, 106(21), pp.8435-8440.
37. Lundgren, M., Allan, N.L. and Cosgrove, T., 2007. Modeling of wetting: a study of nanowetting at rough and heterogeneous surfaces. *Langmuir*, 23(3), pp.1187-1194.
38. Jung, Y.C. and Bhushan, B., 2009. Dynamic effects induced transition of droplets on biomimetic superhydrophobic surfaces. *Langmuir*, 25(16), pp.9208-9218.
39. Vrancken, R.J., Kusumaatmaja, H., Hermans, K., Prenen, A.M., Pierre-Louis, O., Bastiaansen, C.W. and Broer, D.J., 2010. Fully reversible transition from Wenzel to Cassie–Baxter states on corrugated superhydrophobic surfaces. *Langmuir*, 26(5), pp.3335-3341.
40. Reyssat, M., Yeomans, J.M. and Quéré, D., 2007. Impalement of fakir drops. *EPL (Europhysics Letters)*, 81(2), p.26006.
41. Chamakos, N.T., Sema, D.G. and Papathanasiou, A.G., 2020. Progress in Modeling Wetting Phenomena on Structured Substrates. *Archives of Computational Methods in Engineering*, pp.1-20.
42. Parvate, S., Dixit, P. and Chattopadhyay, S., 2020. Superhydrophobic Surfaces: Insights from Theory and Experiment. *The Journal of Physical Chemistry B*, 124(8), pp.1323-1360.
43. Yabu, H. and Shimomura, M., 2005. Single-step fabrication of transparent superhydrophobic porous polymer films. *Chemistry of materials*, 17(21), pp.5231-5234.
44. Lu, X., Zhang, C. and Han, Y., 2004. Low-density polyethylene superhydrophobic surface by control of its crystallization behavior. *Macromolecular Rapid Communications*, 25(18), pp.1606-1610.

45. Khorasani, M.T., Mirzadeh, H.A.M.I.D. and Kermani, Z., 2005. Wettability of porous polydimethylsiloxane surface: morphology study. *Applied Surface Science*, 242(3-4), pp.339-345.
46. Feng, X., Feng, L., Jin, M., Zhai, J., Jiang, L. and Zhu, D., 2004. Reversible superhydrophobicity to super-hydrophilicity transition of aligned ZnO nanorod films. *Journal of the American Chemical Society*, 126(1), pp.62-63.
47. Teshima, K., Sugimura, H., Inoue, Y., Takai, O. and Takano, A., 2005. Transparent ultra water-repellent poly (ethylene terephthalate) substrates fabricated by oxygen plasma treatment and subsequent hydrophobic coating. *Applied Surface Science*, 244(1-4), pp.619-622.
48. Zhang, X., Shi, F., Yu, X., Liu, H., Fu, Y., Wang, Z., Jiang, L. and Li, X., 2004. Polyelectrolyte multilayer as matrix for electrochemical deposition of gold clusters: toward super-hydrophobic surface. *Journal of the American Chemical Society*, 126(10), pp.3064-3065.
49. Qian, B. and Shen, Z., 2005. Fabrication of superhydrophobic surfaces by dislocation-selective chemical etching on aluminum, copper, and zinc substrates. *Langmuir*, 21(20), pp.9007-9009.
50. Shang, H.M., Wang, Y., Limmer, S.J., Chou, T.P., Takahashi, K. and Cao, G.Z., 2005. Optically transparent superhydrophobic silica-based films. *Thin Solid Films*, 472(1-2), pp.37-43.
51. Wu, X., Zheng, L. and Wu, D., 2005. Fabrication of superhydrophobic surfaces from microstructured ZnO-based surfaces via a wet-chemical route. *Langmuir*, 21(7), pp.2665-2667.
52. Jitianu, A., Doyle, J., Amatucci, G. and Klein, L.C., 2010. Methyl modified siloxane melting gels for hydrophobic films. *Journal of sol-gel science and technology*, 53(2), pp.272-279.
53. Yu, M., Gu, G., Meng, W.D. and Qing, F.L., 2007. Superhydrophobic cotton fabric coating based on a complex layer of silica nanoparticles and perfluorooctylated quaternary ammonium silane coupling agent. *Applied surface science*, 253(7), pp.3669-3673.
54. Liang, J., Hu, Y., Wu, Y. and Chen, H., 2014. Facile formation of superhydrophobic silica-based surface on aluminum substrate with tetraethylorthosilicate and vinyltriethoxysilane as co-precursor and its corrosion resistant performance in corrosive NaCl aqueous solution. *Surface and Coatings Technology*, 240, pp.145-153.

55. Mo, C., Zheng, Y., Wang, F. and Mo, Q., 2015. A simple process for fabricating organic/TiO<sub>2</sub> super-hydrophobic and anti-corrosion coating. *Int. J. Electrochem. Sci*, 10(9), pp.7380-7391.
56. Wang, N., Zhao, Y. and Jiang, L., 2008. Low-Cost, Thermoresponsive Wettability of Surfaces: Poly (N-isopropylacrylamide)/Polystyrene Composite Films Prepared by Electrospinning. *Macromolecular Rapid Communications*, 29(6), pp.485-489.
57. Tuteja, A., Choi, W., Ma, M., Mabry, J.M., Mazzella, S.A., Rutledge, G.C., McKinley, G.H. and Cohen, R.E., 2007. Designing superoleophobic surfaces. *Science*, 318(5856), pp.1618-1622.
58. Radwan, A.B., Mohamed, A.M., Abdullah, A.M. and Al-Maadeed, M.A., 2016. Corrosion protection of electrospun PVDF–ZnO superhydrophobic coating. *Surface and Coatings Technology*, 289, pp.136-143.
59. Mohamed, A.M., Jafari, R. and Farzaneh, M., 2014. An optimization of superhydrophobic polyvinylidene fluoride/zinc oxide materials using Taguchi method. *Applied Surface Science*, 288, pp.229-237.
60. Han, J.T., Zheng, Y., Cho, J.H., Xu, X. and Cho, K., 2005. Stable superhydrophobic organic– inorganic hybrid films by electrostatic self-assembly. *The Journal of Physical Chemistry B*, 109(44), pp.20773-20778.
61. Zhao, N., Shi, F., Wang, Z. and Zhang, X., 2005. Combining layer-by-layer assembly with electrodeposition of silver aggregates for fabricating superhydrophobic surfaces. *Langmuir*, 21(10), pp.4713-4716.
62. Yung, C.S., Tomlin, N.A., Heuerman, K., Keller, M.W., White, M.G., Stephens, M. and Lehman, J.H., 2018. Plasma modification of vertically aligned carbon nanotubes: Superhydrophobic surfaces with ultra-low reflectance. *Carbon*, 127, pp.195-201.
63. Ryu, J., Kim, K., Park, J., Hwang, B.G., Ko, Y., Kim, H., Han, J., Seo, E., Park, Y. and Lee, S.J., 2017. Nearly perfect durable superhydrophobic surfaces fabricated by a simple one-step plasma treatment. *Scientific reports*, 7(1), pp.1-8.
64. Sharifi, N., Ettouil, F.B., Moreau, C., Dolatabadi, A. and Pugh, M., 2017. Engineering surface texture and hierarchical morphology of suspension plasma sprayed TiO<sub>2</sub> coatings to control wetting behavior and superhydrophobic properties. *Surface and Coatings Technology*, 329, pp.139-148.
65. Tang, M.K., Huang, X.J., Li, X.W., Huang, Z.Y., Zhang, S.M. and Zhang, Q.X., 2016. Fabrication of superhydrophobic surface with superior anticorrosion and great

- mechanical stability on AA7075 Al alloy via a convenient and efficient approach. *Materials Express*, 6(2), pp.101-115.
66. Tran, N.G. and Chun, D.M., 2020. Simple and fast surface modification of nanosecond-pulse laser-textured stainless steel for robust superhydrophobic surfaces. *CIRP Annals*.
  67. Wang, Y., Cheng, W., Zhang, D., Yu, Q., Wan, Y., Xu, J. and Yu, H., 2019. Rapid preparation of high adhesion superhydrophobic surface of T—groove. *Materials Research Express*, 6(8), p.0865h7.
  68. Dong, S., Wang, Z., Wang, Y., Bai, X., Fu, Y.Q., Guo, B., Tan, C., Zhang, J. and Hu, P., 2018. Roll-to-roll manufacturing of robust superhydrophobic coating on metallic engineering materials. *ACS applied materials & interfaces*, 10(2), pp.2174-2184.
  69. Gao, D., Cao, J. and Guo, Z., 2019. Underwater manipulation of oil droplets and bubbles on superhydrophobic surfaces via switchable adhesion. *Chemical Communications*, 55(23), pp.3394-3397. [28] Lu, Y., Xu, W., Song, J., Liu, X., Xing, Y. and Sun, J., 2012. Preparation of superhydrophobic titanium surfaces via electrochemical etching and fluorosilane modification. *Applied surface science*, 263, pp.297-301.
  70. Xu, N., Sarkar, D.K., Chen, X.G. and Tong, W.P., 2016. Corrosion performance of superhydrophobic nickel stearate/nickel hydroxide thin films on aluminum alloy by a simple one-step electrodeposition process. *Surface and Coatings Technology*, 302, pp.173-184.
  71. YU, S., LIU, J. and DIAO, W., 2014. Fabrication of bionic superhydrophobic surface on X52 pipeline steel. *Chinese Science Bulletin*, 59(3), pp.273-278.
  72. Zhang, J., Chen, F., Yang, Q., Yong, J., Huo, J., Fang, Y. and Hou, X., 2017. A widely applicable method to fabricate underwater superoleophobic surfaces with low oil-adhesion on different metals by a femtosecond laser. *Applied Physics A*, 123(9), p.594.
  73. Chen, Z., Zhou, C., Lin, J., Zhu, Z., Feng, J., Fang, L. and Cheng, J., 2018. ZrO<sub>2</sub>-coated stainless steel mesh with underwater superoleophobicity by electrophoretic deposition for durable oil/water separation. *Journal of Sol-Gel Science and Technology*, 85(1), pp.23-30.
  74. Zhou, C., Cheng, J., Hou, K., Zhu, Z. and Zheng, Y., 2017. Preparation of CuWO<sub>4</sub>@Cu<sub>2</sub>O film on copper mesh by anodization for oil/water separation and aqueous pollutant degradation. *Chemical Engineering Journal*, 307, pp.803-811.
  75. Zhou, C., Cheng, J., Hou, K., Zhu, Z. and Zheng, Y., 2017. Preparation of CuWO<sub>4</sub>@Cu<sub>2</sub>O film on copper mesh by anodization for oil/water separation and aqueous pollutant degradation. *Chemical Engineering Journal*, 307, pp.803-811.

76. Jeevahan, J., Chandrasekaran, M., Joseph, G.B., Durairaj, R.B. and Mageshwaran, G.J.J.O.C.T., 2018. Superhydrophobic surfaces: a review on fundamentals, applications, and challenges. *Journal of Coatings Technology and Research*, 15(2), pp.231-250.
77. Scarratt, L.R., Steiner, U. and Neto, C., 2017. A review on the mechanical and thermodynamic robustness of superhydrophobic surfaces. *Advances in colloid and interface science*, 246, pp.133-152.
78. Ghaffari, S., Aliofkhaeaei, M., Darband, G.B., Zakeri, A. and Ahmadi, E., 2019. Review of superoleophobic surfaces: Evaluation, fabrication methods, and industrial applications. *Surfaces and Interfaces*, 17, p.100340.
79. Darmanin, T., de Givenchy, E.T., Amigoni, S. and Guittard, F., 2013. Superhydrophobic surfaces by electrochemical processes. *Advanced materials*, 25(10), pp.1378-1394.
80. Hou, K., Zeng, Y., Zhou, C., Chen, J., Wen, X., Xu, S., Cheng, J., Lin, Y. and Pi, P., 2017. Durable underwater superoleophobic PDDA/halloysite nanotubes decorated stainless steel mesh for efficient oil–water separation. *Applied Surface Science*, 416, pp.344-352.
81. You, Q., Ran, G., Wang, C., Zhao, Y. and Song, Q., 2018. A novel superhydrophilic–underwater superoleophobic Zn-ZnO electrodeposited copper mesh for efficient oil/water separation. *Separation and Purification Technology*, 193, pp.21-28.
82. Kamegawa, T., Shimizu, Y. and Yamashita, H., 2012. Superhydrophobic surfaces with photocatalytic self-cleaning properties by nanocomposite coating of TiO<sub>2</sub> and polytetrafluoroethylene. *Advanced Materials*, 24(27), pp.3697-3700.
83. Guo, Y., Tang, D., Zhao, E., Yu, Z., Lv, H. and Li, X., 2015. Controlled synthesis of amphiphilic graft copolymer for superhydrophobic electrospun fibres with effective surface fluorine enrichment: the role of electric field and solvent. *RSC advances*, 5(101), pp.82789-82799.
84. Yoon, Y., Kim, D. and Lee, J.B., 2014. *Micro and Nano Syst. Lett*, 2, pp.1-18.
85. Ou, J., Hu, W., Xue, M., Wang, F. and Li, W., 2013. Superhydrophobic surfaces on light alloy substrates fabricated by a versatile process and their corrosion protection. *ACS applied materials & interfaces*, 5(8), pp.3101-3107.
86. Liu, J., Huang, X., Li, Y., Li, Z., Chi, Q. and Li, G., 2008. Formation of hierarchical CuO microcabbages as stable bionic superhydrophobic materials via a room-temperature solution-immersion process. *Solid State Sciences*, 10(11), pp.1568-1576.

87. Lu, F., Cao, Z.F., Yang, F., Wang, S. and Zhong, H., 2019. Fabrication of hydrophobic coating on electrolytic manganese surface for enhancing corrosion resistance. *Progress in Organic Coatings*, 132, pp.379-387.
88. Lee, S.G., Ham, D.S., Lee, D.Y., Bong, H. and Cho, K., 2013. Transparent superhydrophobic/translucent superamphiphobic coatings based on silica-fluoropolymer hybrid nanoparticles. *Langmuir*, 29(48), pp.15051-15057.
89. Li, H., Liao, J., Du, Y., You, T., Liao, W. and Wen, L., 2013. Magnetic-field-induced deposition to fabricate multifunctional nanostructured Co, Ni, and CoNi alloy films as catalysts, ferromagnetic and superhydrophobic materials. *Chemical Communications*, 49(17), pp.1768-1770.

## **Chapter 2. Nonwetting Surfaces Applications**

This chapter presents a review of the literature on nonwetting surfaces for drag reduction (Section 2.1), anti-fouling (Section 2.2), anti-corrosion (Section 2.3) and anti-icing/anti-fogging (Section 2.4) applications.

### **2.1 Drag Reduction**

One of the noticeable characteristics of SHS/SLIPS is its ability to reduce drag force. The air pockets trapped on superhydrophobic surfaces act like a cushion layer that permits the liquid to slide on the surface without touching the solid substrate. This phenomenon is known as the slip effect which can result in the reduction of the drag force on SHS. Drag force reduction could have a considerable cost effect on marine objects and pipelines used in a variety of industries. The amount of slip is quantified with a slip length, which is defined as the ratio of slip velocity to the shear rate at the wall or a virtual distance into the wall at which the liquid velocity vanishes to zero when linearly extrapolated. The slip length on smooth hydrophobic surfaces is less than tens of nanometers while that on hydrophilic surfaces is effectively zero or negligible [1-3]. It's been shown that, for large scale boundary layer flows and pipe flows, where the characteristic length of the flow is on the order of millimeters, the order of the slip length should be on the order of hundred micrometers to obtain a considerable drag reduction [4]. To obtain an effective slip, not only an SHS is needed but also the surface should be able to maintain the Cassie wetting state during the flow. Also, it should be noted that the apparent contact angle of the surface should not be interpreted as the measure of the liquid slip or drag reduction as there are surfaces with an apparent contact angle over  $150^\circ$  where the water maintains a Wenzel state over them or SHS which have shown no effective slip.

#### **2.1.1 Drag Reduction for Laminar Flow**

Slip length is determined by the structural features of SHS, such as the pattern type, pitch, solid fraction, and also is affected by the state of the liquid-gas interface [5]. It's

been shown that roughness has a positive effect on drag as it decreases the contact area between the solid surface and fluid. Effect of grooves size and shape on drag reduction in microchannels have been studied and it's determined that increasing the depth to width ratio of the grooves can increase the pressure drop through the channel up to some point but a further increase can improve the friction loss [6]. For laminar microchannel flow, a large drag reduction can be achieved by using trapezoidal grooves in comparison with triangular grooves, rectangular grooves, and circular segment grooves [7].

Although fabrication of random roughness surfaces is less costly and faster, regular structures decrease the drag force better than surfaces with random roughness. [8]. Surfaces with random structures may experience loss of the trapped gas layer (plastron) which leads to the wetting transition and the smaller slip lengths at a given liquid pressure [9]. Both nanoscale [10] and microscale [11,12] superhydrophobic surfaces can reduce drag force. Besides, the hierarchical or dual structure roughness surfaces have shown high potential in decreasing the drag force in comparison to surfaces with single scale structure as they could maintain a more stable plastron layer in a larger range of the Reynolds numbers [6,13,14].

Beyond surface structure, a pressure difference between the trapped gas and surrounding liquid would cause the liquid-air interface to have a transition from the Cassie to the Wenzel state. If the meniscus penetrates the void of the surface structures the slip length would decrease, on the other hand, the overgrown gas pockets could enhance the slip [15,16]. In addition, on irregular structures the neighboring gas pockets could merge to form larger pockets and further increase the slip however they are unstable and expected to exist only temporarily [17]. If the hydrostatic/hydrodynamic pressure over the surface is too high the water can start to penetrate the pores of the surface increasing the contact area between the solid and liquid which leads to halting the drag reduction effect [18-21]. Effect of hydrostatic pressure on the effectiveness of the superhydrophobic surfaces has been studied by several researchers and it's shown that the pressure fluctuation leads to filling the surface asperities or collapsing the air gaps earlier than reaching the critical hydrostatic pressure [22-25].

The effects of surface wettability on two-phase pressure drop also have been represented in the literature [26,27]. To investigate the effect of hydrophobicity on the

hydrodynamics of an adiabatic two-phase channel flow a study was carried out for air/water mixtures with superficial Reynolds numbers ranging from 22–215 and 55–220, respectively. The data revealed a reduction in the pressure drop for two-phase flow in a channel with a single superhydrophobic wall compared to a control scenario. The observed reduction was approximately 10 percent greater than the reduction that is observed for single-phase flow (relative to a classical channel). The ratio of the reduction in drag for a superhydrophobic surface relative to a hydrophilic surface decreases with increasing vapor qualities, indicating that the effect of the superhydrophobicity is greater with increasing vapor fraction. It is shown that superhydrophobic walls have the potential to reduce drag in two-phase flows, depending on the channel size and flow regime [27,28].

Plastron stability is the main obstacle for the real-life application of SHS for drag reduction applications. High water pressure [18,29,30], high shear flow [17], air diffusion [31-34], condensation [35], and pressure fluctuations [24] have been regarded as the main sources of plastron depletion. The enhancement of the plastron layer stability by alternative passive and active methods are reported in the literature. For passive methods, no external energy source is required such as the use of hybrid surfaces for channel walls [36] or application of surfaces with hydrophobic hair structures with hydrophilic patches on top where the hydrophilic tips make the water-air meniscus pinned even when the pressure of the trapped air becomes larger than the water pressure [37]. In another approach, a side-channel was added under the SHS in a way that the air layer on the SHS was automatically compressed by a flowing liquid in the side channel [38] where the maximum sustainable pressure of the SHS was increased from 8 to 25 kPa without any deterioration of slippage effect. Surface pattern design such as ridges with small widths and lengths are reported to sustain air entrapment even at high-pressure gradient conditions and could enhance the drag reduction efficiency by suppressing the deformation of the air-water meniscus [39].

Active plastron stability enhancement methods are reported through pressurization of the air layer on SHS where with this approach, the SHS could be sustained up to a water pressure of 60 kPa [40,41]. Another energy-efficient approach was proposed to automatically restore the plastron when it is lost, by generating a self-controlled gas layer

that guarantees the surface superhydrophobicity under high liquid pressure conditions (up to 7 bar) [42,43]. In this method, electrodes are patterned over a multi-scale structure for an electrolytic gas generation; as water intrudes the microstructures, the electrodes generate gas by electrolysis, as the impregnating water closes the electrochemical circuit between the electrode and the conductive liquid. The newly generated gas displaces the wetting liquid out of the surface structures and eventually restores a gas film on the SHS. Gas layer regeneration over SHS via solar energy instead of electrical energy is also reported [44]. Sustaining the air bubbles in a textured hydrophobic surface by changing the water temperature near the surface is explored as well [45,46].

Besides the scalable fabrication method, Other characteristics of the surface such as its mechanical stability, corrosion resistance, and biofouling resistance will affect the real-life application of the SHS for drag reduction purposes. Recent studies have targeted such a combination toward functional surface manufacturing. A low-cost facile two-step spraying method of preparing superhydrophobic surfaces on aluminum substrates was reported where as-prepared surfaces showed good mechanical durability, anti-corrosion, and drag reduction properties. Rheometry results demonstrated that the surface drag reduction rate could reach up to 48.7% [47]. The superhydrophobic surface with a 3D flower-like micro-nano structure on the steel foil using the method of high-temperature oxidation is also reported which showed the drag reduction ratio of 20–30% at low velocities. In another attempt to obtain a robust SHS, a superhydrophobic paint was developed using 1H,1H,2H,2H-perfluorooctyltriethoxysilane (PFOTES), TiO<sub>2</sub> nanoparticles, and ethanol which could be readily applied to the surfaces via painting and spraying regardless of the size and structure of the surface. It was shown that this superhydrophobic coating could reduce the water drag force up to 12.7% [48].

### **2.1.2 Drag Reduction for Turbulent Flow**

The numerical and experimental studies for turbulent flow conditions have shown that SHS can result in significant turbulent drag reduction, as the turbulent vortices become weakened near the SHS and the main characteristic length scale for the turbulent flow changes to a thin viscous sublayer. Using regular-structured SHS of large slip lengths,

drag reductions of as much as 75 % have been reported in turbulent boundary layer flows [49,12,20]. Although some experimental studies showed drag reduction on random structured SHS such as those made via electrodeposition processes [50], plastron deterioration and dismissal of drag reduction on random SHS were reported for turbulent flows which are similar to the trend widely seen for laminar flows [51]. Effect of surface morphology and Reynold number on drag reduction was studied by Rastegari et al. [52] through a lattice Boltzmann model for SHS channels. In some cases, a higher than 80 % reduction in drag force was achieved. The drag reduction of superhydrophobic surfaces through turbulent pipe flow was also studied by Costantini et al. [53] for streamwise grooves at the wall surface. They reported that the grooves' dimension and the solid fraction strongly affect the drag reduction. Also, drag reduction, caused by a rise in mean slip velocity, leads to increasing the flow rate at a fixed pressure drop. SHS with a random distribution of roughness can be fabricated in a more scalable process such as spray coating and etched process. However, many of the studies are focused on SHS with periodic geometries that are not economically feasible in large scale applications. To address this important aspect a numerical simulation of turbulent flows over randomly patterned interfaces considering a range of texture was carried out recently which showed that randomness of texture arrangement increases the possibility of meniscus breakage as compared to the aligned case. This is because the post could face at least two times of interface deformation angles as those in the case of aligned posts [54].

Metallic surfaces, which have high hardness and corrosion resistance, such as nickel have great potential for real-life applications in harsh environments. The metallic hierarchical structures fabricated via a layer by layer method which combined laser interference lithography, photolithography, thermal reflow, nanoimprinting, and pulse-reverse-current electrochemical deposition were investigated for the effect of surface morphology on drag reduction over a large flow regime range. Comparing drag reduction for bare surface, a nanostructured surface, a micro-riblet surface, and a hierarchically structured surface of nanostructures on micro-riblets for nickel substrates, the maximum drag-reduction ratio was reported up to 36% for the hierarchically engineered surface that combines micro-riblet and nanostructures. Also, this process was based on a reapplication process that uses a re-usable metallic master, which implies that this process has the

potential for practical applications [55]. The turbulent flow drag reduction for SHS pipes is also studied experimentally and it's been shown that the drag reduction ranged from 8.3% to 17.8% could be attained for the Reynolds numbers ranging from 3000 to 11,000 [56].

A complete review of the recent experimental studies on SHS drag reduction is not presented in this report as they have been listed in a recent review paper by Liravi et al. [57]; the current advancements specifically for underwater drag reduction are also reviewed by Liu et al. [58].

### **2.1.3 Drag Reduction over SLIPS**

It's been shown that SLIPS is more stable than SHS and can repel a wider variety of liquids, however, SLIPS provides less drag reduction than SHS since the viscosity of the lubricant is greater than that of air. Rheometer drag reduction measurements on SLIPS in laminar flow with different working fluid viscosities demonstrated a drag reduction of 16% when the working fluid was 260 times more viscous than the lubricant [59]. In another analytical study, the drag reduction of SLIPS in laminar flow was investigated and it was found that a working fluid to lubricant viscosity ratio of 56 can attain a 20% flow increase on an optimized SLIPS [60]. In the evaluation of drag reduction effects, it should be noted that adding SLIPS to the inner surface of a pipe reduces its radius. The advantages of SLIPS would have to be greater than the added resistance of a decreased pipe radius.

Drag reduction of SLIPS for turbulent flow has been reported in the literature as well and demonstrated up to 14% drag reductions [61-63]. Analytical studies also demonstrated that confining lubricants on small scales may lead to additional drag reduction benefits [64]. The stability and thickness of the lubricant layer proved to be critical to drag reduction in SLIPS [65]. When the working droplets are moving above the critical speed on a stable lubricant layer the working fluid droplets could be lifted to the top of the lubricant layer [66]. So the properties of the SLIPS can be designed to improve the stability of the lubricant layer by enhancing the droplet motion.

The experimental studies on pressure-driven flows over the SLIPS are limited and the majority of them have only focused on lubricant depletion through textured under the applied pressure rather than quantification of hydrodynamic drag. Another numerical study investigated the drag reduction capabilities of SLIPS for a large parameter range of Reynolds numbers 1–1000; viscosity ratio 0–1; constriction ratio 0.1–10 and lubricant fraction 0–1. In this study, the viscous effects of lubricant on the amount of slippage were captured through balancing the velocity continuity and shear stress at the liquid–lubricant interface. Effect of relevant non-dimensional flow and surface geometrical parameters on the slip length were studied for texture configurations such as posts and holes. Both surface structures demonstrated a considerable amount of dissipation in the lubricant phase for a viscosity ratio greater than 0.1. The effective slip length decreased substantially for viscosity ratios greater than 0.1 when compared to viscosity ratios less than 0.1. However, an increased viscosity ratio between the lubricant and liquid improved the performance of the posts compared to holes at low-lubricant fractions. The inertial effects on the effective slip length were reduced with an increase in viscosity of the underlying lubricant, for a surface covered with holes compared to posts [67].

## **2.2 Fouling Reduction**

Bioinspired SHS and SLIPS present unique features such as self-cleaning, waterproofing, anti-microbial, anti-corrosion, anti-fouling, and anti-icing properties. Anti-fouling, easy-to-clean and self-cleaning surfaces offer a diverse application in medical equipment [68-70], building materials [71], fabrics [72,73] water pipelines, filters/purification membranes [74], water/oil separation [75], and marine sectors [76-78]. Wherever contaminants could harm the aesthetic, hygienic, or technical operation of the surface these properties help to maintain an operational surface and a reduction in cleaning costs. Various nonwetting surfaces have shown resistance to stains, proteins, bacteria, and marine organisms acting as an eco-friendly solution for fouling issues. While these surfaces are resistant to contamination, they do not affect other organisms present in their working environment. The ongoing studies on natural surfaces such as the hierarchical pattern of Saliva leaves [79] and the micropatterned surface of the Asian

tiger mosquito eggshell [80] have inspired the application of nonwetting surfaces for addressing fouling problems. Scardino et al. [81] have listed great biological samples that inspired the fundamental approaches for the fabrication of anti-fouling surfaces. The importance of surface morphology on antifouling properties is evident as settlement and attachment of particles diminished for structures smaller than the size of settling particle/cell. The new antifouling technologies could be made by combining surface chemistry and surface topographies. Surface wettability also has shown great effects on settlement and attachment processes. Self-cleaning surfaces could be designed by combining the hydrophobic coatings with a high aspect ratio structuring to trap a plastron layer for drag and adhesion reduction [82-84]. However, the plastron layer needs to be preserved so the desired low-drag properties could be sustained [85,86]. It's been shown that for underwater conditions, upon deprivation of the air/vapor cushion, the self-cleaning property of the surface could be lost [87]. Besides a nano-scaled structured superhydrophobic coating could discourage the settlement of all fouling organisms tested [88].

To assure the actual performance of the engineered surfaces in real-life applications, they should be tested in flow conditions as the actual application environment is complex and cannot be completely simulated in the laboratory. The flow could affect material surface properties, particle settlement preferences, and the interactions at the flow and nano/micro-scale structures' interface [88-90]. Moreover, the durability of the anti-fouling surface is very important for its real-life applications. Surfaces with micro/nanoscale structures could be very delicate and prone to destruction therefore, the wear resistance and self-healing properties of the antifouling surface should be considered in their design process.

In a recent review paper, Li et al. [91] have covered a comprehensive investigation on nonwetting surfaces for antifouling applications; including SHS and SLIPS for common and underwater utilizations. In this review, other contemporary studies not included in Li's review paper, and specifically those which are focused on the application of metallic surfaces for antifouling purposes are covered. As solid metallic surfaces have higher surface energy by nature and also because the low-surface-energy coating needed for making nonwetting surface generally has a weak adhesion to the metallic hierarchical

microstructures, it is more difficult to obtain superamphiphobic metallic surfaces than non-metallic surfaces.

### **2.2.1 Antifouling**

Anti-fouling properties could be divided into a few different categories: Self-cleaning, anti-scaling, and anti-bacterial/ biological adhesion. Self-cleaning is one of the special features of some nonwetting surfaces, where the pollutants on the surface are easily dissolved or attached into the liquid, and the dirt on SHS/SLIPS could be taken away by the working liquid due to the surface energy reduction [92].

Surfaces with nanostructures provide enhanced antifouling properties while their wetting properties do not influence the outcome. It is well known that on SHS water droplets could slide/roll and clear particles from surfaces due to the friction force reduction between water droplets and the surface. Heckenthaler et al. [93] studied the effect of surface morphology on the attachment and detachment forces exerted on particles sitting over a surface during the self-cleaning mechanism. They tested four Si-based samples including both smooth and nanotextured hydrophilic and hydrophobic surfaces; surfaces with higher hydrophobicity (nanotextured surfaces) demonstrated a superior particle removal efficiency. The particle removal enhancement is not only affected by low friction between the SHS and the droplets but also, is improved by the adhesion force reduction between them. Besides, the altered geometry of the air-particle-liquid interface increases the tension force acting on the particles sitting over the SHS therefore particles could be detached from the surface. Based on this investigation, a criterion for particle removal was derived which could be used for evaluation of the self-cleaning efficiency of other surfaces and designing the proper surface characteristics for a variety of particle removal situations.

### **2.2.2 Anti-Scaling**

Several industrial processes are susceptible to scale formation due to inorganic salts deposition. Scale buildups could cause operational complications and hindering production efficiency. Surface engineering and modifications that could withstand scaling environments are an active area of anti-fouling studies [94]. Sousa et al. [95] investigated the anti-scaling over SLIPS. They developed SLIPS through silicon oil infusion into porous electropolymerized and silanized polyaniline. The textured surface was modified through silanization to enhance the silicon oil infusion and prevent oil leakage during the operation and cleaning stages. The prepared surface was immersed into a brine for a period of 16 h to test its scaling properties. The scanning electronic microscopy (SEM) results showed clear anti-scaling properties. The oil coverage on the micro-textured surface lowered the energy barrier for scale formation as it retards scale deposition over oil/working fluid interface and make the particles flowing rather than scaling over the surface. The effect of the surface structure on the scaling process was investigated and it was shown that the smoothest structures enhanced the scale inhibition the most. On the other hand, the silanized derivative sample, with the lowest degree of wettability, showed the maximum scaling. Based on their thermodynamic calculations, they showed that surface-liquid energy for the hydrophobic surface is higher than the surface-deposit-liquid energy leading to more scale deposition and a higher degree of fouling for these surfaces. They also, suggested that impregnating the silanized surface with perfluorinated oils could reduce the adhesion of the crystals onto the surface.

### **2.2.3 Anti-Bacterial/Biological Adhesion**

The effect of surface morphology on the anti-fouling property of metallic surfaces has been presented in the literature. Kim et al. [96] fabricated an SHS using a replica anodic aluminum oxide (AAO) template. The antifouling properties of the developed surface were compared against an aluminum and a polytetrafluoroethylene (PTFE) surface for 3T3-Swiss albino cells growth. The aluminum and PTFE surface developed fouling within 3 days while it was hard for cells to attach to the SHS. It was demonstrated that the high resistance of SHS to cell adhesion is correlated with the surface hydrophobicity

property. The anti-biofouling property of a superhydrophobic surface is associated with the air layer entrapped in the surface structure which reduces the contact area between the bacteria and the surface. The plastron layer also could mitigate the adhesion forces acting on the bacterium by the surface making it hard for bacteria to attach to the surface. Hwang et al. [97] studied antifouling properties for a sturdy superhydrophobic surface fabricated from 1H,1H,2H,2H perfluorooctyltriethoxysilane, P25 TiO<sub>2</sub> nanoparticles. Their study showed that the plastron layer could be diminished when superhydrophobic surfaces were immersed in water for a long time and this could lead to excessive bacterial adhesion on the surface. It was suggested that SHS could encourage bacterial adhesion during long term exposure. Whenever superhydrophobicity effects were short-lived, due to air layer dissolution in water, the high roughness of SHS becomes a favorable environment for bacterial colonization. In a 24 hr testing time frame, the number of bacteria attached to the SHS was considerably higher than other substrates, and bacterial removal for these surfaces was harder as well. SHS stability has a crucial role in the antifouling property of the surface; if plastron stability is lost, the removal of fouling could be harder than a smooth surface.

DLVO (Derjaguin, Landau, Verwey, Overbeek) theory is used to explain the mechanism of bacterial interaction with a surface. Van der Waals's attractive and repulsive forces between the electrical double layer of the cell and the surface lead to particle adhesion [98,99] As SHS are nonpolar and have low surface energy, their interaction with bacteria is controlled by the electrostatic repulsive forces of the cell surface protein. The bacterial adhesion is also affected by the surface wettability and contact area where the presence of the plastron layer decreases the wettability and contact area leading to better bactericide properties [100].

Biofilms form in two steps; at first, the bacteria cell interacts with the material surface in a fast and reversible process. In the next step proteins on the bacterial surface start binding molecules with the surface in a chemical process, which is typically irreversible and leads to complete coverage of the surface by biofilm [99]. To fully understand anti-biofouling properties, the foulant substance, and its behavior over the surface should be investigated as well. For the case of bacteria, it's been suggested that the nano-pillars of the surface could pierce the membrane and destroy the bacteria. The anti-bacterial

investigation of some bacteria showed that a combination of adhesion and shear force plays a role in cell rupture demonstrating the influence of nanostructure geometry. The anti-biofouling characteristics of SHS is not a chemical interaction but rather is a physical one. Nanostructured surfaces have a higher contact area, so they pose a higher adhesion force on particles subject them to higher stretching and bending values. These forces are more pronounced in the areas between the pillars and cause more bacterial membrane rupture [101]. An increase in surface roughness enhances the bactericidal property of a nanostructured surface. The stretching modulus of bacteria's membrane varies from one bacteria to another one and this makes different bacteria more or less susceptible to the bactericide effect of the surface structure [101]. Moreover, environmental conditions could affect the mechanical properties of the bacterial membrane [102].

Shahi et al. [103] developed a polymeric superhydrophobic surface through biological nano-scaffolds (BNS) that exhibits superior anti-biofouling performance. They have assembled Tobacco mosaic virus (TMV)-templated metallic nano scaffolds, on gold surfaces. To obtain a complex micro-nano scale structured SHS, the surface was coated with a polymer solution. Biofouling testing for the BNS-based superhydrophobic surfaces and plain substrates in 48 hours showed up to a 6 times reduction in biofilm adhesion for the SHS. This anti-biofouling enhancement was associated with the complex surface morphology and its antiadhesion properties.

To fully investigate the antibacterial property of a surface, the bacteria size, shape, and surface morphology and, wettability should be considered. Pan et al. [104] fabricated an antibacterial SHS on AISI 420 martensitic stainless-steel plates through picosecond laser texturing. The laser-textured surface had a nano-microstructure with superhydrophobic properties in air and superaerophilicity underwater. The prepared surface could inhibit up to 99% for *Escherichia coli* adhesion and 93% for *Staphylococcus aureus* under vibration conditions. Almost no bacteria adhesion was observed under a stationary state. The laser-textured superhydrophobic surface demonstrated robust mechanical stability and advanced anti-corrosion properties. The antibacterial durability could be extended considerably when deep cleaning was performed after each dipping time in the bacterial suspension. The hierarchical micro-nano structures maintained a robust air layer over the surface contributing to the

antibacterial mechanism. Their study clarified the effect of the grooves size and bacteria's characteristics on antibacterial property. Upon air layer disruption, micro-sized grooves could allow the entrance of coccoid-shaped *S. aureus* (approximately 700 nm) and rod-shaped *E. coli* (2  $\mu\text{m}$ ) and provide them with colonization opportunity. Moreover, the bacteria shape makes it easier for *S. aureus* to get into the micro-sized grooves for enhanced colonization. On the other hand, for the long rod-shaped *E. coli*, this process is not that straightforward, this factor leads to an enhanced anti-adhesion performance of the laser textured SHS for *E. coli* [99,105].

Studies in the literature suggest that in addition to surface roughness, structures pattern could also contribute to the antibacterial properties of the surface [106,107]. Surface modifications such as patterning [108] or shot peening [109], finishing via magnetorheological abrasive flow [110] have shown a reduction in bacterial adhesion. These processes form hierarchical structures on the surface promoting a stable Cassie wetting state which makes the prolonged antifouling properties possible. Pechook et al. [111] achieved antifouling properties against *Pseudomonas aeruginosa* (Gram-negative) and *Bacillus cereus* (Gram-positive) biofilms through surface modification without application of any toxic biocides. Gupta et al. [112] employed nanosecond laser texturing to form a re-melted layer with a wavy pattern on a 304 L SS surface to fabricate a nanostructure SHS. *Pseudomonas sp.* and *Bacillus flexus* which are two of the predominant biofilm formers in the freshwater reservoirs were used for exposure testing for 6 h. Bacteria density over the prepared laser-treated surfaces was two orders of magnitude less than the untreated surface for both Gram-positive and Gram-negative bacteria. Laser texturing changed the surface with re-melting layer formation and adding micro-pits, and bumpy structures which contributed to bacteria adhesion reduction properties of the surface. In addition to antibacterial features, the prepared surface showed a significant corrosion resistance.

Robust metallic surfaces with broad-spectrum self-cleaning functions are in high demand. Depending on the application, surfaces having diverse strong pollutant-resistances including decomposing organic substances, sterilizing, anti-fouling, and good mechanical durability are desired. Shen et al. [113] adopted a composite electrodeposition process to prepare multifunctional self-cleaning metallic surfaces by

introducing tungsten trioxide (WO<sub>3</sub>) nanoparticles and carbon nanotubes (CNTs) into the deposited nickel metal, forming the Ni/nano-WO<sub>3</sub>/CNTs metal matrix composite (MMC) coating. It was found that the MMC coating shows a unique micro-nano-scale dual hierarchical surface structure with overhanging microstructures, being superhydrophilic in its as-plated state and superamphiphobic after it is modified. The prepared Ni/nano-WO<sub>3</sub>/CNTs MMC coating shows an excellent anti-bacterial function due to the dual anti-bacterial effects of the introduced WO<sub>3</sub> nanoparticles (photocatalytic degradation effect) and CNTs (physical destroy effect). MMC coating is significantly resistant to pollution. The Ni/nano-WO<sub>3</sub>/CNTs MMC coating surface possesses transferable extreme wettability and thus shows broad-spectrum anti-fouling and antibacterial properties as well as good mechanical durability.

Zhang et al. [114] developed a superhydrophobic EP-PTFE/GP-SiO<sub>2</sub>-POTS coating on the steel surface through electrostatic spraying. The prepared surface was mechanically stable and exhibited self-cleaning and anti-fouling properties in a slurry. The nano-micro-nano structure of this surface could prevent water diffusion into the coating which caused the surface to maintain a stable air layer for up to 60 days. This stable plastron preserves superhydrophobicity of the surface leading to a reduction in the contact area and adhesion of fouling substance.

Manoj et al. [115] fabricated an SHS on a titanium surface through simultaneous anodization and adsorption. The surface was exposed to microbial cultures of *Pseudomonas* sp. and *Bacillus* sp. for 48 h and bacterial adhesion was reduced by 50% in comparison with the untreated Ti surface. The surface also showed chemical and mechanical stability and self-cleaning characteristics via bouncing dirt removal which makes it perfect for marine engineering applications. The bacterial adhesion on the prepared SHS was low because only 3% of the surface was available for bacterial attachment (solid-liquid area fraction for the prepared SHS was 0.03). Also, other factors such as detachment of bacteria through fluid flow [116], and detergent properties of the myristic acid over the SHP surface [117] could contribute to the anti-bacterial properties of this surface.

#### 2.2.4 Antifouling for SLIPS

SLIPS provide an alternative approach to anti-fouling materials; the flowability of the oil layer leads to self-healing and enables a sustained antifouling effect [118,119]. These surfaces could function under high-pressure conditions [119], provide self-healing [119], optical transparency [120], delay ice nucleation [121] and repel fluids such as crude oil and brine [121,122], blood or biofilms [120,121,123,124]. SLIPS could be fabricated from a broad range of inexpensive materials by infusing lubricating oils into rough micro/nanostructured substrates [119]; however, approaches for developing metallic SLIPS without significant reduction in durability are limited which makes SLIPS usage very limited in demanding applications. Tesler et al. [125] employed electrodeposition of nanoporous tungsten oxide (TO) films to fabricate anti-fouling steel surfaces. The SLIPS was then prepared by the infiltration of fluorinated TO-SHS with perfluoropolyether lubricants. The TO-textured steels showed to have comparable mechanical durability as bare steel. The lubricant infused surface demonstrated omniphobicity against highly contaminating media while maintaining their exceptional mechanical durability. The as-prepared surfaces exhibited high anti-fouling features when tested against adhesion of marine algal biofilm, *Escherichia coli* attachment, and blood staining. The TO-SLIPS provides adequate qualities which make it an excellent candidate for real-life applications under harsh environmental and fouling conditions.

Ouyang et al. [126] used a facile electrodeposition approach to construct dendritic Ag crystals onto a Ti substrate. The prepared surface showed superhydrophobicity and superoleophilicity. Then the SLIPS was made through dimethyl silicone oil infusion. The proposed SLIP shows anti-biofouling properties killing water-borne microorganisms without any toxic material application or external energy usage. To evaluate the biofouling properties, the SLIPS and plain Ti surface were immersed for 14 days in samples containing diatom and green algae *Chlorella Vulgaris*. It was demonstrated that the number of microorganisms on the SLIPS was 4 orders of magnitude less than bare Ti substrate. The surface also showed corrosion resistance which made it a suitable material for seawater pipeline systems.

Nonwetting surface application in oil-water separation has gained lots of attention in recent years. As these surfaces are subject to high marine biofouling conditions the anti-

fouling properties of the developed surfaces are of high importance. Deng et al. [127] developed a superhydrophobic lauric acid-modified  $\text{Cu}(\text{OH})_2$  (LAMC) coating which could be applied to various substrates via spraying or dipping process. The LAMC coating showed self-cleaning and mechanical stability properties which could make it a promising protective coating for ships and walls. In this study, they demonstrated the anti-fouling properties of an LAMC coated copper mesh as a high-efficiency oil-water separation sponge.

Sun et al. [128] studied two modification methods for commercial melamine sponges (MS) to enhance its absorption capacity for oil-water separation purposes. Graphene oxide (GO) or GO-based nanocomposites (NCs) sheets and Ag/RGO NC were separately applied to MS via a combined chemical reduction and immersion process. The coating process transformed the superhydrophilic MS into hydrophobic surfaces that are recyclable. The prepared surfaces showed absorption capacity enhancement and antibacterial performance against different groups of commonly existing bacteria in the seawater. The antibacterial properties of the surface are explained through multiple effects including bactericide effects of the RGO sheets and Ag NPs, and continuous delivery of the silver ions, preserving the antibacterial performance of the Ag/RGO-MS. It's been shown that the sharp edges of the RGO sheets can puncture the bacterial cell membrane, which leads to cell death [129]. The RGO sheets also can disrupt bacterial metabolism, causing cell inactivation [130].

Zhao et al. [131] fabricated a slippery liquid-infused polyethylene terephthalate (SLI-PET) membrane through a facile method for oil-water separation. The prepared membranes exhibited high oil-water separation efficiency, excellent antifouling, and recyclability. The membranes received silica nanoparticles (SiNPs) then went through the fluorination process and oil infusion. Investigation on lubricant properties showed that stable SLIPS can't be achieved with the lubricants of high volatility and low viscosity however a slight improvement in the fouling resistance of the membrane could be obtained. On the other hand, membranes infused with low volatility and high viscosity oils demonstrated strong stability even under evaporation or flowing immersion. The lubricant layer has a prime effect on the antifouling properties of the membrane and a more stable lubricant layer provides better anti-pollution performance.

## 2.3 Corrosion Resistance

The chemical and electrochemical reactions of metals with their environment lead to corrosion which has a considerable impact on their industrial applications. Corrosion within the systems is known to degrade the system's energy efficiencies and reliabilities and add to maintenance costs. Corrosion may shorten the lifespan of the system, result in metal oxides deposition on other system parts leading to overheating and failure problems. Therefore, corrosion control throughout systems such as powerplant steam/condensate system is imperative. Corrosion inhibitors, including neutralizing and filming agents are the common solutions that should be specifically tailored based on the system and its working environment for each project. However, these chemical approaches have raised safety concerns for the downstream systems communicating with the main medium [132]. It's believed that nonwetting surfaces could provide an eco-friendly solution to the corrosion problem as the surface morphology alone without any need for chemical additives could remedy the issue. The superhydrophobic structure enhances the anti-corrosion characteristics of the surface through increasing the surface air fraction and also reducing the actual area of a rough surface in contact with corrosive solution [133]. Superhydrophobic coatings on the surface protect them from environmental moisture and inhibit the electrochemical reactions as the entrapped air pockets in the structured surface prevents the transmission of electron and ion between the substrate and electrolyte. Also, the Laplace pressure exerted by the plastron could push out the corrosive liquid from surface cavities [58]. There has been extensive research on the SHS and SLIPS surfaces with anti-corrosion features. Superhydrophobic coatings are developed for many of prevalent metal surfaces such as aluminum [134-136], copper [137,138], steel [139], titanium [140], zinc [141,142] and magnesium [133]. SLIPS with corrosive resistance properties are also developed and shown to be a promising approach for corrosion inhibition [143,144]. In SLIPS, all the preventive roles played by the plastron layer in SHS are performed by the lubricant layer entrapped on the structured surface.

Yao et al. [145] provided a recent review on various methods used to fabricate corrosion-resistant coatings for magnesium alloys. In another recent study, Darband et al. [146] presented a comprehensive review for the corrosion resistance of

superhydrophobic surfaces fabricated by different methods and compared the outcomes for the surface stability and corrosion resistance. Based on this comparative study they demonstrated that as the wetting contact angle of the surface increases, its corrosion resistance gets improved.

Implementation of SHS and SLIPS as corrosion resistance solutions for real-life applications is bounded by the stability of these surfaces during their service life in practice. Plastron and hierarchical structure stability play an important role in corrosion resistance sustainability of SHS coatings. Self-healing properties of SHS or SLIPS could expand the longevity of these surfaces and make their scaled-up applications possible. However, the majority of studies on the self-healing properties of SHS are focused on polymer materials which limits their applications for metallic surfaces. SLIPS, on the other hand, provide a suitable approach as the lubricant fluidity enhance the self-healing features and could be applied to a variety of metallic surfaces.

## **2.4 Anti-Fogging and Anti-Icing**

Nonwetting surfaces offer a variety of beneficial features including anti-fogging and anti-icing which makes them appealing to many industrial and everyday use applications. Consequently, the pool of literature on these topics is rich. Anti-fogging surfaces have been fabricated as SHS and SLIPS [147-149,121]. Also, these surfaces have been investigated as a means of fog collection to generate water from fog where liquid water drops are collected without any phase change phenomena [150,151]. Superhydrophobicity of these surfaces makes them excellent water repellent and therefore prevents accumulation or pinning of the condensate water on them. Comparison studies on SHS and SLIPS showed that SLIPS have a higher water collection rate from the fog as compared to SHS. However, contamination of the collected water with leaked lubricant could be a disadvantage for water harvesting from fog via SLIPS [152]. It has been also shown that hybrid surfaces with superhydrophilic/superhydrophobic patterns have higher fog collection efficiency than uniform superhydrophilic surfaces, uniform superhydrophobic surfaces, and untreated hydrophilic surfaces [153]. The fog collection ability of the patterned surfaces varies for different metal substrates; patterned Steel

surface showed the highest fog collection efficiency, followed by Cu, Ti, and the lowest is shown on Al. demonstrating that fog collection efficiency improves with the reduction in surface energy [153].

Moreover, anti-icing surfaces have a diverse application in aviation systems, renewable energy systems such as wind turbines, solar panels, and many more industrial applications, building and construction materials. Recent anti-icing advancements are reviewed by Esmeryan [154] highlighting the impact of nonwetting surfaces as their application typically do not cause surface damage due to chemical usage and do not need energy consumption for their anti-icing function. Superhydrophobic surfaces, prevent droplet pining on the surface promoting water droplets to roll off before freezing. The development of anti-icing SHS has been reviewed by Yancheshme et al. [155]. Mechanical stability of these surfaces plays an important role in scaling up their fabrication for industrial applications. In a SLIPS, the immiscible lubricant film enhances the removal of the accumulated ice without any damage to the surface. Also, the self-healing properties of SLIPS could promote their durability when exposed to harsh environments. Wang et al. [156] presented a comprehensive review on ice repelling SLIPS. In general, nonwetting surfaces provide passive icing protection through different mechanisms including water repellence, delayed ice nucleation, and ice adhesion reduction. The ice formation on the superhydrophobic surface depends on several factors such as surface roughness, contact area, temperature, and surface thermodynamics. The anti-icing mechanisms of the SHS and SLIPS have been investigated by Irajizad et al. [157] in a recent review paper. Latthe et al. [158] also provided a review covering the recent progress in passive anti-icing coating materials and methodologies for metal substrates, polymers, and nanoparticles/polymer composites. Passive superhydrophobic icing protection is proposed in the literature for a variety of metal surfaces such as aluminum [159-162], copper [163], and steel [164].

## 2.5 References

1. Choi, C.H., Westin, K.J.A. and Breuer, K.S., 2003. Apparent slip flows in hydrophilic and hydrophobic microchannels. *Physics of fluids*, 15(10), pp.2897-2902.
2. Neto, C., Evans, D.R., Bonaccorso, E., Butt, H.J. and Craig, V.S., 2005. Boundary slip in Newtonian liquids: a review of experimental studies. *Reports on progress in physics*, 68(12), p.2859.
3. Rothstein, J.P., 2010. Slip on superhydrophobic surfaces. *Annual Review of Fluid Mechanics*, 42, pp.89-109.
4. Lee, C., Choi, C.H. and Kim, C.J., 2016. Superhydrophobic drag reduction in laminar flows: a critical review. *Experiments in Fluids*, 57(12), p.176.
5. Lee, C. and Choi, C.H., 2008. Structured surfaces for a giant liquid slip. *Physical review letters*, 101(6), p.064501.
6. Daeian, M.A., Moosavi, A., Nouri-Borujerdi, A. and Taghvaei, E., 2017. Drag reduction in a channel with microstructure grooves using the lattice Boltzmann method. *Journal of Physics D: Applied Physics*, 50(10), p.105301.
7. Mohammadi, A. and Floryan, J.M., 2015. Numerical analysis of laminar-drag-reducing grooves. *Journal of Fluids Engineering*, 137(4).
8. Samaha, M.A., Vahedi Tafreshi, H. and Gad-el-Hak, M., 2011. Modeling drag reduction and meniscus stability of superhydrophobic surfaces comprised of random roughness. *Physics of fluids*, 23(1), p.012001.
9. Cottin-Bizonne, C., Barentin, C. and Bocquet, L., 2012. Scaling laws for slippage on superhydrophobic fractal surfaces. *Physics of fluids*, 24(1), p.012001.
10. Kang, M., Lee, J.W. and Kang, Y.T., 2016. Reduction of liquid pumping power by nanoscale surface coating. *International Journal of Refrigeration*, 71, pp.8-17.
11. Byun, D. and Park, H.C., 2006, December. Drag reduction on micro-structured superhydrophobic surface. In 2006 IEEE International Conference on Robotics and Biomimetics (pp. 818-823). IEEE.
12. Daniello, R.J., Waterhouse, N.E. and Rothstein, J.P., 2009. Drag reduction in turbulent flows over superhydrophobic surfaces. *Physics of Fluids*, 21(8), p.085103.
13. Ahmmed, K.T. and Kietzig, A.M., 2016. Drag reduction on laser-patterned hierarchical superhydrophobic surfaces. *Soft Matter*, 12(22), pp.4912-4922.

14. Taghvaei, E., Moosavi, A., Nouri-Borujerdi, A., Daeian, M.A. and Vafaeinejad, S., 2017. Superhydrophobic surfaces with a dual-layer micro-and nanoparticle coating for drag reduction. *Energy*, 125, pp.1-10.
15. Biben, T. and Joly, L., 2008. Wetting on nanorough surfaces. *Physical review letters*, 100(18), p.186103.
16. Ng, C.O. and Wang, C.Y., 2009. Stokes shear flow over a grating: implications for superhydrophobic slip. *Physics of Fluids*, 21(1), p.087105.
17. Gao, P. and Feng, J.J., 2009. Enhanced slip on a patterned substrate due to depinning of contact line. *Physics of Fluids*, 21(10), p.102102.
18. Forsberg, P., Nikolajeff, F. and Karlsson, M., 2011. Cassie–Wenzel and Wenzel–Cassie transitions on immersed superhydrophobic surfaces under hydrostatic pressure. *Soft Matter*, 7(1), pp.104-109.
19. Emami, B., Hemeda, A.A., Amrei, M.M., Luzar, A., Gad-el-Hak, M. and Vahedi Tafreshi, H., 2013. Predicting longevity of submerged superhydrophobic surfaces with parallel grooves. *Physics of Fluids*, 25(6), p.062108.
20. Park, H. and Sun, G., 2014. Superhydrophobic turbulent drag reduction as a function of surface grating parameters. *Journal of Fluid Mechanics*, 747, pp.722-734.
21. Steinberger, A., Cottin-Bizonne, C., Kleimann, P. and Charlaix, E., 2007. High friction on a bubble mattress. *Nature materials*, 6(9), pp.665-668.
22. Amrei, M.M. and Tafreshi, H.V., 2015. Effects of hydrostatic pressure on wetted area of submerged superhydrophobic granular coatings. Part 1: mono-dispersed coatings. *Colloids and Surfaces A: Physicochemical and Engineering Aspects*, 465, pp.87-98.
23. Emami, B., Bucher, T.M., Tafreshi, H.V., Pestov, D., Gad-el-Hak, M. and Tepper, G.C., 2011. Simulation of meniscus stability in superhydrophobic granular surfaces under hydrostatic pressures. *Colloids and Surfaces A: Physicochemical and Engineering Aspects*, 385(1-3), pp.95-103.
24. Piao, L. and Park, H., 2015. Two-dimensional analysis of air–water interface on superhydrophobic grooves under fluctuating water pressure. *Langmuir*, 31(29), pp.8022-8032.
25. Samaha, M.A., Tafreshi, H.V. and Gad-el-Hak, M., 2012. Effects of hydrostatic pressure on the drag reduction of submerged aerogel-particle coatings. *Colloids and Surfaces A: Physicochemical and Engineering Aspects*, 399, pp.62-70.

26. Phan, H.T., Caney, N., Marty, P., Colasson, S. and Gavillet, J., 2011. Flow boiling of water in a minichannel: The effects of surface wettability on two-phase pressure drop. *Applied Thermal Engineering*, 31(11-12), pp.1894-1905.
27. Lee, C.Y. and Lee, S.Y., 2010. Pressure drop of two-phase dry-plug flow in round minichannels: Effect of moving contact line. *Experimental Thermal and Fluid Science*, 34(1), pp.1-9.
28. Wang, Y., Al Shakhshir, S., Li, X. and Chen, P., 2014. Superhydrophobic flow channel surface and its impact on PEM fuel cell performance. *International Journal of Low-Carbon Technologies*, 9(3), pp.225-236.
29. Samaha, M.A., Vahedi Tafreshi, H. and Gad-el-Hak, M., 2012. Sustainability of superhydrophobicity under pressure. *Physics of Fluids*, 24(11), p.112103.
30. Emami, B., Tafreshi, H.V., Gad-el-Hak, M. and Tepper, G.C., 2011. Predicting shape and stability of air–water interface on superhydrophobic surfaces with randomly distributed, dissimilar posts. *Applied Physics Letters*, 98(20), p.203106.
31. Xiang, Y., Xue, Y., Lv, P., Li, D. and Duan, H., 2016. Influence of fluid flow on the stability and wetting transition of submerged superhydrophobic surfaces. *Soft Matter*, 12(18), pp.4241-4246.
32. Xiang, Y., Huang, S., Lv, P., Xue, Y., Su, Q. and Duan, H., 2017. Ultimate stable underwater superhydrophobic state. *Physical review letters*, 119(13), p.134501.
33. Xu, M., Sun, G. and Kim, C.J., 2014. Infinite lifetime of underwater superhydrophobic states. *Physical review letters*, 113(13), p.136103.
34. Shirtcliffe, N.J., McHale, G., Newton, M.I., Perry, C.C. and Pyatt, F.B., 2006. Plastron properties of a superhydrophobic surface. *Applied Physics Letters*, 89(10), p.104106.
35. Domingues, E.M., Arunachalam, S., Nauruzbayeva, J. and Mishra, H., 2018. Biomimetic coating-free surfaces for long-term entrapment of air under wetting liquids. *Nature communications*, 9(1), pp.1-11.
36. Lee, C. and Kim, C.J.C., 2009. Maximizing the giant liquid slip on superhydrophobic microstructures by nanostructuring their sidewalls. *Langmuir*, 25(21), pp.12812-12818.
37. Barthlott, W., Schimmel, T., Wiersch, S., Koch, K., Brede, M., Barczewski, M., Walheim, S., Weis, A., Kaltenmaier, A., Leder, A. and Bohn, H.F., 2010. The Salvinia paradox: superhydrophobic surfaces with hydrophilic pins for air retention under water. *Advanced Materials*, 22(21), pp.2325-2328.
38. Carlborg, C.F. and van der Wijngaart, W., 2011. Sustained superhydrophobic friction reduction at high liquid pressures and large flows. *Langmuir*, 27(1), pp.487-493.

39. Choi, W., Byeon, H., Park, J.Y., Kim, I.C. and Lee, S.J., 2019. Effects of pressure gradient on stability and drag reduction of superhydrophobic surfaces. *Applied Physics Letters*, 114(10), p.101603.
40. Carlborg, C.F., Do-Quang, M., Stemme, G., Amberg, G. and van der Wijngaart, W., 2008, January. Continuous flow switching by pneumatic actuation of the air lubrication layer on superhydrophobic microchannel walls. In 2008 IEEE 21st International Conference on Micro Electro Mechanical Systems (pp. 599-602). IEEE.
41. Du, P., Wen, J., Zhang, Z., Song, D., Ouahsine, A. and Hu, H., 2017. Maintenance of air layer and drag reduction on superhydrophobic surface. *Ocean Engineering*, 130, pp.328-335.
42. Lee, C. and Kim, C.J., 2011. Underwater restoration and retention of gases on superhydrophobic surfaces for drag reduction. *Physical review letters*, 106(1), p.014502.
43. Lee, C. and Kim, C.J., 2012. Wetting and active dewetting processes of hierarchically constructed superhydrophobic surfaces fully immersed in water. *Journal of microelectromechanical systems*, 21(3), pp.712-720.
44. Lee, J. and Yong, K., 2015. Combining the lotus leaf effect with artificial photosynthesis: regeneration of underwater superhydrophobicity of hierarchical ZnO/Si surfaces by solar water splitting. *NPG Asia Materials*, 7(7), pp.e201-e201.
45. Vakarelski, I.U., Chan, D.Y. and Thoroddsen, S.T., 2014. Leidenfrost vapour layer moderation of the drag crisis and trajectories of superhydrophobic and hydrophilic spheres falling in water. *Soft Matter*, 10(31), pp.5662-5668.
46. Dilip, D., Kumar, S.V., Bobji, M.S. and Govardhan, R.N., 2018. Sustained drag reduction and thermo-hydraulic performance enhancement in textured hydrophobic microchannels. *International Journal of Heat and Mass Transfer*, 119, pp.551-563.
47. Wang, C., Tang, F., Li, Q., Zhang, Y. and Wang, X., 2017. Spray-coated superhydrophobic surfaces with wear-resistance, drag-reduction and anti-corrosion properties. *Colloids and Surfaces A: Physicochemical and Engineering Aspects*, 514, pp.236-242.
48. Hwang, G.B., Patir, A., Page, K., Lu, Y., Allan, E. and Parkin, I.P., 2017. Buoyancy increase and drag-reduction through a simple superhydrophobic coating. *Nanoscale*, 9(22), pp.7588-7594.
49. Park, H., Park, H. and Kim, J., 2013. A numerical study of the effects of superhydrophobic surface on skin-friction drag in turbulent channel flow. *Physics of Fluids*, 25(11), p.110815.

50. Newton, M., Brennan, J.C., Geraldi, N.R., Morris, R.H., Fairhurst, D. and McHale, G., 2015. Flexible conformable hydrophobized surfaces for turbulent flow drag reduction.
51. Aljallis, E., Sarshar, M.A., Datla, R., Sikka, V., Jones, A. and Choi, C.H., 2013. Experimental study of skin friction drag reduction on superhydrophobic flat plates in high Reynolds number boundary layer flow. *Physics of fluids*, 25(2), p.025103.
52. Rastegari, A. and Akhavan, R., 2019. On drag reduction scaling and sustainability bounds of superhydrophobic surfaces in high Reynolds number turbulent flows. *Journal of Fluid Mechanics*, 864, pp.327-347.
53. Costantini, R., Mollicone, J.P. and Battista, F., 2018. Drag reduction induced by superhydrophobic surfaces in turbulent pipe flow. *Physics of Fluids*, 30(2), p.025102.
54. Seo, J. and Mani, A., 2018. Effect of texture randomization on the slip and interfacial robustness in turbulent flows over superhydrophobic surfaces. *Physical Review Fluids*, 3(4), p.044601.
55. Kim, T., Shin, R., Jung, M., Lee, J., Park, C. and Kang, S., 2016. Drag reduction using metallic engineered surfaces with highly ordered hierarchical topographies: nanostructures on micro-riblets. *Applied Surface Science*, 367, pp.147-152.
56. Lv, F.Y. and Zhang, P., 2016. Drag reduction and heat transfer characteristics of water flow through the tubes with superhydrophobic surfaces. *Energy Conversion and Management*, 113, pp.165-176.
57. Liravi, M., Pakzad, H., Moosavi, A. and Nouri-Borujerdi, A., 2020. A comprehensive review on recent advances in superhydrophobic surfaces and their applications for drag reduction. *Progress in Organic Coatings*, 140, p.105537.
58. Liu, G., Yuan, Z., Qiu, Z., Feng, S., Xie, Y., Leng, D. and Tian, X., 2020. A brief review of bio-inspired surface technology and application toward underwater drag reduction. *Ocean Engineering*, 199, p.106962.
59. Solomon, B.R., Khalil, K.S. and Varanasi, K.K., 2014. Drag reduction using lubricant-impregnated surfaces in viscous laminar flow. *Langmuir*, 30(36), pp.10970-10976.
60. Schönecker, C., Baier, T. and Hardt, S., 2013. Influence of the enclosed fluid on the flow over a microstructured surface in the Cassie state. arXiv preprint arXiv:1311.7006.
61. Rosenberg, B.J., Van Buren, T., Fu, M.K. and Smits, A.J., 2016. Turbulent drag reduction over air-and liquid-impregnated surfaces. *Physics of Fluids*, 28(1), p.015103.
62. Fu, M.K. and Hultmark, M., 2015. A Model for Turbulent Drag Reduction Over Liquid Infused Micro textured Surfaces. Tech. rep., European Drag Reduction and Flow Control Meeting.

63. Wang, Y., Zhang, H., Liu, X. and Zhou, Z., 2016. Slippery liquid-infused substrates: a versatile preparation, unique anti-wetting and drag-reduction effect on water. *Journal of Materials Chemistry A*, 4(7), pp.2524-2529.
64. Jackson, R.L., 2010. A scale dependent simulation of liquid lubricated textured surfaces. *Journal of Tribology*, 132(2).
65. Scarratt, L.R., Zhu, L. and Neto, C., 2019. How Slippery are SLIPS? Measuring Effective Slip on Lubricated Surfaces with Colloidal Probe Atomic Force Microscopy. *Langmuir*, 35(8), pp.2976-2982.
66. Daniel, D., Timonen, J.V., Li, R., Velling, S.J. and Aizenberg, J., 2017. Oleoplaning droplets on lubricated surfaces. *Nature Physics*, 13(10), pp.1020-1025.
67. Sharma, H., Gaddam, A., Agrawal, A. and Joshi, S.S., 2019. Slip flow through microchannels with lubricant-infused bi-dimensional textured surfaces. *Microfluidics and Nanofluidics*, 23(2), p.28.
68. Banerjee, I., Pangule, R.C. and Kane, R.S., 2011. Antifouling coatings: recent developments in the design of surfaces that prevent fouling by proteins, bacteria, and marine organisms. *Advanced materials*, 23(6), pp.690-718.
69. Lee, M.J., Kwon, J.S., Jiang, H.B., Choi, E.H., Park, G. and Kim, K.M., 2019. The antibacterial effect of non-thermal atmospheric pressure plasma treatment of titanium surfaces according to the bacterial wall structure. *Scientific reports*, 9(1), pp.1-13.
70. Habash, M. and Reid, G., 1999. Microbial biofilms: their development and significance for medical device—related infections. *The Journal of Clinical Pharmacology*, 39(9), pp.887-898.
71. Kong, X., Zhang, J., Xuan, Q., Lu, J. and Feng, J., 2018. Superhydrophobic coating for antifouling of chinese paintings. *Langmuir*, 34(28), pp.8294-8301.
72. Yang, C., Liang, G.L., Xu, K.M., Gao, P. and Xu, B., 2009. Bactericidal functionalization of wrinkle-free fabrics via covalently bonding TiO<sub>2</sub>@ Ag nanoconjugates. *Journal of materials science*, 44(7), pp.1894-1901.
73. Meilert, K.T., Laub, D. and Kiwi, J., 2005. Photocatalytic self-cleaning of modified cotton textiles by TiO<sub>2</sub> clusters attached by chemical spacers. *Journal of molecular catalysis A: chemical*, 237(1-2), pp.101-108.
74. Ong, C.S., Goh, P.S., Lau, W.J., Misdan, N. and Ismail, A.F., 2016. Nanomaterials for biofouling and scaling mitigation of thin film composite membrane: A review. *Desalination*, 393, pp.2-15.

75. Si, Y., Guo, Z. and Liu, W., 2016. A robust epoxy resins@ stearic acid-Mg (OH) 2 micronanosheet superhydrophobic omnipotent protective coating for real-life applications. *ACS applied materials & interfaces*, 8(25), pp.16511-16520.
76. [9] Callow, J.A. and Callow, M.E., 2011. Trends in the development of environmentally friendly fouling-resistant marine coatings. *Nature communications*, 2(1), pp.1-10.
77. Almeida, E., Diamantino, T.C. and de Sousa, O., 2007. Marine paints: the particular case of antifouling paints. *Progress in Organic Coatings*, 59(1), pp.2-20.
78. Flemming, H.C., 2002. Biofouling in water systems—cases, causes and countermeasures. *Applied microbiology and biotechnology*, 59(6), pp.629-640.
79. Xiang, Y., Huang, S., Huang, T.Y., Dong, A., Cao, D., Li, H., Xue, Y., Lv, P. and Duan, H., 2020. Superrepellency of underwater hierarchical structures on *Salvinia* leaf. *Proceedings of the National Academy of Sciences*, 117(5), pp.2282-2287.
80. Kim, H., Sun, Y., Bae, C.G. and Moon, M.J., 2020. Structural characterization of the micropatterned egg plastron in the mosquito, *Aedes albopictus*. *Entomological Research*, 50(4), pp.189-198.
81. Scardino, A.J. and de Nys, R., 2011. Mini review: biomimetic models and bioinspired surfaces for fouling control. *Biofouling*, 27(1), pp.73-86.
82. Koc, Y., de Mello, A.J., McHale, G., Newton, M.I., Roach, P. and Shirtcliffe, N.J., 2008. Nano-scale superhydrophobicity: suppression of protein adsorption and promotion of flow-induced detachment. *Lab on a Chip*, 8(4), pp.582-586.
83. Ou, J. and Rothstein, J.P., 2005. Direct velocity measurements of the flow past drag-reducing ultrahydrophobic surfaces. *Physics of fluids*, 17(10), p.103606.
84. Liu, Y., Moevius, L., Xu, X., Qian, T., Yeomans, J.M. and Wang, Z., 2014. Pancake bouncing on superhydrophobic surfaces. *Nature physics*, 10(7), pp.515-519.
85. Hof, B., 2017. Water flows out of touch. *Nature*, 541(7636), pp.161-162.
86. Saranadhi, D., Chen, D., Kleingartner, J.A., Srinivasan, S., Cohen, R.E. and McKinley, G.H., 2016. Sustained drag reduction in a turbulent flow using a low-temperature Leidenfrost surface. *Science advances*, 2(10), p.e1600686.
87. Zhang, H., Lamb, R. and Lewis, J., 2005. Engineering nanoscale roughness on hydrophobic surface—preliminary assessment of fouling behaviour. *Science and Technology of Advanced Materials*, 6(3-4), pp.236-239.
88. Scardino, A.J., Zhang, H., Cookson, D.J., Lamb, R.N. and Nys, R.D., 2009. The role of nano-roughness in antifouling. *Biofouling*, 25(8), pp.757-767.

89. Marmur, A., 2006. Super-hydrophobicity fundamentals: implications to biofouling prevention. *Biofouling*, 22(02), pp.107-115.
90. Genzer, J. and Efimenko, K., 2006. Recent developments in superhydrophobic surfaces and their relevance to marine fouling: a review. *Biofouling*, 22(5), pp.339-360.
91. Li, Z. and Guo, Z., 2019. Bioinspired surfaces with wettability for antifouling application. *Nanoscale*, 11(47), pp.22636-22663.
92. Yu, M., Chen, S., Zhang, B., Qiu, D. and Cui, S., 2014. Why a lotus-like superhydrophobic surface is self-cleaning? An explanation from surface force measurements and analysis. *Langmuir*, 30(45), pp.13615-13621.
93. Heckenthaler, T., Sadhujan, S., Morgenstern, Y., Natarajan, P., Bashouti, M. and Kaufman, Y., 2019. Self-cleaning mechanism: Why nanotexture and hydrophobicity matter. *Langmuir*, 35(48), pp.15526-15534.
94. Huang, G., Wang, D., Ma, S., Chen, J., Jiang, L. and Wang, P., 2015. A new, low-cost adsorbent: Preparation, characterization, and adsorption behavior of Pb (II) and Cu (II). *Journal of Colloid and Interface Science*, 445, pp.294-302.
95. Sousa, M.F.B., Barbosa, G.F., Signorelli, F. and Bertran, C.A., 2017. Anti-scaling properties of a SLIPS material prepared by silicon oil infusion in porous polyaniline obtained by electropolymerization. *Surface and Coatings Technology*, 325, pp.58-64.
96. Kim, D., Park, M., Park, J. and Hwang, W., 2009, May. Cell adherence and growth on a fabricated superhydrophobic surface. In 2009 IEEE International Conference on Computational Intelligence for Measurement Systems and Applications (pp. 230-233). IEEE.
97. Hwang, G.B., Page, K., Patir, A., Nair, S.P., Allan, E. and Parkin, I.P., 2018. The anti-biofouling properties of superhydrophobic surfaces are short-lived. *ACS nano*, 12(6), pp.6050-6058.
98. Hermansson, M., 1999. The DLVO theory in microbial adhesion. *Colloids and surfaces B: Biointerfaces*, 14(1-4), pp.105-119.
99. Zhang, X., Wang, L. and Levänen, E., 2013. Superhydrophobic surfaces for the reduction of bacterial adhesion. *Rsc Advances*, 3(30), pp.12003-12020.
100. Legeay, G., Poncin-Epaillard, F. and Arciola, C.R., 2006. New surfaces with hydrophilic/hydrophobic characteristics in relation to (no) bioadhesion. *The International journal of artificial organs*, 29(4), pp.453-461.
101. Pogodin, S., Hasan, J., Baulin, V.A., Webb, H.K., Truong, V.K., Nguyen, T.H.P., Boshkovikj, V., Fluke, C.J., Watson, G.S., Watson, J.A. and Crawford, R.J., 2013.

- Biophysical model of bacterial cell interactions with nanopatterned cicada wing surfaces. *Biophysical journal*, 104(4), pp.835-840.
102. Thwaites, J.J. and Surana, U.C., 1991. Mechanical properties of *Bacillus subtilis* cell walls: effects of removing residual culture medium. *Journal of bacteriology*, 173(1), pp.197-203.
103. Chu, S., Shahi, I., Huiszoon, R.C., Culver, J.N. and Ghodssi, R., 2019, June. Bionanoscaffolds-Enabled Non-Wetting Surfaces for Antibiofouling Applications. In 2019 20th International Conference on Solid-State Sensors, Actuators and Microsystems & Eurosensors XXXIII (TRANSDUCERS & EUROSENSORS XXXIII) (pp. 2384-2387). IEEE.
104. Pan, Q., Cao, Y., Xue, W., Zhu, D. and Liu, W., 2019. Picosecond laser-textured stainless steel superhydrophobic surface with an antibacterial adhesion property. *Langmuir*, 35(35), pp.11414-11421.
105. Fadeeva, E., Truong, V.K., Stiesch, M., Chichkov, B.N., Crawford, R.J., Wang, J. and Ivanova, E.P., 2011. Bacterial retention on superhydrophobic titanium surfaces fabricated by femtosecond laser ablation. *Langmuir*, 27(6), pp.3012-3019.
106. Feng, G., Cheng, Y., Wang, S.Y., Borca-Tasciuc, D.A., Worobo, R.W. and Moraru, C.I., 2015. Bacterial attachment and biofilm formation on surfaces are reduced by small-diameter nanoscale pores: how small is small enough?. *npj Biofilms and Microbiomes*, 1(1), pp.1-9.
107. Gopal, J., Tata, B.V.R., George, R.P., Muraleedharan, P. and Dayal, R.K., 2008. Biofouling control of titanium by microroughness reduction. *Surface engineering*, 24(6), pp.447-451.
108. Bagherifard, S., Hickey, D.J., de Luca, A.C., Malheiro, V.N., Markaki, A.E., Guagliano, M. and Webster, T.J., 2015. The influence of nanostructured features on bacterial adhesion and bone cell functions on severely shot peened 316L stainless steel. *Biomaterials*, 73, pp.185-197.
109. Kathiresan, S. and Mohan, B., 2017. In-vitro bacterial adhesion study on stainless steel 316L subjected to magneto rheological abrasive flow finishing.
110. Perera-Costa, D., Bruque, J.M., González-Martín, M.L., Gómez-García, A.C. and Vadillo-Rodríguez, V., 2014. Studying the influence of surface topography on bacterial adhesion using spatially organized microtopographic surface patterns. *Langmuir*, 30(16), pp.4633-4641.

111. Pechook, S., Sudakov, K., Polishchuk, I., Ostrov, I., Zakin, V., Pokroy, B. and Shemesh, M., 2015. Bioinspired passive anti-biofouling surfaces preventing biofilm formation. *Journal of Materials Chemistry B*, 3(7), pp.1371-1378.
112. Gupta, R.K., Anandkumar, B., Choubey, A., George, R.P., Ganesh, P., Upadhyaya, B.N., Philip, J., Bindra, K.S. and Kaul, R., 2019. Antibacterial and Corrosion Studies on Nanosecond Pulse Laser Textured 304 L Stainless Steel Surfaces. *Lasers in Manufacturing and Materials Processing*, 6(3), pp.332-343.
113. Shen, J., Ming, P., Zhang, X., Yan, L., Zheng, X. and Wang, W., 2019. Broad Spectrum Anti-Fouling, Photocatalytic Antibacterial and Superamphiphobic Coating Fabricated by Composite Electrodeposition Process. *Journal of The Electrochemical Society*, 166(16), p.E564.
114. Zhang, X., Liu, Z., Li, Y., Wang, C., Zhu, Y., Wang, H. and Wang, J., 2019. Robust superhydrophobic epoxy composite coating prepared by dual interfacial enhancement. *Chemical Engineering Journal*, 371, pp.276-285.
115. Manoj, T.P., Rasitha, T.P., Vanithakumari, S.C., Anandkumar, B., George, R.P. and Philip, J., 2020. A simple, rapid and single step method for fabricating superhydrophobic titanium surfaces with improved water bouncing and self cleaning properties. *Applied Surface Science*, 512, p.145636.
116. Vanithakumari, S.C., George, R.P. and Mudali, U.K., 2013. Enhancement of corrosion performance of titanium by micro-nano texturing. *Corrosion*, 69(8), pp.804-812.
117. Desbois, A.P. and Smith, V.J., 2010. Antibacterial free fatty acids: activities, mechanisms of action and biotechnological potential. *Applied microbiology and biotechnology*, 85(6), pp.1629-1642.
118. Jin, B., Liu, M., Zhang, Q., Zhan, X. and Chen, F., 2017. Silicone oil swelling slippery surfaces based on mussel-inspired magnetic nanoparticles with multiple self-healing mechanisms. *Langmuir*, 33(39), pp.10340-10350.
119. Wong, T.S., Kang, S.H., Tang, S.K., Smythe, E.J., Hatton, B.D., Grinthal, A. and Aizenberg, J., 2011. Bioinspired self-repairing slippery surfaces with pressure-stable omniphobicity. *Nature*, 477(7365), pp.443-447.
120. Vogel, N., Belisle, R.A., Hatton, B., Wong, T.S. and Aizenberg, J., 2013. Transparency and damage tolerance of patternable omniphobic lubricated surfaces based on inverse colloidal monolayers. *Nature communications*, 4(1), pp.1-10.

121. Kim, P., Wong, T.S., Alvarenga, J., Kreder, M.J., Adorno-Martinez, W.E. and Aizenberg, J., 2012. Liquid-infused nanostructured surfaces with extreme anti-ice and anti-frost performance. *ACS nano*, 6(8), pp.6569-6577.
122. Zhang, C., Xia, Y., Zhang, H. and Zacharia, N.S., 2018. Surface functionalization for a nontextured liquid-infused surface with enhanced lifetime. *ACS applied materials & interfaces*, 10(6), pp.5892-5901.
123. Howell, C., Vu, T.L., Lin, J.J., Kolle, S., Juthani, N., Watson, E., Weaver, J.C., Alvarenga, J. and Aizenberg, J., 2014. Self-replenishing vascularized fouling-release surfaces. *ACS applied materials & interfaces*, 6(15), pp.13299-13307.
124. Leslie, D.C., Waterhouse, A., Berthet, J.B., Valentin, T.M., Watters, A.L., Jain, A., Kim, P., Hatton, B.D., Nedder, A., Donovan, K. and Super, E.H., 2014. A bioinspired omniphobic surface coating on medical devices prevents thrombosis and biofouling. *Nature biotechnology*, 32(11), pp.1134-1140.
125. Tesler, A.B., Kim, P., Kolle, S., Howell, C., Ahanotu, O. and Aizenberg, J., 2015. Extremely durable biofouling-resistant metallic surfaces based on electrodeposited nanoporous tungstite films on steel. *Nature communications*, 6(1), pp.1-10.
126. Ouyang, Y., Zhao, J., Qiu, R., Hu, S., Chen, M. and Wang, P., 2019. Liquid-infused superhydrophobic dendritic silver matrix: A bio-inspired strategy to prohibit biofouling on titanium. *Surface and Coatings Technology*, 367, pp.148-155.
127. Deng, W., Long, M., Miao, X., Wen, N. and Deng, W., 2017. Eco-friendly preparation of robust superhydrophobic Cu (OH) 2 coating for self-cleaning, oil-water separation and oil sorption. *Surface and Coatings Technology*, 325, pp.14-21.
128. Sun, S., Tang, S., Chang, X., Wang, N., Wang, D., Liu, T., Lei, Y. and Zhu, Y., 2019. A bifunctional melamine sponge decorated with silver-reduced graphene oxide nanocomposite for oil-water separation and antibacterial applications. *Applied Surface Science*, 473, pp.1049-1061.
129. Zou, X., Zhang, L., Wang, Z. and Luo, Y., 2016. Mechanisms of the antimicrobial activities of graphene materials. *Journal of the american chemical society*, 138(7), pp.2064-2077.
130. Smith, S.C. and Rodrigues, D.F., 2015. Carbon-based nanomaterials for removal of chemical and biological contaminants from water: a review of mechanisms and applications. *Carbon*, 91, pp.122-143.

131. Zhao, L., Li, R., Xu, R., Si, D., Shang, Y., Ye, H., Zhang, Y., Ye, H. and Xin, Q., 2020. Antifouling slippery liquid-infused membrane for separation of water-in-oil emulsions. *Journal of Membrane Science*, p.118289.
132. [00] Chen, T.Y., Port, R.D., Batton, C.B. and Cicero, D.M., 1998, January. Condensate corrosion in steam generating systems. In *CORROSION 98*. NACE International.
133. shizaki, T., Hieda, J., Saito, N., Saito, N., and Takai, O., 2010. Corrosion resistance and chemical stability of super-hydrophobic film deposited on magnesium alloy AZ31 by microwave plasma-enhanced chemical vapor deposition. *Electrochimica Acta*, 55(23), pp.7094-7101.
134. Barkhudarov, P.M., Shah, P.B., Watkins, E.B., Doshi, D.A., Brinker, C.J., and Majewski, J., 2008. Corrosion inhibition using superhydrophobic films. *Corrosion Science*, 50(3), pp.897-902.
135. Hintze, P.E., and Calle, L.M., 2006. Electrochemical properties and corrosion protection of organosilane self-assembled monolayers on aluminum 2024-T3. *Electrochimica Acta*, 51(8-9), pp.1761-1766.
136. Skorb, E.V., Shchukin, D.G., Möhwald, H., and Andreeva, D.V., 2010. Ultrasound-driven design of metal surface nanofoams. *Nanoscale*, 2(5), pp.722-727.
137. Hu, F., Xu, P., Wang, H., byoung Kang, U., Hu, A. and Li, M., 2015. Superhydrophobic and anti-corrosion Cu microcones/Ni–W alloy coating fabricated by electrochemical approaches. *RSC advances*, 5(126), pp.103863-103868.
138. Zhang, Z., Ge, B., Men, X. and Li, Y., 2016. Mechanically durable, superhydrophobic coatings prepared by dual-layer method for anti-corrosion and self-cleaning A Physicochemical and engineering aspects.
139. Peng, R., Liang, L., Hood, Z.D., Boulesbaa, A., Puretzky, A., Ievlev, A.V., Come, J., Ovchinnikova, O.S., Wang, H., Ma, C. and Chi, M., 2016. In-plane heterojunctions enable multiphase two-dimensional (2D) MoS<sub>2</sub> nanosheets as efficient photocatalysts for hydrogen evolution from water reduction. *ACS Catalysis*, 6(10), pp.6723-6729.
140. Zhang, F., Chen, S., Dong, L., Lei, Y., Liu, T. and Yin, Y., 2011. Preparation of superhydrophobic films on titanium as effective corrosion barriers. *Applied surface science*, 257(7), pp.2587-2591.
141. Ning, T., Xu, W. and Lu, S., 2011. Fabrication of superhydrophobic surfaces on zinc substrates and their application as effective corrosion barriers. *Applied surface science*, 258(4), pp.1359-1365.

142. Hermelin, E., Petitjean, J., Lacroix, J.C., Chane-Ching, K.I., Tanguy, J. and Lacaze, P.C., 2008. Ultrafast electrosynthesis of high hydrophobic polypyrrole coatings on a zinc electrode: Applications to the protection against corrosion. *Chemistry of Materials*, 20(13), pp.4447-4456.
143. Song, T., Liu, Q., Zhang, M., Chen, R., Takahashi, K., Jing, X., Liu, L. and Wang, J., 2015. Multiple sheet-layered super slippery surfaces based on anodic aluminum oxide and its anticorrosion property. *RSC advances*, 5(86), pp.70080-70085.
144. Lee, J., Shin, S., Jiang, Y., Jeong, C., Stone, H.A. and Choi, C.H., 2017. Oil-Impregnated Nanoporous Oxide Layer for Corrosion Protection with Self-Healing. *Advanced Functional Materials*, 27(15), p.1606040.
145. Yao, W., Liang, W., Huang, G., Jiang, B., Atrens, A. and Pan, F., 2020. Superhydrophobic coatings for corrosion protection of magnesium alloys. *Journal of Materials Science & Technology*.
146. Darband, G.B., Aliofkhazraei, M., Khorsand, S., Sokhanvar, S. and Kaboli, A., 2020. Science and engineering of superhydrophobic surfaces: review of corrosion resistance, chemical and mechanical stability. *Arabian Journal of Chemistry*, 13(1), pp.1763-1802.
147. Lomga, J., Varshney, P., Nanda, D., Satapathy, M., Mohapatra, S.S. and Kumar, A., 2017. Fabrication of durable and regenerable superhydrophobic coatings with excellent self-cleaning and anti-fogging properties for aluminum surfaces. *Journal of Alloys and Compounds*, 702, pp.161-170.
148. Varshney, P. and Mohapatra, S.S., 2018. Durable and regenerable superhydrophobic coatings for brass surfaces with excellent self-cleaning and anti-fogging properties prepared by immersion technique. *Tribology International*, 123, pp.17-25.
149. Howarter, J.A. and Youngblood, J.P., 2007. Self-cleaning and anti-fog surfaces via stimuli-responsive polymer brushes. *Advanced materials*, 19(22), pp.3838-3843.
150. Cao, M., Guo, D., Yu, C., Li, K., Liu, M. and Jiang, L., 2016. Water-repellent properties of superhydrophobic and lubricant-infused "slippery" surfaces: A brief study on the functions and applications. *ACS applied materials & interfaces*, 8(6), pp.3615-3623.
151. Park, K.C., Chhatre, S.S., Srinivasan, S., Cohen, R.E. and McKinley, G.H., 2013. Optimal design of permeable fiber network structures for fog harvesting. *Langmuir*, 29(43), pp.13269-13277.

152. Lalia, B.S., Anand, S., Varanasi, K.K. and Hashaikeh, R., 2013. Fog-harvesting potential of lubricant-impregnated electrospun nanomats. *Langmuir*, 29(42), pp.13081-13088.
153. Liu, X., Shen, H., Liu, J., Zhang, J., Chen, Y., Zhang, Z., Zhang, F., Guan, N., Zhao, D. and Jin, Z., 2020. A green, maskless, and universal preparation method for patterned surfaces on various metal substrates. *Applied Surface Science*, 514, p.145838.
154. Esmerlyan, K.D., 2020. From extremely water-repellent coatings to passive icing protection—principles, limitations and innovative application aspects. *Coatings*, 10(1), p.66.
155. Yancheshme, A.A., Momen, G. and Aminabadi, R.J., 2020. Mechanisms of ice formation and propagation on superhydrophobic surfaces: A review. *Advances in Colloid and Interface Science*, p.102155.
156. Wang, G. and Guo, Z., 2019. Liquid infused surfaces with anti-icing properties. *Nanoscale*, 11(47), pp.22615-22635.
157. Irajizad, P., Nazifi, S. and Ghasemi, H., 2019. Icephobic surfaces: Definition and figures of merit. *Advances in colloid and interface science*, 269, pp.203-218.
158. Latthe, S.S., Sutar, R.S., Bhosale, A.K., Nagappan, S., Ha, C.S., Sadasivuni, K.K., Liu, S. and Xing, R., 2019. Recent developments in air-trapped superhydrophobic and liquid-infused slippery surfaces for anti-icing application. *Progress in Organic Coatings*, 137, p.105373.
159. Jung, S., Tiwari, M.K., Doan, N.V. and Poulikakos, D., 2012. Mechanism of supercooled droplet freezing on surfaces. *Nature communications*, 3(1), pp.1-8.
160. Kulinich, S.A., Farhadi, S., Nose, K. and Du, X.W., 2011. Superhydrophobic surfaces: are they really ice-repellent?. *Langmuir*, 27(1), pp.25-29.
161. Kulinich, S.A. and Farzaneh, M., 2009. How wetting hysteresis influences ice adhesion strength on superhydrophobic surfaces. *Langmuir*, 25(16), pp.8854-8856.
162. Kulinich, S.A. and Farzaneh, M., 2009. Ice adhesion on super-hydrophobic surfaces. *Applied Surface Science*, 255(18), pp.8153-8157.
163. Tourkine, P., Le Merrer, M. and Quéré, D., 2009. Delayed freezing on water repellent materials. *Langmuir*, 25(13), pp.7214-7216.
164. Meuler, A.J., Smith, J.D., Varanasi, K.K., Mabry, J.M., McKinley, G.H. and Cohen, R.E., 2010. Relationships between water wettability and ice adhesion. *ACS applied materials & interfaces*, 2(11), pp.3100-3110.

## Chapter 3. Condensation on Nonwetting Surfaces

Condensation is an effective heat transfer method used in a variety of applications such as thermal management, electrical power generation, distillation, air conditioning, and natural gas processing. Enhancing condensation heat transfer could improve these systems' efficiencies considerably. For instance, the thermal efficiency of the steam cycle, which is one of the major power production processes, is directly linked to condensation heat transfer performance. Another prominent application of condensation which accounts for around 20% of the total energy consumption in developed countries is heating, ventilating, and air conditioning (HVAC) systems; improving condensation heat transfer in these systems could substantially improve air conditioning efficiency which would enable massive global energy savings.

On a typical surface, the vapor condenses as a film that acts as a substantial thermal barrier to subsequent condensation (filmwise condensation-FWC). Alternatively, vapor can condense as drops that roll off under gravity (dropwise condensation-DWC) and can provide up to a tenfold increase in heat transfer when compared to surfaces that condense filmwise [1-3]. Promoting condensation heat transfer by shifting FWC to DWC and delaying or preventing the flooding event is crucial to obtain the long-term high heat transfer performance. Condensation heat transfer performance also can be improved by increasing the condensate removal rate especially when the forming droplets are removed at smaller sizes [1,4-7]. Since a condensate droplet presents a thermal resistance as it forms, it is desirable to shed condensate drops as quickly as possible [8]. Studies on surface wettability have shown promising approaches for surface modification to enhance condensation heat transfer. It's been shown that a lower contact angle hysteresis (CAH) will result in the shedding of condensate drops at a smaller size, and thus a larger heat transfer coefficient. The dropwise condensation heat transfer coefficient also depends on several complex factors including nucleation site density and droplet population distribution [9]. Condensation thermal resistances, substrate thermal resistance, vapor pressure, and the presence of non-condensable gases (NCG) could affect these factors and their impact will be discussed in this review. Several superhydrophobic (SHS) and liquid-infused surfaces (LIS) have been manufactured and their performance during condensation of steam or water vapor, as well as low surface tension fluids have been

studied. This part of the thesis is focused to summarize the recent developments to highlight the achievements of this field.

### **3.1 Condensation over SHS**

Studies on surfaces with different wettability have shown that superhydrophobic surfaces, obtained by combining low surface free energy with micro/nano-scale surface roughness, can promote dropwise condensation mode. While superhydrophilic ones, obtained by roughening the substrate, showing the promotion of film formation during condensation. Effect of surface morphology on promoting DWC has been established via several studies; continuous dropwise condensation (DWC) on a two-tier silicon superhydrophobic surface was studied by Chen et al. [8] and they were able to maintain DWC for up to 1 hour during their experiment on a superhydrophobic surface with short carbon nanotubes(CNTs) deposited on micromachined posts over a silicon substrate before it turns in to FWC. In another study [10] they sustained DWC for 30 minutes on CNTs which were grown by plasma-enhanced chemical vapor deposition on silicon substrates. They investigated the effect of NCG presence on condensation and it was shown that the condensate droplet conducts a transition from the Wenzel to the Cassie mode when the NCG concentration increases, indicating NCG can promote dropwise condensation. In this scenario, the condensate could not be automatically removed from the textured condensing surface. Without mechanical actuation, condensate accumulates on the textured surface leading to surface flooding in a fast fashion. Due to the filmwise condensation, the condensation heat transfer coefficient of the prepared superhydrophobic surface was lower than that of a flat hydrophobic surface especially under high heat flux situations and saturation pressures. The observed effect for the presence of NCG on DWC over SHS is different from the consequence of its presence in FWC mode. In a common condenser with an FWC regime, the presence of noncondensable gas is typically unavoidable, and even with the presence of a very small amount, it is significantly detrimental to the overall heat transfer rates of the system [11]. As the NCG builds up near the condenser surface, it creates another layer of resistance for steam condensation, and consequently the heat transfer rate of the whole system. With the presence of NCG, the thermal resistance from mixture diffusion in the gas phase is at

least one order of magnitude larger than that of the condensate film layer [12]. On the other hand, it seems that the gas layer builds up over SHS, reinforces the trapped gas layer required for the proper function of the surface, and enhances DWC.

Later, Lee et al. [13] fabricated micro/nano-scale porous surfaces on the steam condenser tubes made of copper alloy 122 to promote dropwise condensation. The micro/nano-scale porous surfaces could effectively initiate dropwise condensation by generating smaller condensates and limiting the growth of large condensate drops and by improving the surface renewal rate. Although dropwise condensation modes were observed during the condensation tests, the prepared surfaces with polymer-based coatings and a self-assembled layer showed less heat flux than those from the film-wise condensation correlation, this was justified because of the extra thermal transfer resistances added by the coating layers on the condensation surfaces. Although the addition of a coating layer can promote dropwise condensation, it will also increase the thermal resistance of the condensation process. The effect of the promoter thermal resistance on the dropwise condensation heat transfer coefficient has been investigated to establish the proper coating thickness [14,15]. For thicker Polytetrafluoroethylene (PTFE) coatings the thermal resistance of the promoter could be modeled as a conduction thermal resistance, using the thermal conductivity of the promoter and its thickness to calculate a thermal resistance. This assumption is only accurate if the coating thickness is greater than the Kapitza length of the interface. However, for monolayer promoters, with a length scale of around 2 nm, the interacting phonon and fluid-particle interactions between the metal, promoter, and liquid play a role in the thermal interface resistance. For such a case, experimental measurements for steam condensation show that the promoter resistance is an order of magnitude smaller than the total droplet thermal resistance [16]. Liu et al. [17,18] also studied the effect of superhydrophobic coating's thickness on heat transfer via a thermodynamic model based on Gibbs free energy and availability for heterogeneous condensation nucleation. Their model shows that a thin hydrophobic coating layer with a high thermal conductivity could decrease the droplet nucleation radius and is favorable for promoting dropwise condensation. The model also established the effect of vapor pressure on droplet characteristics; it was shown that the droplet nucleation radius will be enlarged at higher vapor pressures with higher saturated

temperature and smaller latent heat. Also, at higher saturation pressures, both the condensation heat flux and droplet nucleation density increase.

Effect of vapor pressure on DWC heat transfer was also studied by Hu et al. [19] and they showed that as the steam pressure decreased, the time for the droplet's direct growth increased and the gas-liquid interface transfer resistance increased rapidly. They concluded that to improve the heat transfer at low pressure, the focus should be on the reduction of the density of large droplets in addition to the reduction of departure size. Wen et al. [20] completed a similar study on hydrophobic copper tubes to investigate the transient characteristics of initial droplet size distribution, steady droplet size distribution, and thermal resistance distribution at lower and ultra-lower steam pressure for dropwise condensation at the pressure range of atmospheric to 1.5 kPa. Droplet size distribution turned more scattered at low steam pressure, showing larger departure size, and denser large droplets, resulting in the reduction of the effective heat transfer area. By comparing the thermal resistance distribution at various pressures, they showed that large droplets induced a greater proportion of resistance at low pressure.

Recently, the role of substrate thermal conductivity and vapor pressure in DWC was experimentally examined by Hoeng et al. [21]. Hydrophobic gold-plated copper, aluminum, carbon steel, and stainless-steel condenser surfaces, prepared using self-assembled monolayer coatings, were tested over a range of surface subcooling and vapor pressure. Results showed that the condensation heat transfer coefficient depends on the substrate thermal conductivity (fivefold higher for copper compared to stainless steel) and the tendency of a hydrophobic surface to maintain a small liquid-film resistance is controlled by the droplet growth and coalescence rate. With decreasing substrate thermal conductivity, the departing droplet radius and the surface coverage increase. The interfacial resistance which depends on the vapor mean free path increases at low pressure. Their proposed temperature-slip model predicts the measured interfacial vapor resistance closely.

Many reported SHS for condensation enhancement showed a limited ability for maintaining the DWC for a long time. The majority of the studies either reported transition to FWC in less than a few hours or do not provide a clear time frame for their experiments. Paxon et al. [22] reported sustained dropwise condensation of steam on a

thin film of poly-(1 H,1 H,2 H,2 H – perfluorodecyl acrylate)- co -divinyl benzene p(PFDA- co -DVB) implanted in a metal substrate by initiated chemical vapor deposition (iCVD). They were able to sustain DWC on the proposed surface after prolonged exposure to steam at 100 °C for more than 48 hours. iCVD surfaces exhibit heat transfer coefficients that are more than 7 times greater than filmwise condensation on practical engineering heat transfer substrates, such as aluminum and copper. The film thickness was optimized to ensure that the conduction resistance of the polymer film contributes no more than 1% of the total resistance. The iCVD process is a solvent-free vapor-phase deposition method, which is substrate independent. Tuning the process parameters allows for conformal thicknesses in which grafting to the substrate provides enhanced durability. iCVD can be applied to tubular geometries which are dominant heat transfer surfaces in shell-and-tube heat exchangers used across industries. These coatings have demonstrated great stability in industrial conditions and exhibited reduced contact angle hysteresis of condensing water droplets when compared to other hydrophobic coatings, leading to improved condensation heat transfer performance. The iCVD coatings effectively increase the vapor-side heat transfer coefficient of the condenser and are stable under industrial environments, which can be applied in a scalable fashion.

Nanofabricated superhydrophobic surfaces have achieved minimal droplet adhesion with high mobility for droplets. Rate of droplet removal can be controlled by external forces such as gravity or vapor shear; these forces need to overcome the surface tension which fixes the droplets to the condensing surface [23,24]. By reducing droplet departure sizes to below that of the capillary length and enabling faster clearing of the surface for re-nucleation, condensation could be enhanced. In an attempt to achieve a properly structured surface with these characteristics, Miljkovic et al. [25] fabricated a silanized copper oxide surfaces which could achieve highly efficient jumping-droplet condensation heat transfer. The prepared SHS demonstrated a 25% higher overall heat flux and 30% higher condensation heat transfer coefficient compared to hydrophobic condensing surfaces at low supersaturations ( $<1.12$ ). In their study, they demonstrated a major difference in condensation over hydrophilic, hydrophobic, and superhydrophobic surfaces as the condensation mechanism on the first two were independent of the supersaturation  $S$ , where  $S = P_v/P_{sat}(T_w)$  is the ratio of the partial vapor pressure of the

ambient air and the saturation pressure of water vapor at the substrate temperature. In contrast, condensation on the nanostructured SHS showed significant dependence on the supersaturation.

The Discovery of jumping droplet condensation, triggered by naturally occurring coalescence events over nanostructured SHS, has offered a new avenue to further enhance condensation heat transfer [26]. On low-adhesion surfaces, including synthetic and natural superhydrophobic surfaces, coalescing droplets can spontaneously jump off which could be used in a range of applications, such as self-cleaning condensers, anti-icing coatings, and thermal diodes. The droplets can jump out-of-plane upon coalescence due to surface energy being converted to kinetic energy [25,26]. This can be achieved by increasing the time-averaged density of small droplets. However, droplet jumping cannot be sustained if the nucleation density is too high and the spacing between droplets is reduced. In such conditions, droplets could strongly adhere to the surface and lead to a flooding condensation mode [27].

Out-of-plane jumping events triggered by multi-droplet coalescence and a single fallen droplet are observed by Lv et al. [28]. They studied the departure of multi-droplet coalescence on a superhydrophobic coated silicon surface with nanoscale roughness. Experimental data show that the droplets' departure due to coalescence and the jumping modes is dominant for the removal of condensed droplets from the substrate. In multi-droplet coalescence jumping mode, it is easier to overcome the energy barrier and the critical size of the self-propelled droplets could be further decreased. They also developed a general theoretical model that accounts quantitatively for determining the jumping velocity and the critical size of the multi-droplet coalescence. In another publication, Lv et al. [29] investigated droplet removal mechanism on Silicon wafer substrates with square-shaped micropillars fabricated by photolithography and etching of inductively coupled plasma (ICP). Based on this study they concluded that a further decreased value of Laplace pressure on the top side of the individual droplet leads to instability and subsequently an unexpected spontaneous dewetting transition without any external force. They reveal that the spacing of the micropillars is essential for determining the critical size of the droplet for the transition. Also, the nucleation density of the condensate must be smaller than the density of the surface features to prevent

flooding. Droplet jumping was also observed by Oh et al. [30]. They fabricated spray-coated mechanically robust superhydrophobic surfaces using treated titanium dioxide or silica particles. The spray-coating method was applied to the tube type condenser and the condensation behaviors were observed within the environmental chamber with controlled pressure, humidity, and non-condensable gas. The observed droplet jumping effect soon stopped and only dropwise condensation was observed since the condensed droplets were pinned on the cracks at spray-coated surfaces.

Wasserfall et al. [31] analyzed droplet jumping upon unequal-sized droplet coalescence by direct numerical simulations, exploring the effects of viscosity, droplet size ratios, and contact angle. The influence of viscous damping and gravity is given by a dimensionless number, Ohnesorge number, defined as  $Oh = \frac{\mu}{\sqrt{R_1 \rho_1 \sigma}}$ , where  $\mu$  is the dynamic viscosity of the droplet,  $R_1$  is radii of a spherical,  $\sigma$  is the surface tension and  $\rho_1$  is the density of the liquid droplets. For small Ohnesorge numbers, coalescence is dominated by capillary forces, inducing high jumping velocities. For large Ohnesorge numbers, coalescence is damped by viscous forces, restricting the jumping phenomenon to droplet coalescence with an Ohnesorge number of  $Oh < 0.5$ . Droplet size mismatch, expressed in terms of droplet size ratios, has a significant effect on the jumping velocity. Decreasing the droplet size ratio increases the ratio between adhesion forces of the merged droplet to the excess energy released due to droplet merging. Coalescence-induced droplet jumping was observed for droplet size ratios of more than 0.3 as the flow asymmetry caused by droplet mismatch limits the jumping phenomenon. This limiting condition for nearly nonwetting properties is reduced for wetting properties with stronger adhesive forces, i.e., smaller contact angles.

Mulroe et al. [32] also studied the effects of droplet size on jumping droplet condensation through experimental and modeling analysis which revealed that the critical diameter where condensing droplets can jump off an SHS upon coalescence is highly dependent upon the topology of the surface's nanostructure. They were able to show that critical jumping diameter could be reduced by an order of magnitude by designing slender and densely packed nanostructures. Because of its smaller condensate departure size, jumping-droplet condensation on SHS provides better heat transfer performance than does regular dropwise condensation.

The effects of surface orientation on jumping-droplet condensation had not received much attention as the out-of-plane jumping of coalescing droplets on SHS is capillary-inertial and is gravity independent. However, long-term condensation experiments on different surface orientations carried out by Mukherjee et al. [33] showed that jumping-droplet condensation is dramatically enhanced when gravitational shedding complements the jumping. By measuring the droplet size distribution at different orientations, it was revealed that the maximum droplet size was an order of magnitude smaller for the inclined surfaces compared to the horizontal orientation, which would enhance the theoretical heat transfer coefficient by 40% for the 45° tilt and by 100% for the vertical orientation.

To further enhance jumping droplet condensation, Traipattanakul et al. [34] examined electric field utilization as a method to increase the driving force acting on coalescing-jumping droplets and to extend the jumping height of the coalescing-jumping droplets. Through experiments and mathematical modelings, the jumping height of jumping droplets was determined as a function of the droplet radius, the average charge per surface area of a droplet, and the jumping angle. They demonstrate that with the electrostatic-induced jumping phenomenon, the maximum jumping height of coalescing jumping droplets is over three times higher than that of the classical coalescing-jumping droplets without an applied electric field. This could be explained as increases in the electric field causes the inertia force decreases, but the electrostatic force significantly increases. Effect of electric fields applied by pulsed and direct current (DC) power on droplet jumping dynamics behavior was studied by Tian et al. [35] as well. The results indicate that the droplet can jump more rapidly under the pulsed electric field which has instructively significance for some industrial fields such as surface self-cleaning, condensation, and digital microfluidics.

### **3.2 Condensation over Biophilic Surfaces**

Hybrid patterned surfaces also have shown promising aspects for droplet size control and droplet departure enhancement. Peng et al. [36] carried out steam condensation at atmospheric pressure on various hydrophobic– hydrophilic hybrid surfaces. surfaces with different hydrophobic and hydrophilic region widths were prepared on copper

substrate by locally masking, sandblasting, and self-assembling successively. The experimental results demonstrate that increasing hydrophobic region width leads to enlargement of the maximum droplet radius on the hydrophobic region while the droplet population density decreases. For an appropriately designed hybrid surface with an optimum hydrophobic region width condensation heat transfer could exceed DWC. (The steam condensation heat transfer on the optimum hybrid surface outperformed complete dropwise condensation by 23% at surface subcooling of 2.0 K.) Besides, the steam condensation heat transfer performance diminished with the increase of hydrophilic region width. The optimum maximum droplet radius was about 0.25 mm for the hydrophobic region width of about 0.55 mm. Also, surface subcooling has a counter effect on the heat transfer enhancement factor so steam condensation heat transfer can be boosted with a hydrophobic–hydrophilic hybrid surface more effectively at low surface subcooling.

Hu et al. [37] studied condensation heat transfer outside horizontal plain and finned copper tubes with different surface wettability. The hydrophobic surfaces or superhydrophobic surfaces with nanostructures were fabricated through methods of self-assembled monolayer coatings of n-octadecyl mercaptan with oxidation and etching treatments. The experimental results indicate that the hydrophilic– superhydrophobic hybrid finned tube achieves the highest condensation heat transfer performance in the presence of a large amount of NCG while it does not perform well for the pure vapor condensation. The dropwise condensation transforms gradually to the film condensation on both the superhydrophobic and the hydrophilic– superhydrophobic hybrid finned tubes with the increase of water vapor fraction.

Alwazzan et al. [38,39] prepared copper condenser tubes with alternative mini-scale straight patterns consisted of hydrophobic and less-hydrophobic regions. They showed that the wettability gradient created by the existence of the two adjacent regions can mitigate condensate and increase its removal rates. Hydrophobic regions served mainly as droplet nucleation sites with rapid droplet mobility; whereas the less-hydrophobic regions promoted droplet removal from the neighboring hydrophobic regions and served as drainage paths where condensate can be drained quickly by gravity. The results reveal that adjusting the patterned regions could affect the condensation heat transfer coefficient

which exceeds filmwise condensation heat transfer and in some ratios could significantly outperform a surface with a complete dropwise condensation. However, they also observed the presence of undesirable droplet bridging on all tested hybrid patterned surfaces, which could have a detrimental influence on the condensation heat transfer performance. A bridging droplet can be referred to a droplet joined (bridged) by two, three, or four neighboring less-hydrophobic stripes. As these unwanted droplets are formed on the surface more frequently, it'll induce additional thermal resistance which can reduce the condensation rate.

Several numerical studies on hybrid surfaces have been carried out using the lattice Boltzmann method. Li et al. [40] simulated transition from dropwise to filmwise condensation for a dry saturated vapor on downward-facing smooth subcooled horizontal hydrophobic walls with hydrophilic spots. Effects of wall subcooling and wettability of the surface on droplet departure diameter, average cycle time, and nucleation time were investigated. At lower wall subcooling, droplets are formed on hydrophilic spots of the hydrophobic surface. Coalescence of droplets and their subsequent departure were observed as subcooling increased. An additional rise in the wall subcooling leads to a transition from dropwise condensation to filmwise condensation mode, and droplets fall from the subcooled surface at locations according to Taylor's unstable wavelength.

To investigate condensation on a surface with gradient wettability, Deng et al. [41] developed a model of vapor condensation on a solid surface using the free energy lattice Boltzmann method. Firstly, the vapor condenses into a thin film due to the unbalanced wetting force, and then the film fractures into droplet nucleation as the condensation process goes on. The larger wettability gradient results in a larger amplitude oscillation of condensation rate and a slighter variation of surface coverage. The condensate droplets resulting from phase change on a gradient surface could be swept promptly to provide a favorable condition for the subsequent condensation phase change. When two adjacent droplets coalesce on a gradient surface, the droplet on the side of low surface energy accelerates and move faster which contributes to the movement of condensate droplets towards the hydrophilic side.

Li et al. also [42] numerically simulated dropwise condensation on rough structures with different wettability to study the effect of rough surfaces' wettability on heat transfer efficiency. They show that with the increase of strength coefficient of the fluid-solid interaction or surface hydrophobicity, the nucleation position rises from the bottom to top of the pillar, and the wetting state of droplet changes from the wetting Wenzel state to the nonwetting Cassie one. At higher surface hydrophobicity, the average condensation rate is smaller and the nucleation waiting time is higher.

Guo et al. [43] also investigated condensation characteristics on biomimetic subcooled surfaces with different pillar structures and mixed wettability on a novel 3D multicomponent/multiphase lattice Boltzmann method. They demonstrated that surface with larger wettability contrast is better at promoting stable dropwise condensation and controlling droplet nucleation density by geometry optimization. During dropwise condensation in presence of non-condensable gas, NCG accumulates at the corner of pillars and above the condensing liquid-vapor interface. It was shown that increasing pillar width or pillar height (with other geometric parameters remained unchanged), as well as decreasing degree of wall subcooling or NCG concentration, can delay the transition from dropwise to filmwise condensation. The observed effect of NCG on these hybrid surfaces was different from a homogeneous SHS studied by Chen et al. [8] as discussed earlier.

Chen et al. [44] also studied the surface size effect on enhancing the heat transfer coefficient of the DWC on biophilic surfaces through numerical simulation. In biophilic surfaces, when the hydrophobic domain is small, the maximum droplet diameter is controlled by the shortest dimension where the droplets merge at the boundary. This size-effect heat transfer coefficient enhancement is calculated through direct numerical simulations. Then the 1-D biophilic surface was optimized considering the size-dependent hydrophilic domain partial flooding, the subcooling (heat flux), and condenser length effects. Patterned wettability which can be accomplished using both chemical and topographical-based approaches has been investigated in several studies. Edalatpour et al. [45] provide comprehensive lists for surface wettability modification techniques and studies on patterned wettability surfaces in their recent review paper.

### 3.3 Surface Morphology Effect on Condensation

To accomplish successful dropwise condensation, both efficient droplet nucleation and droplet self-removal are essential. A variety of surface morphologies have been studied to attain these requirements. Heterogeneous wettability and hierarchical roughness features in multiscale structures were implemented by Chen et al. [46] to enhance both, drop nucleation and drop departure on a condensation surface. SHS with nanograsped micro pyramid arrays were fabricated using a combined anisotropic wet-etching and deep reactive ion etching (DRIE) process. In over a 1-hour experiment, the condensed drops remained spherical and continuously departed from the surface via coalescence with neighboring drops. Fast drop growth and drop departure can naturally lead to a larger surface coverage of small drops. While Small drops contribute to most of the heat transfer in dropwise condensation because of their small thermal resistances. They reported a global superhydrophobicity as well as locally wettable nucleation sites which resulted in around a 65% increase in the drop number density and almost 450% increase in the drop self-removal volume as compared to an SHS with nanostructures alone. While this study was focused on silicon, the concept of activating the three-phase interfaces by tailoring micro/nanostructures for enhanced dropwise condensation can also apply to other material systems.

Park et al. [47] investigated water vapor condensation on an SHS with convex millimetric bumps. The surface was prepared on a thin aluminum sheet pressed between three-dimensionally printed polymer and subsequently spin-coated with mineral oil. The study showed that by optimizing the radius of curvature and cross-sectional shape for the bumps, the vapor diffusion flux at the apex could be maximized. Analogous to cactus spines, this design integrates the apex geometry with a widening slope which could directly couple droplet growth facilitation with fast directional transport, by creating a free-energy profile that drives the droplet down the slope before its growth rate can decrease. To complement these effects, a slippery, pitcher-plant-inspired nanocoating was added to promote coalescence-driven growth and capillary-driven motion on the way down. Integrating all of these mechanisms, bumps could be designed to grow and transport large droplets even against gravity and overcome the effect of an unfavorable temperature gradient. The prepared surface achieved six fold-higher exponents of droplet

growth rate, faster nucleation, higher steady-state turnover rate, and a greater volume of water collected compared to other surfaces.

Yao et al. [48] studied the effects of macroscopic surface topography on the DWC of water on SHS. They transferred bump and dimple patterns from a pair of 3D printed molds by pressing a thin aluminum sheet between the two 3D printed molds. Results clearly show that, in the millimeter-scale size range, the droplets grow slower on a dimple than on a bump. For the same type of surface topography, the condensation enhancement or suppression could be more pronounced with a smaller magnitude of the radius of curvature. The diffusion flux of water vapor around the surface textures was numerically calculated and showed that diffusion flux magnitude is higher on bumps and lower on dimples compared to a flat surface. They also observed an unexpectedly less favorable condensation on smaller, millimeter-scale dimples where the capillary condensation effect is negligible.

Zhao et al. [49] investigated geometric effects on dropwise condensation, for pure vapor and an air-vapor mixture on the titanium block functionalized by depositing a fluorinated silane. It was demonstrated that convex structures enable faster droplet growth in an air-vapor mixture (in the presence of NCG); on the other hand, the same structures impose the opposite effect during pure vapor condensation. Their modeling and experimental results demonstrate that the same convex geometric feature, or bump, can impose opposite effects on dropwise condensation in different vapor conditions.

Qi et al. [50] fabricated sine-shaped micro-grooved surfaces employing dry etching technique on aluminum surfaces. The wetting behavior and heat transfer characteristics on the micro-grooved surfaces presented anisotropic characteristics, the static contact angle and contact angle hysteresis in the perpendicular direction was significantly larger than that in the parallel direction. For the vertically grooved surface, the heat transfer during dropwise condensation was increased to 30–50% due to improvement in the sweeping effects of falling droplets which was improved by the vertical grooves. It was shown that better heat transfer performance can be achieved when the ratio of height to pitch increases. The velocities of sliding down on horizontal grooved surfaces were only 60–70% of that on the smooth surface, while the velocities of sliding down on vertical grooved surfaces could improve to 120% or higher than that on the smooth surface.

For the rapid removal of condensed droplets and condensation heat transfer enhancement, Peng et al. [51] created a micro-grooved surface with CuO nanostructures by a combination of simple machining and self-limiting chemical oxidation method. When the condensed droplet exceeds the width of microgrooves due to growth and coalescence, the droplets would suspend on the microgrooves rather than permeated into microgrooves which leads to exposing the bottom of microgrooves for new nucleation. Also, suspended droplets had less basal area contacting with the surface, which resulted in reducing droplet departure size for accelerating the renewal of surface. The heat transfer tests demonstrated a significant dropwise condensation heat transfer enhancement on the micro-grooved surface with CuO nanostructures compared to that on a plain hydrophobic surface. Furthermore, the fabrication process of such surface combining machining and chemical oxidation method has provided a low cost and scalable avenue to large-scale industrial applications. Although, this study doesn't provide any data on preserving DWC for a long time.

SHS coatings are susceptible to mechanical damage and the fabrication of stable surfaces is another challenge to be addressed. Tam et al. [52] reported the fabrication of SHS surface on a copper substrate via electrodeposition of Ni-CeO<sub>2</sub> which could withstand abrasion test and show a promising application in high wear stability demands such as power plants and desalination condenser tubes.

Parin et al. [53] studied the effect of the fabrication chemical process on DWC performance. Condensation of pure steam has been investigated on four different SHS aluminum samples obtained via wet-chemical fabrication processes. To fabricate nanoscale roughness, the metal substrates were etched using three different strategies; then a fluorosilane film was deposited over them by two different modes of spin coating and immersion, to decrease the surface energy. This study demonstrates that the surface morphology has a role in the droplet behavior and the wettability could be changed with temperature. Comparing the samples demonstrated that on a rougher surface, the highest amount of nucleation sites is expected which leads to a more enhanced heat transfer coefficient (HTC). Furthermore, the roughness could influence the homogenous distribution of the hydrophobic layer (fluorooctatrchlorosilane-FOTS) over the surface. One of the samples with the highest roughness could remain superhydrophobic up to 90

°C; The highest values of HTC were obtained on this sample. In this case, an HTC value higher than  $100 \text{ kWm}^{-2} \text{ K}^{-1}$  at 3.5 K wall subcooling was measured, which is about 8 times higher than that during FWC on the untreated aluminum sample. The FOTS layer on this sample was either thinner or less homogenous as compared to the other samples and after 1 h of testing it was completely degraded. It was shown that the first step to achieve DWC is providing a good distribution of the hydrophobic layer. If the FOTS layer is not homogenous, the less protected aluminum can react more easily with vapor/water at high temperatures forming the flower-like structure of aluminum hydroxide. Another sample was able to maintain a good hydrophobicity even after 2 h of condensation due to the presence of FOTS. However, the presence of aluminum hydroxide flowerlike crystals could provide new nucleation sites for vapor condensation inside the roughness asperities, leading to the transition from DWC to FWC. If the nucleation site density is too high, superhydrophobic surfaces can become flooded. the coating used to control the wettability of the metallic surface should be chosen not only considering its surface energy but also given its capability to prevent corrosion phenomena of the substrate (especially if the substrate is aluminum).

### **3.4 Low Surface Tension Fluids Condensation over SHS**

Maintaining DWC for low surface tension fluids poses extra challenges and promises. Most prepared SHS for steam condensation will flood if used for low surface tension fluids condensation. On the other hand, developing proper SHS which could maintain DWC for low surface tension fluids has great potential in HVAC systems and other industrial organic Rankine cycles (ORCs) for hydrocarbons and refrigerants. Recently, Khalil et al. [54] designed grafted polymer coatings using initiated chemical vapor deposition (iCVD), that is capable of stable dropwise condensation of organic fluids (low-surface tension fluids). They have deposited poly-(1H,1H,2H,2H-perfluorodecyl acrylate)-co-divinyl benzene p(PFDA-co-DVB) thin films to typical heat exchanger metal substrates such as steel and titanium by iCVD. Condensation on the prepared samples showed a 4 to 8-fold enhancement in vapor-side heat transfer coefficients. To establish the performance of iCVD grafted surfaces, they compared the heat transfer

coefficient obtained for samples with different substrates for condensation of ethanol, hexane, and pentane. Heat transfer enhancement is also compared with the achievements of fins application and using electrohydrodynamics and mechanical vibration to shed the filmwise condensate.

Promoting dropwise condensation for low-surface tension fluids in heat exchangers used in HVAC and refrigeration, and petroleum processes have a great potential for enhancement of the system's efficiency. Another state-of-the-art employment for adjusting surface wettability is the design of CO<sub>2</sub>-phobic surfaces for dropwise condensation-based CO<sub>2</sub> capture applications. Through large-scale classic MD simulations, Wu et al. [55] revealed the role of nanoscale surface and topographical features on the wetting characteristic of a CO<sub>2</sub> droplet on Cu-like surfaces. They observed a critical transition of CO<sub>2</sub>-philic to CO<sub>2</sub>-phobic by pillared nanostructuring of the surface. A wetting state transition from the Cassie state to the Wenzel state appears by either changing the interaction energy parameter ( $\epsilon_{\text{Cu-CO}_2}$ ) or the structural parameter of the pillared surfaces. It can be inferred that the wetting state on a solid substrate can be tuned by surface roughening.

On the last note, it should be declared that besides all efforts to achieve DWC on hydrophobic surfaces, film condensation, is still the most common condensation mode in industrial condensers and thus it is important to understand how hydrophobicity may affect heat transfer during filmwise condensation. Hydrophobic and rough surfaces could promote dropwise condensation at low heat flux while at higher heat flux smooth condensing surfaces with low contact angle hysteresis have a better performance, avoiding the flooding mechanism which would occur on a superhydrophobic surface [25]. Enright et al. [56, 57] identified a limiting heat flux value of 80 kW/m<sup>2</sup> in the case of superhydrophobic surfaces. Col et al. [58] investigated the influence of the wetting properties during condensation of pure steam on a vertical surface. Aluminum substrates were modified to obtain a hydrophobic surface and condensation tests, at varying high heat fluxes (range of 250 and 500 kW/m<sup>2</sup>) and variation of vapor velocities have been performed on multiple hydrophilic and hydrophobic samples. The condensation mode was purely filmwise for all cases, even on the hydrophobic surfaces, due to the complete flooding of the surface. However, the filmwise condensation on the hydrophobic surfaces

exhibits higher heat transfer coefficients compared to the untreated hydrophilic plate. The heat transfer coefficient was higher by 10–45% on the hydrophobic surface as compared to the hydrophilic sample. This enhancement in heat transfer cannot be explained with classic filmwise condensation theory. To explain this effect, it was proposed that the non-zero slip length at the solid-liquid interface means a non-zero slip velocity which leads to a reduced condensate film thickness and enhanced condensation mass flow rate. The reduced thermal resistance of the condensate layer caused by the reduction of the liquid film thickness leads to an enhancement of the two-phase heat transfer coefficient. On the hydrophobic samples, contact angle measurements have been done which showed a change in the surface wettability after a certain period. This degradation of the fluorosilane layer for hydrophobic samples, caused the heat transfer coefficients to diminish to the values of the hydrophilic surface. Effect of vapor velocity and heat flux on heat transfer enhancement of hydrophobic surfaces was investigated and it was shown that for the same temperature difference between saturation and wall, the most heat transfer enhancement in comparison with hydrophilic surfaces obtained at higher steam velocities. Studies in the literature [59] suggest that slip velocity is proportional to the fluid velocity which means that by increasing the liquid-vapor interfacial velocity a higher slip velocity and thus a lower liquid film thickness could be attained.

### **3.5 Condensation over SLIPS**

To promote DWC, an efficient condenser surface should have critical surface energy appreciably lower than that of the condensate to result in a finite contact angle (wetting angle), and a contact angle hysteresis low enough to allow condensate drops to shed before they merge into a continuous film [60,61]. Slippery lubricant-impregnated porous surfaces (SLIPS) or lubricant-impregnated surfaces (LIS) have been fabricated by adding a selective lubricant to the structured surfaces similar to SHS to achieve this goal. The substrate should be porous, rough, or swellable to stabilize the lubricant layer by combining van der Waals forces and, if it is porous or rough, by capillary forces.

In SLIPS, the lubricant contained in the surface reduces the surface energy and prevents droplets from condensing within the surface texture. Random droplet nucleation

within surface asperities can grow to large drops leading to FWC over SHS which diminishes their effectiveness. This common problem for SHS could be avoided by SLIPS. Also, the presence of lubricant facilitates the droplets' mobility. On a conventional superhydrophobic surface, the critical size for departing droplets is on the order of a few millimeters while for SLIPS drops as small as  $20\mu\text{m}$  were mobile (with speeds of around  $1\text{ mm s}^{-1}$ ) on the surface as observed by Anand et al. [62] Besides, it's been demonstrated that under identical conditions, the droplet nucleation for water condensation on SLIPS is faster than on SHS, suggesting that the lubricant-impregnated surfaces have a lower energy barrier for nucleation.[62,63] A comprehensive comparison between SHS and SLIPS characteristics is provided in a review by Chen et al.[64]

Whether the onset of steam condensation on LIS could happen on top of the lubricant layer or within the lubricant layer and move upwards towards the lubricant-vapor interface as the droplets grow, has been debated over by different studies. The analysis proposed by Eslami et al. [65] and Anand et al. [62] had proposed that the nucleation of steam into the water on LIS should occur at the lubricant–air interface. In another study, Anand et al. rationalized that as long as the vapor content within the lubricant is limited by absorption it cannot achieve supersaturation to allow for nucleation within the lubricant, which suggests that nucleation should occur only on top of the lubricant layer [66]. On the other hand, Xiao et al. had suggested that for supersaturation of  $S = 1.6$  ( $S = P_v/P_w$ ), nucleation could occur at the solid surface beneath the lubricant at locations where the thickness of the oil film is small. In these regions, the water vapor was able to diffuse through the thin oil layer and form nuclei immersed in the oil layer on the high-surface-energy sites.[63] Another study by Kajiya et al. [67] clarified that the solid surface wettability could affect where the nucleating drops could form. Through 3D imaging using a laser scanning confocal microscope, they observed that on lubricant-impregnated hydrophobic micropillars, water drops nucleate and grow on the lubricant surface. However, on lubricant-impregnated hydrophilic micropillars, drops nucleate on the lubricant and the micropillars top surface, with a preference for nucleation on the top surfaces of micropillars. On lubricant-impregnated hydrophilic micropillars, once the water drops contact the bottom substrate, they do not detach, and their mobility is permanently restricted leading to the displacement of the lubricant layer with water. For

hydrophobic pillars, however, once droplets grow enough that their lower side contacts the bottom substrate, the lubricant/water interface forms a defined contact angle with the substrate. With further growth, the drops could span several micropillars and detach again from the bottom substrate.

The enhanced shedding and nucleation of droplets indicate the potential of SLIPS for high condensation heat transfer. Xiao et al. compared the condensation heat transfer of SLIPS versus conventional hydrophobic and SHS for typical industrial condenser materials which showed that SLIPS could achieve 200% heat transfer enhancement [63]. in contrast to SHS which only exhibits FWC at high supersaturation, SLIPS could also maintain dropwise condensation of steam up to the highest supersaturation tested.

Weisensee et al. [68] investigated heat transfer and sweeping rates for water condensation on an aluminum-based lubricant-infused vertical plate. Their study showed that surfaces with the low-viscosity oils ( $\nu = 12$  cSt) degraded quickly via lubricant drainage, whereas those surfaces with higher viscosity ( $\nu > 140$  cSt) remained stable for more than 10 hours of operation. Based on this observation they recommend using oils with a viscosity of more than 100-200 cSt for water condensation on LIS. Also, they showed that the coating thickness has a major role in heat transfer enhancement and thicknesses in the range of 0.5-5  $\mu\text{m}$  can increase heat transfer rates up to 10-15 times compared to traditional filmwise condensation.

Moreover, the dependence of sweeping rates on the distribution of droplet sizes and average heat transfer rates were investigated using artificial sweeping experiments and numerical modeling. The maximum departing droplet size decreases rapidly with only a modest decrease in the sweeping period. However, the distribution of droplet sizes and heat transfer rates were nearly unaffected. This trend could be justified as only droplets smaller than 100  $\mu\text{m}$  contribute and influence the heat transfer process. This study demonstrated that the distribution of droplet sizes on LIS is independent of lubricant viscosity. However, Anand et al. demonstrated in their study that drops that condense and grow on a lubricant-impregnated surface with 1000 cSt silicone oil as the lubricant tend to grow in a narrow size distribution whereas those that condense on a lubricant-impregnated surface with 10 cSt oil tend to be more polydisperse.[66]

It was shown by Anand et al. [62] that depending on the lubricant's surface tension and interfacial tension with water, nucleation on a lubricant can have a significantly lower energy barrier compared to that on solids. Based on their analysis, they proposed a system for the selection of lubricants that may lead to enhanced nucleation [66]. Several studies have shown a loss of lubricant during the condensation process and investigated lubricant loss mechanisms. It's been shown that SLIPS function could be diminished over time due to the depletion of the lubricant layer by various factors, including miscibility, evaporation, shearing, the loss of the cloaking layer, or the wetting ridge, etc. The first important condition for a proper lubricant is that it should be immiscible and non-reactive with the working fluid (the condensate). Other properties of the lubricant affect the successful fabrication of SLIPS; To avoid the risk of lubricant displacement by condensate liquid, the selected lubricant's receding contact angle on the porous surface and the interfacial tension between the lubricant and condensate liquid has a higher effect than lubricant's density. This means the affinity between the lubricant-solid should be greater than that between the air-solid and the working droplets-solid to ensure that the lubricant can penetrate the structures in an air environment and that the substrate will be preferentially wet by the lubricant rather than by the working droplets. Also, as typical condensers operate at low pressures, to avoid lubricant loss, lubricants used for condensation applications must have a low vapor pressure. Depending on the spreading coefficient of the lubricant on the working fluid, lubricant cloaking could happen for immiscible fluids. The lubricant can spread and encapsulate a working fluid drop, forming a cloak surrounding the lubricant droplet. The spreading coefficient is defined as  $S_{ol} = \gamma_l - \gamma_o - \gamma_{ol}$  where  $\gamma_l$ ,  $\gamma_o$ , and  $\gamma_{ol}$  are the liquid-vapor surface tensions of the condensate and lubricant and the interfacial tension between the lubricant and condensate, respectively. As long as the spreading coefficient of the lubricant on the working fluid in the presence of air is positive ( $S_{ol} > 0$ ), the lubricant will cloak. Anand et al. demonstrated that on lubricants that form a cloak over the condensed water drops, the rate of condensed water drop growth on lubricant surfaces is significantly reduced as compared to non-cloaking lubricants. The capillary forces of the lubricant could submerge drops that are smaller than the solid texture features after their formation, this will lead to lubricant displacement with working fluid. Shedding of cloaked drops which

depletes lubricant also affects the longevity of lubricant-impregnated surfaces. Also, the cloaking layer not only inhibits condensate growth and slides off, which is disadvantageous for the condensation heat transfer effect, but it also contaminates the discharged condensate, which could be undesirable. [62,69]

Another phenomenon observed for condensation over SLIPS is the non-coalescence of droplets on a SLIPS. Boreyko et al. found that the non-coalescence is due to the lubricant wetting ridge [70]. When two or more water droplets collide on a lubricant infused substrate, they exhibit noncoalescence due to the formation of a thin lubricant film that gets squeezed between the droplets from the bottom up. The time for two water drops to merge on a LIS is greater by an order of magnitude than for two water drops in a bath of the same lubricant and increases with the lubricant viscosity [70]. For example, the time for two 5  $\mu\text{L}$  water drops to coalesce is 1 s when the lubricant is 10 cSt silicone oil but around 1 day when the lubricant is 500 cSt silicone oil. Furthermore, they showed that mixing phospholipids into the water drops creates lipid bilayers that prevent coalescence indefinitely. Barman et al. demonstrate that the coalescence process can be rapidly accelerated by applying a voltage between the two drops [71]. Kreder et al. [72] found that the most important reason for the depletion of lubricant is the growth of the wetting ridge pulled up by the droplets through the balance of interfacial forces between the droplets, lubricant, and air. Therefore, to minimize the loss of lubricant, lubricant-working liquid pairs without a cloaking layer should first be selected. For the lubricants, a suitable viscosity and thin lubricant layer should be chosen that not only provides excellent lubricity but also reduces evaporation and slows down the formation of the cloaking layer and wetting ridge. For the external liquids, larger volume droplets or continuous fluids can be applied to suppress lubricant depletion. Besides, the external droplets with high speed can also reduce the loss of the lubricant wetting ridge.

Guo et al. [73] developed a molecular-dynamics-based numerical model that simulates SLIPS for all possible stable states for a given working fluid, lubricant, and solid surface. The influences of the lubricant thickness, the solid wettability, and the interfacial tension on the droplet sliding velocity have been investigated and it was suggested that with a proper increase in the lubricant thickness, the sliding velocity of the droplet could be increased for the encapsulated state of nanostructures. The sliding speed

of the drop on SLIPS is significantly improved if an excess film is present, however with an additional increase in the lubricant thickness, the velocity decrease. They identified that the interfacial tension between working fluid and surface, & lubricant, and the surface roughness are two main factors influencing the droplet sliding velocity. When the interfacial tension is larger, droplets slide faster.

Haghani-Hassan-Abadi et al. [74] also explored the condensation mechanism due to phase change on pillar arrays of a liquid-impregnated surface using a phase-field lattice Boltzmann method. In their model, a system consists of three immiscible fluids, two of which undergo phase change has been evaluated. The results demonstrated that the droplets can easily slip on the lubricant which aids the coalescence in the SLIPS system to happen sooner than the SHS system. It seems that this model doesn't reflect the wetting ridge effect for droplet coalescence on SLIPS.

Heat transfer degradation on SLIPS after extended use has been reported due to the loss of infused liquid. It's known that SLIPS with rough surfaces are more stable than smooth surfaces as they can hold the lubricant in place by capillary force. As capillary forces are generated only when the size of the surface features is small enough [75] and the scale of both micro and nanotextures is often smaller than the capillary length (which is a comparison of capillary forces to gravitational forces) of the corresponding lubricating liquids, the lubricant will be maintained within the textures firmly. Typical SLIPS are also subjected to shear stresses when they are exposed to the flow of external working fluids that act against capillary force to destroy the stability of the lubricant layer. With the strengthening of shear force, the lubricant film may drain over time, eventually resulting in the shear driven failure of SLIPS [76] Shearing of the lubricant in condensers can happen due to droplet shedding as droplets slide over the SLIPS, leading to accumulation of lubricant on the bottom of the condenser and eventually cause the failure of the SLIPS [68,77,78]. As was shown by Weisensee et al.[68], high viscosity lubricants provide longer-lasting performance during the condensation of steam, the same effect has been established for low surface energy liquids [77,78]. Therefore, to prevent the failure of SLIPS due to shear, a lubricant with a higher viscosity should be selected. Rough structures can also provide capillary forces to hold the lubricant in place against the shear force, and the shear resistance on the same surface increases as the surface

roughness increases.[79] the greater the roughness, the smaller the lubricant thickness required to maintain a continuous lubricant layer after being subjected to shear, and the better the shear resistance of the surface.

To compare the effect of micro and nanostructured surfaces on condensation enhancement, Maeda et al.[80] fabricated four hierarchical micro/nano-structured SLIPSs varying in the size and density of the structures by etching, oxidation, and hydrophobization of the copper surfaces, then immersion in Krytox General Purpose Lubricant. They observed a 100% heat transfer enhancement on nano-structured SLIPSs when compared to hierarchical micro/nano-structure SLIPSs. Although the microstructure retains more lubricant but demonstrates less heat transfer performance, whilst the nanostructure with the least amount of lubricant provides better performance. The presence of micro-structures induced a greater population of smaller sized droplets allowing for a greater number of condensing droplets and 50 % enhancement through individual droplets. However, this effect was not enough to overcome the greater heat transfer predicted on solely nano-structured SLIPSs as the micro-structures and the lubricant present within the structures imposed a greater thermal resistance. Another approach to improve SLIPS stability is using a closed-cell structure where the oil pockets separated by the individual nanopores will facilitate the stabilization of the oil within the porous structure. the closed-cell structure is used to improve mechanical stability [81,82]. and also improves the mechanical damage resistance [79].

An alternative method besides capillary-force-based lubricant stabilization is implementing  $\pi$ -electronic interactions which reduce the importance of the surface structure for lubricant stabilization, as a stable coating can be obtained even on a flat surface. Tsuchiya et al. [83] designed a liquid-infused smooth surface named “SPLASH” (surface with  $\pi$  electron interaction liquid adsorption, smoothness, and hydrophobicity) to obtain stable, high heat-transfer performance. The SPLASH is fabricated on Cu substrate by infusing silicone oil on a smooth base layer with abundant  $\pi$ -electrons through  $\pi$ -interactions, instead of using capillary force, as observed in SLIPS. The phenyl-group modified smooth base layer, which includes abundant  $\pi$ - electrons, is prepared via sol-gel reaction. The SPLASH displayed a maximum condensation heat-transfer coefficient which was 175% higher than that of an uncoated substrate. Considering

droplet mobility and the thermodynamic energy barrier for nucleation, the SPLASH outperformed SHS and SLIPS, demonstrating higher heat-transfer performance and more stable dropwise condensation. The SPLASH was able to sustain dropwise condensation after 16 h. However, the silicone oil would not remain on the surface permanently, and the condensation heat transfer coefficient would decrease due to the depletion of silicone oil. The effects of liquid-infused surface roughness and liquid viscosity on condensation heat transfer were investigated and it was shown that a smooth base layer and low-viscosity infusing liquid further increase droplet mobility and improve heat-transfer performance. Moreover, in a long-run condensation process, the lubricant thickness decreases however the LIS with a smooth substrate could maintain its stable water sliding ability better than the LIS with a rougher surface so it displayed longer-term stable dropwise condensation and heat transfer performance.

In an effort to address the challenge of preventing the depletion of the infused liquid Seo et al. [84] proposed a brushed LIS (BLIS) that can allow the application of LIS under high condensation heat transfer. In BLIS, a brush replenishes the depleted oil via physical contact with the rotational tube, while oil is continuously supplied to the brush by capillarity. To fabricate the BLIS, CuO nanostructures surfaces were used, and to render the surface hydrophobic, the samples were coated with self-assembled monolayers (SAMs) then it was impregnated with the fluorinated oil of Krytox 1506. The BLIS obtained up to 61% heat transfer enhancement compared to hydrophobic surfaces as the brush sweeping helped with droplet removal which leads to enhanced heat transfer performance. By applying BLIS, the stable dropwise condensation mode was maintained for more than 48 hours under high supersaturation levels

Typical SLIPS adopt Perfluoropolyethers [69,76,47,85-91] and silicone oils [92-94] as the infused lubricant. SLIPS prepared by organic lubricants are susceptible to lubricant evaporation at high temperatures. To create a liquid-infused surface that could sustain its stability at high temperatures, Wang et al. [95] designed and fabricated the ionic liquids-infused slippery surfaces on Nickel sheet by impregnating hydrophobic ionic liquids into the nanocone-like arrays. The prepared surface exhibited superior high-temperature resistance, high-efficiency condensation, and hot water repellency as compared with the SHS. Ionic liquids (ILs) are room-temperature molten salts composed

entirely of cations and anions, which are regarded as a new type of solvent except for aqueous and organic solvents [96]. Hydrophobic ILs are immiscible with water and have excellent negligible vapor pressure, high conductivity, and thermal stability [97]. Two kinds of 1-alkyl-3-methylimidazolium hexafluorophosphate ionic liquids (ILs) with different chain lengths were infused into the porous surface constructed by nanocone arrays of (NiCo-NCA), aiming to produce slippery surfaces with stable non-wetting performance. The prepared surfaces could endure physical damage and could quickly restore liquid repellency after physical damage and maintain high stability even under external impact. To demonstrate the mechanical stability physical damages were made by scratching the surfaces with a knife. As the lubricant layer is liquid, it simply flows towards the damaged area by surface-energy-driven capillary action [98], and spontaneously refills the physical voids. The ILs-infused SHS showed excellent anti-wetting behavior for room temperature water, and hot water ( $\sim 95\text{ }^{\circ}\text{C}$ ). The water sliding speed on the ILs-infused SSs could be tuned by the viscosity of the ILs. The lower the viscosity of the infused IL induced the faster sliding speed of the water droplet. The nucleation process of condensing water droplets may be easier on the ILs infused surfaces than that on the SHS. Though the droplets easily move around the ILs-infused surfaces, the surface adhesion would be higher and droplet removal would be also difficult as compared to SHS due to the larger SA of the ILs-infused surfaces. After 5 min, the ILs-infused SSs seem to have larger droplets than the SHS, indicating a quicker transition to filmwise condensation.

Condensation of low surface tension liquids on SLIPS has been investigated in the literature. It's been shown that SLIPS are more effective than flat or micro and nanostructured coatings at enhancing low surface tension fluid condensation heat transfer, but failure by depletion of the lubricant remains a critical concern. Rykaczewski et al. [99] investigated condensation behavior of a variety of low surface tension liquids (with surface tensions in the range of 12 to 28 mN/m including perfluoro hexane, pentane, hexane, octane, isopropanol, ethanol, and toluene) on smooth oleophobic, re-entrant superomniphobic, and lubricant-impregnated surfaces. The smooth and textured silicon wafers were functionalized with fluorosilane coatings. Krytox perfluorinated oil was then used to impregnate the textured surfaces. This lubricant was selected primarily

because its surface tension (17 mN/m) is low enough to promote dropwise condensation of most condensed fluids while avoiding cloaking [62,85], and also because of its low vapor pressure, broad chemical inertness, and immiscibility with most of the condensed fluids. The results demonstrated that smooth oleophobic and lubricant-impregnated surfaces can promote dropwise condensation however, re-entrant omniphobic surfaces get flooded and degraded to filmwise condensation as the condensing liquid displaced the Krytox film. It was shown that to reduce droplet pinning on the surface, the lubricant layer should be sustained through the proper choice of lubricant and underlying surface texture. With the proposed engineered surfaces they were able to promote dropwise condensation of low-surface tension fluids and achieved up to eight-fold improvement in the heat transfer coefficient. Later on, Sett et al. [100] developed a lubricant selection guideline for stable LISs and SLIPSs to enhance condensation of low-surface-tension working fluids. The guideline is developed based on immiscibility and cloaking effect between the lubricant and working fluid/condensate.

Preston et al. [77] confirmed the effectiveness of SLIPS in promoting dropwise condensation for Water and toluene condensation over plain, SHS, and LIS copper tubes by providing experimental measurements of heat transfer performance. Hydrocarbon condensation on a SLIPS showed 450% heat transfer enhancement compared to an uncoated surface. They also demonstrated heat transfer improvement through the removal of noncondensable gases where less than 10% NCG was shown to eliminate the gain in performance obtained from the promotion of dropwise condensation. The lubricant failure mechanism was observed after 1 hr due to shedding droplets. The degradation began at the top of the condenser surface and slowly moved downwards. Since toluene is not cloaked by Krytox, the droplet shearing effect [101,102] is primarily responsible for the LIS failure in this case as evidenced by the accumulation of lubricant at the base of the condenser over time.

Sett et al. [78] demonstrated stable dropwise condensation of ethanol and hexane on SLIPSs which were made of CuO substrate impregnated with Krytox 1525. They obtained about 200% enhancement in the condensation heat transfer coefficient for both fluids compared to filmwise condensation on hydrophobic surfaces. They were able to maintain 7 h of steady dropwise condensation. This study showed that for working fluids

having surface tension higher than the infused lubricant in SLIPS, the heat transfer performance is independent of the lubricant viscosity. However, when the surface tension of the condensate fluid and the lubricant becomes comparable, lower viscosity SLIPs result in easier droplet shedding, leading to better heat transfer performance. It is important to note that lubricants having viscosities that are too low can be detrimental because the surfaces degrade quickly through lubricant drainage. Thus, for best heat transfer results they recommended using lubricants with viscosity  $\mu \approx 500 \text{ mPa}\cdot\text{s}$  for developing stable, robust, and durable LISs.

### 3.6 Nomenclature

*Oh* Ohnesorge number

*R* Radii of a spherical droplet

*S* Spreading coefficient

#### *Subscripts and Superscripts*

*L* Liquid

*O* Oil

*OL* Oil-liquid

#### *Greek Symbols*

$\gamma$  Surface tension

$\mu$  Dynamic viscosity

$\rho$  Density

$\sigma$  Surface tension

$\nu$  Viscosity

### 3.7 References

1. Rose, J.W., 2002. Dropwise condensation theory and experiment: a review. Proceedings of the Institution of Mechanical Engineers, Part A: Journal of Power and Energy, 216(2), pp.115-128.
2. Rohsenow, W.M., Hartnett, J.P. and Cho, Y.I., 1998. Handbook of heat transfer (Vol. 3). New York: McGraw-Hill.
3. Cho, H.J., Preston, D.J., Zhu, Y. and Wang, E.N., 2016. Nanoengineered materials for liquid–vapour phase-change heat transfer. Nature Reviews Materials, 2(2), pp.1-17.
4. Sikarwar, B.S., Khandekar, S., Agrawal, S., Kumar, S. and Muralidhar, K., 2012. Dropwise condensation studies on multiple scales. Heat Transfer Engineering, 33(4-5), pp.301-341.
5. Le Fevre, E.J. and Rose, J.W., 1966. A theory of heat transfer by dropwise condensation. In International Heat Transfer Conference Digital Library. Begel House Inc..
6. Tanasawa, I. and Westwater, J.W., 1974. What we don't know about the Mechanism of Dropwise Condensation. In International Heat Transfer Conference Digital Library. Begel House Inc.
7. Rose, J.W., 1988. Some aspects of condensation heat transfer theory. International communications in heat and mass transfer, 15(4), pp.449-473.
8. Chen, C.H., Cai, Q., Tsai, C., Chen, C.L., Xiong, G., Yu, Y. and Ren, Z., 2007. Dropwise condensation on superhydrophobic surfaces with two-tier roughness. Applied physics letters, 90(17), p.173108.
9. Dietz, C., Rykaczewski, K., Fedorov, A.G. and Joshi, Y., 2010. Visualization of droplet departure on a superhydrophobic surface and implications to heat transfer enhancement during dropwise condensation. Applied physics letters, 97(3), p.033104.
10. Cheng, J., Vandadi, A. and Chen, C.L., 2012. Condensation heat transfer on two-tier superhydrophobic surfaces. Applied Physics Letters, 101(13), p.131909.
11. Othmer, D.F., 1929. The condensation of steam. Industrial & Engineering Chemistry, 21(6), pp.576-583.
12. Sparrow, E.M. and Lin, S.H., 1964. Condensation heat transfer in the presence of a noncondensable gas.
13. Lee, S., Cheng, K., Palmre, V., Bhuiya, M.M.H., Kim, K.J., Zhang, B.J. and Yoon, H., 2013. Heat transfer measurement during dropwise condensation using micro/nano-scale porous surface. International Journal of Heat and Mass Transfer, 65, pp.619-626.

14. Rose, J.W., 1981. Dropwise condensation theory. *International Journal of Heat and Mass Transfer*, 24(2), pp.191-194.
15. Abu-Orabi, M., 1998. Modeling of heat transfer in dropwise condensation. *International journal of heat and mass transfer*, 41(1), pp.81-87.
16. Bonner III, R.W., 2013. Correlation for dropwise condensation heat transfer: Water, organic fluids, and inclination. *International Journal of Heat and Mass Transfer*, 61, pp.245-253.
17. Liu, X. and Cheng, P., 2015. Dropwise condensation theory revisited: Part I. Droplet nucleation radius. *International Journal of Heat and Mass Transfer*, 83, pp.833-841.
18. Liu, X. and Cheng, P., 2015. Dropwise condensation theory revisited Part II. Droplet nucleation density and condensation heat flux. *International Journal of Heat and Mass Transfer*, 83, pp.842-849.
19. Hu, H.W. and Tang, G.H., 2014. Theoretical investigation of stable dropwise condensation heat transfer on a horizontal tube. *Applied thermal engineering*, 62(2), pp.671-679.
20. Wen, R., Lan, Z., Peng, B., Xu, W. and Ma, X., 2015. Droplet dynamics and heat transfer for dropwise condensation at lower and ultra-lower pressure. *Applied Thermal Engineering*, 88, pp.265-273.
21. Hoenig, S.H., Modak, S., Chen, Z., Kaviani, M., Gilchrist, J.F. and Bonner III, R.W., 2020. Role of substrate thermal conductivity and vapor pressure in dropwise condensation. *Applied Thermal Engineering*, 178, p.115529.
22. Paxson, A.T., Yagüe, J.L., Gleason, K.K. and Varanasi, K.K., 2014. Stable dropwise condensation for enhancing heat transfer via the initiated chemical vapor deposition (iCVD) of grafted polymer films. *Advanced Materials*, 26(3), pp.418-423.
23. Joanny, J.F. and De Gennes, P.G., 1984. A model for contact angle hysteresis. *The journal of chemical physics*, 81(1), pp.552-562.
24. Quéré, D., 2005. Non-sticking drops. *Reports on Progress in Physics*, 68(11), p.2495.
25. Miljkovic, N., Enright, R., Nam, Y., Lopez, K., Dou, N., Sack, J. and Wang, E.N., 2013. Jumping-droplet-enhanced condensation on scalable superhydrophobic nanostructured surfaces. *Nano letters*, 13(1), pp.179-187.
26. Boreyko, J.B. and Chen, C.H., 2009. Self-propelled dropwise condensate on superhydrophobic surfaces. *Physical review letters*, 103(18), p.184501.
27. Miljkovic, N. and Wang, E.N., 2013. Condensation heat transfer on superhydrophobic surfaces. *MRS bulletin*, 38(5), pp.397-406.

28. Lv, C., Hao, P., Yao, Z. and Niu, F., 2015. Departure of condensation droplets on superhydrophobic surfaces. *Langmuir*, 31(8), pp.2414-2420.
29. Lv, C., Hao, P., Zhang, X. and He, F., 2015. Dewetting transitions of dropwise condensation on nanotexture-enhanced superhydrophobic surfaces. *Acs Nano*, 9(12), pp.12311-12319.
30. Oh, S., Seo, D., Lee, C. and Nam, Y., 2016. Superhydrophobic surfaces for condensation by using spray coating method. In *Proceedings of the Korean Vacuum Society Conference* (pp. 157-2). The Korean Vacuum Society.
31. Wasserfall, J., Figueiredo, P., Kneer, R., Rohlf, W. and Pischke, P., 2017. Coalescence-induced droplet jumping on superhydrophobic surfaces: Effects of droplet mismatch. *Physical Review Fluids*, 2(12), p.123601.
32. Mulroe, M.D., Srijanto, B.R., Ahmadi, S.F., Collier, C.P. and Boreyko, J.B., 2017. Tuning superhydrophobic nanostructures to enhance jumping-droplet condensation. *ACS nano*, 11(8), pp.8499-8510.
33. Mukherjee, R., Berrier, A.S., Murphy, K.R., Vieitez, J.R. and Boreyko, J.B., 2019. How surface orientation affects jumping-droplet condensation. *Joule*, 3(5), pp.1360-1376.
34. Traipattanakul, B., Tso, C.Y. and Chao, C.Y., 2019. Electrostatic-induced coalescing-jumping droplets on nanostructured superhydrophobic surfaces. *International Journal of Heat and Mass Transfer*, 128, pp.550-561.
35. Tian, Y., Wang, H., Deng, Q., Zhu, X., Chen, R., Ding, Y. and Liao, Q., 2020. Dynamic behaviors and charge characteristics of droplet in a vertical electric field before bouncing. *Experimental Thermal and Fluid Science*, 119, p.110213.
36. Peng, B., Ma, X., Lan, Z., Xu, W. and Wen, R., 2015. Experimental investigation on steam condensation heat transfer enhancement with vertically patterned hydrophobic-hydrophilic hybrid surfaces. *International Journal of Heat and Mass Transfer*, 83, pp.27-38.
37. Hu, H.W., Tang, G.H. and Niu, D., 2015. Experimental investigation of condensation heat transfer on hybrid wettability finned tube with large amount of noncondensable gas. *International Journal of Heat and Mass Transfer*, 85, pp.513-523.
38. Alwazzan, M., Egab, K., Peng, B., Khan, J. and Li, C., 2017. Condensation on hybrid-patterned copper tubes (I): Characterization of condensation heat transfer. *International Journal of Heat and Mass Transfer*, 112, pp.991-1004.

39. Alwazzan, M., Egab, K., Peng, B. and Khan, J., 2017. Condensation on hybrid-patterned copper tubes (II): Visualization study of droplet dynamics. *International Journal of Heat and Mass Transfer*, 112, pp.950-958.
40. Li, X. and Cheng, P., 2017. Lattice Boltzmann simulations for transition from dropwise to filmwise condensation on hydrophobic surfaces with hydrophilic spots. *International Journal of Heat and Mass Transfer*, 110, pp.710-722.
41. Deng, Z., Zhang, C., Shen, C., Cao, J. and Chen, Y., 2017. Self-propelled dropwise condensation on a gradient surface. *International Journal of Heat and Mass Transfer*, 114, pp.419-429.
42. Li, M., Huber, C., Tao, W. and Wei, J., 2019. Study on nucleation position and wetting state for dropwise condensation on rough structures with different wettability using multiphase lattice Boltzmann method. *International Journal of Heat and Mass Transfer*, 131, pp.96-100.
43. Guo, Q. and Cheng, P., 2019. 3D lattice Boltzmann investigation of nucleation sites and dropwise-to-filmwise transition in the presence of a non-condensable gas on a biomimetic surface. *International Journal of Heat and Mass Transfer*, 128, pp.185-198.
44. Chen, Z., Modak, S., Kaviany, M. and Bonner, R., 2020. DIRECT SIMULATIONS OF BIPHILIC-SURFACE CONDENSATION: OPTIMIZED SIZE EFFECTS. *Frontiers in Heat and Mass Transfer (FHMT)*, 14.
45. Edalatpour, M., Liu, L., Jacobi, A.M., Eid, K.F. and Sommers, A.D., 2018. Managing water on heat transfer surfaces: A critical review of techniques to modify surface wettability for applications with condensation or evaporation. *Applied Energy*, 222, pp.967-992.
46. Chen, X., Wu, J., Ma, R., Hua, M., Koratkar, N., Yao, S. and Wang, Z., 2011. Nanograssed micropyramidal architectures for continuous dropwise condensation. *Advanced functional materials*, 21(24), pp.4617-4623.
47. Park, K.C., Kim, P., Grinthal, A., He, N., Fox, D., Weaver, J.C. and Aizenberg, J., 2016. Condensation on slippery asymmetric bumps. *Nature*, 531(7592), pp.78-82.
48. Yao, Y., Aizenberg, J. and Park, K.C., 2018. Dropwise condensation on hydrophobic bumps and dimples. *Applied Physics Letters*, 112(15), p.151605.
49. Zhao, Y., Preston, D.J., Lu, Z., Zhang, L., Queeney, J. and Wang, E.N., 2018. Effects of millimetric geometric features on dropwise condensation under different vapor conditions. *International Journal of Heat and Mass Transfer*, 119, pp.931-938.

50. Qi, B., Zhou, J., Wei, J. and Li, X., 2018. Study on the wettability and condensation heat transfer of sine-shaped micro-grooved surfaces. *Experimental Thermal and Fluid Science*, 90, pp.28-36.
51. Peng, Q., Jia, L., Dang, C., An, Z., Zhang, Y. and Yin, L., 2019. Analysis of droplet dynamic behavior and condensation heat transfer characteristics on rectangular microgrooved surface with CuO nanostructures. *International Journal of Heat and Mass Transfer*, 130, pp.1096-1107.
52. Tam, J., Erb, U. and Azimi, G., 2018. Non-wetting nickel-cerium oxide composite coatings with remarkable wear stability. *MRS Advances*, 3(29), pp.1647-1651.
53. Parin, R., Martucci, A., Sturaro, M., Bortolin, S., Bersani, M., Carraro, F. and Del Col, D., 2018. Nano-structured aluminum surfaces for dropwise condensation. *Surface and Coatings Technology*, 348, pp.1-12.
54. Khalil, K., Soto, D., Farnham, T., Paxson, A., Katmis, A.U., Gleason, K. and Varanasi, K.K., 2019. Grafted Nanofilms Promote Dropwise Condensation of Low-Surface-Tension Fluids for High-Performance Heat Exchangers. *Joule*, 3(5), pp.1377-1388.
55. Wu, J., Snustad, I., Ervik, Å., Brunsvold, A., He, J. and Zhang, Z., 2020. CO<sub>2</sub> wetting on pillar-nanostructured substrates. *Nanotechnology*, 31(24), p.245403.
56. Enright, R., Miljkovic, N., Alvarado, J.L., Kim, K. and Rose, J.W., 2014. Dropwise condensation on micro-and nanostructured surfaces. *Nanoscale and Microscale Thermophysical Engineering*, 18(3), pp.223-250.
57. Enright, R., Miljkovic, N., Al-Obeidi, A., Thompson, C.V. and Wang, E.N., 2012. Condensation on superhydrophobic surfaces: the role of local energy barriers and structure length scale. *Langmuir*, 28(40), pp.14424-14432.
58. Del Col, D., Parin, R., Bisetto, A., Bortolin, S. and Martucci, A., 2017. Film condensation of steam flowing on a hydrophobic surface. *International Journal of Heat and Mass Transfer*, 107, pp.307-318.
59. Granick, S., Zhu, Y. and Lee, H., 2003. Slippery questions about complex fluids flowing past solids. *Nature materials*, 2(4), pp.221-227.
60. Wilmhurst, R., 1979. Heat transfer during dropwise condensation of steam, ethane 1, 2 diol, aniline and nitrobenzene (Doctoral dissertation, Queen Mary, University of London).
61. Zhao, H. and Beysens, D., 1995. From droplet growth to film growth on a heterogeneous surface: condensation associated with a wettability gradient. *Langmuir*, 11(2), pp.627-634.

62. Anand, S., Paxson, A.T., Dhiman, R., Smith, J.D. and Varanasi, K.K., 2012. Enhanced condensation on lubricant-impregnated nanotextured surfaces. *ACS nano*, 6(11), pp.10122-10129.
63. Xiao, R., Miljkovic, N., Enright, R. and Wang, E.N., 2013. Immersion condensation on oil-infused heterogeneous surfaces for enhanced heat transfer. *Scientific reports*, 3(1), pp.1-6.
64. Chen, X., Wen, G. and Guo, Z., 2020. What are the design principles, from the choice of lubricants and structures to the preparation method, for a stable slippery lubricant-infused porous surface?. *Materials Horizons*.
65. Eslami, F. and Elliott, J.A., 2011. Thermodynamic investigation of the barrier for heterogeneous nucleation on a fluid surface in comparison with a rigid surface. *The Journal of Physical Chemistry B*, 115(36), pp.10646-10653.
66. Anand, S., Rykaczewski, K., Subramanyam, S.B., Beysens, D. and Varanasi, K.K., 2015. How droplets nucleate and grow on liquids and liquid impregnated surfaces. *Soft matter*, 11(1), pp.69-80.
67. Kajiya, T., Schellenberger, F., Papadopoulos, P., Vollmer, D. and Butt, H.J., 2016. 3D imaging of water-drop condensation on hydrophobic and hydrophilic lubricant-impregnated surfaces. *Scientific reports*, 6, p.23687.
68. Weisensee, P.B., Wang, Y., Qian, H., Schultz, D., King, W.P. and Miljkovic, N., 2017. Condensate droplet size distribution on lubricant-infused surfaces. *International Journal of Heat and Mass Transfer*, 109, pp.187-199.
69. Wong, T.S., Kang, S.H., Tang, S.K., Smythe, E.J., Hatton, B.D., Grinthal, A. and Aizenberg, J., 2011. Bioinspired self-repairing slippery surfaces with pressure-stable omniphobicity. *Nature*, 477(7365), pp.443-447.
70. Boreyko, J.B., Polizos, G., Datskos, P.G., Sarles, S.A. and Collier, C.P., 2014. Air-stable droplet interface bilayers on oil-infused surfaces. *Proceedings of the National Academy of Sciences*, 111(21), pp.7588-7593.
71. Barman, J., Pant, R., Nagarajan, A.K. and Khare, K., 2017. Electrowetting on dielectrics on lubricating fluid-infused smooth/rough surfaces with negligible hysteresis. *Journal of adhesion science and Technology*, 31(2), pp.159-170.
72. Kreder, M.J., Daniel, D., Tetreault, A., Cao, Z., Lemaire, B., Timonen, J.V. and Aizenberg, J., 2018. Film dynamics and lubricant depletion by droplets moving on lubricated surfaces. *Physical Review X*, 8(3), p.031053.

73. Guo, L., Tang, G.H. and Kumar, S., 2019. Droplet morphology and mobility on lubricant-impregnated surfaces: a molecular dynamics study. *Langmuir*, 35(49), pp.16377-16387.
74. Haghani-Hassan-Abadi, R. and Rahimian, M.H., 2019. A lattice Boltzmann method for simulation of condensation on liquid-impregnated surfaces. *International Communications in Heat and Mass Transfer*, 103, pp.7-16.
75. De Gennes, P.G., Brochard-Wyart, F. and Quéré, D., 2013. *Capillarity and wetting phenomena: drops, bubbles, pearls, waves*. Springer Science & Business Media.
76. Kim, P., Kreder, M.J., Alvarenga, J. and Aizenberg, J., 2013. Hierarchical or not? Effect of the length scale and hierarchy of the surface roughness on omniphobicity of lubricant-infused substrates. *Nano letters*, 13(4), pp.1793-1799.
77. Preston, D.J., Lu, Z., Song, Y., Zhao, Y., Wilke, K.L., Antao, D.S., Louis, M. and Wang, E.N., 2018. Heat transfer enhancement during water and hydrocarbon condensation on lubricant infused surfaces. *Scientific reports*, 8(1), pp.1-9.
78. Sett, S., Sokalski, P., Boyina, K., Li, L., Rabbi, K.F., Auby, H., Foulkes, T., Mahvi, A., Barac, G., Bolton, L.W. and Miljkovic, N., 2019. Stable Dropwise Condensation of Ethanol and Hexane on Rationally Designed Ultrascaleable Nanostructured Lubricant-Infused Surfaces. *Nano letters*, 19(8), pp.5287-5296.
79. Vogel, N., Belisle, R.A., Hatton, B., Wong, T.S. and Aizenberg, J., 2013. Transparency and damage tolerance of patternable omniphobic lubricated surfaces based on inverse colloidal monolayers. *Nature communications*, 4(1), pp.1-10.
80. Maeda, Y., Lv, F., Zhang, P., Takata, Y. and Orejon, D., 2020. Condensate Droplet Size Distribution and Heat Transfer on Hierarchical Slippery Lubricant Infused Porous Surfaces. *Applied Thermal Engineering*, p.115386.
81. Williams, M.K., Weiser, E.S., Fesmire, J.E., Grimsley, B.W., Smith, T.M., Brenner, J.R. and Nelson, G.L., 2005. Effects of cell structure and density on the properties of high performance polyimide foams. *Polymers for advanced technologies*, 16(2-3), pp.167-174.
82. Aly, M.S., 2007. Behavior of closed cell aluminium foams upon compressive testing at elevated temperatures: Experimental results. *Materials Letters*, 61(14-15), pp.3138-3141.
83. Tsuchiya, H., Tenjimbayashi, M., Moriya, T., Yoshikawa, R., Sasaki, K., Togasawa, R., Yamazaki, T., Manabe, K. and Shiratori, S., 2017. Liquid-infused smooth surface for improved condensation heat transfer. *Langmuir*, 33(36), pp.8950-8960.
84. Seo, D., Shim, J., Lee, C. and Nam, Y., 2020. Brushed lubricant-impregnated surfaces (BLIS) for long-lasting high condensation heat transfer. *Scientific reports*, 10(1), pp.1-13.

85. Smith, J.D., Dhiman, R., Anand, S., Reza-Garduno, E., Cohen, R.E., McKinley, G.H. and Varanasi, K.K., 2013. Droplet mobility on lubricant-impregnated surfaces. *Soft Matter*, 9(6), pp.1772-1780.
86. Bohn, H.F. and Federle, W., 2004. Insect aquaplaning: *Nepenthes* pitcher plants capture prey with the peristome, a fully wettable water-lubricated anisotropic surface. *Proceedings of the National Academy of Sciences*, 101(39), pp.14138-14143.
87. Wu, Y., Zhou, S., You, B. and Wu, L., 2017. Bioinspired design of three-dimensional ordered tribrachia-post arrays with re-entrant geometry for omniphobic and slippery surfaces. *ACS nano*, 11(8), pp.8265-8272.
88. Song, T., Liu, Q., Zhang, M., Chen, R., Takahashi, K., Jing, X., Liu, L. and Wang, J., 2015. Multiple sheet-layered super slippery surfaces based on anodic aluminum oxide and its anticorrosion property. *RSC advances*, 5(86), pp.70080-70085.
89. Wang, P., Zhang, D., Sun, S., Li, T. and Sun, Y., 2017. Fabrication of slippery lubricant-infused porous surface with high underwater transparency for the control of marine biofouling. *ACS applied materials & interfaces*, 9(1), pp.972-982.
90. Stamatopoulos, C., Hemrle, J., Wang, D. and Poulikakos, D., 2017. Exceptional anti-icing performance of self-impregnating slippery surfaces. *ACS Applied Materials & Interfaces*, 9(11), pp.10233-10242.
91. Hao, C., Li, J., Liu, Y., Zhou, X., Liu, Y., Liu, R., Che, L., Zhou, W., Sun, D., Li, L. and Xu, L., 2015. Superhydrophobic-like tunable droplet bouncing on slippery liquid interfaces. *Nature communications*, 6(1), pp.1-7.
92. Zhang, J., Gu, C. and Tu, J., 2017. Robust slippery coating with superior corrosion resistance and anti-icing performance for AZ31B Mg alloy protection. *ACS applied materials & interfaces*, 9(12), pp.11247-11257.
93. Zhang, P., Chen, H., Zhang, L., Zhang, Y., Zhang, D. and Jiang, L., 2016. Stable slippery liquid-infused anti-wetting surface at high temperatures. *Journal of Materials Chemistry A*, 4(31), pp.12212-12220.
94. Manna, U. and Lynn, D.M., 2015. Fabrication of liquid-infused surfaces using reactive polymer multilayers: principles for manipulating the behaviors and mobilities of aqueous fluids on slippery liquid interfaces. *Advanced Materials*, 27(19), pp.3007-3012.
95. Wang, X.Q., Gu, C.D., Wang, L.Y., Zhang, J.L. and Tu, J.P., 2018. Ionic liquids-infused slippery surfaces for condensation and hot water repellency. *Chemical Engineering Journal*, 343, pp.561-571.

96. Plechkova, N.V. and Seddon, K.R., 2008. Applications of ionic liquids in the chemical industry. *Chemical Society Reviews*, 37(1), pp.123-150.
97. Armand, M., Endres, F., MacFarlane, D.R., Ohno, H. and Scrosati, B., 2011. Ionic-liquid materials for the electrochemical challenges of the future. In *Materials For Sustainable Energy: A Collection of Peer-Reviewed Research and Review Articles from Nature Publishing Group* (pp. 129-137).
98. Tani, M., Kawano, R., Kamiya, K. and Okumura, K., 2015. Towards combinatorial mixing devices without any pumps by open-capillary channels: fundamentals and applications. *Scientific reports*, 5, p.10263.
99. Rykaczewski, K., Paxson, A.T., Staymates, M., Walker, M.L., Sun, X., Anand, S., Srinivasan, S., McKinley, G.H., Chinn, J., Scott, J.H.J. and Varanasi, K.K., 2014. Dropwise condensation of low surface tension fluids on omniphobic surfaces. *Scientific reports*, 4, p.4158.
100. Sett, S., Yan, X., Barac, G., Bolton, L.W. and Miljkovic, N., 2017. Lubricant-infused surfaces for low-surface-tension fluids: Promise versus reality. *ACS applied materials & interfaces*, 9(41), pp.36400-36408.
101. Wexler, J.S., Jacobi, I. and Stone, H.A., 2015. Shear-driven failure of liquid-infused surfaces. *Physical review letters*, 114(16), p.168301.
102. Liu, Y., Wexler, J.S., Schönecker, C. and Stone, H.A., 2016. Effect of viscosity ratio on the shear-driven failure of liquid-infused surfaces. *Physical Review Fluids*, 1(7), p.074003.

## **Chapter 4: Technoeconomic Analysis of Textured Surfaces for Improved Condenser Performance in Thermoelectric Power Plants**

*The work reported in this chapter is the basis for the following journal publication:*

K. Nithyanandam, P. Shoaie and R. Pitchumani, “Technoeconomic Analysis of Thermoelectric Power Plant Condensers with Superhydrophobic and Liquid Infused Nonwetting Surfaces,” *Energy*, In Review, 2020.

Engineering micro and nano-scale textures on surfaces have shown significant potential in improving the efficiency of energy applications. This chapter investigates the dynamic performance and economic benefits of using textured surfaces fabricated using an electrodeposition process for condenser tubes in thermoelectric power plants. The textured surfaces are expected to provide enhanced performance by deterring fouling thereby reducing fouling resistance and promoting dropwise condensation of the steam on the shell side. Using a thermal resistance network of a shell and tube condenser, detailed parametric studies are carried out to investigate the effect of various design parameters — tube diameter, number of tubes — and operating parameters — cooling water velocity, fouling factor, and diurnal fluctuations in cooling water temperature — on the annual condenser performance measured in terms of its electric energy output of a representative 550 MW coal-fired power plant. A cost modeling tool and a new levelized cost of condenser (LCOC) metric have been developed to evaluate the economic and performance benefits of enhanced condenser designs. The LCOC is defined as the ratio of the lifetime cost of condenser (and associated costs such as coating, operation & maintenance) to the total electric energy produced by the thermoelectric power plant. The physical model is coupled with a numerical optimization method to identify the optimal design and operating parameters of the textured tubes that minimizes LCOC. Overall, the study presents the first effort to construct and analyze enhanced condenser design with textured tube surfaces on annual thermoelectric power plant performance and compares it against the baseline condenser design with plain tubes.

## 4.1 Introduction

The most common type of thermoelectric power plants generate electricity by utilizing the heat of combustion of fuel to convert water into steam in a boiler that turns a turbine. The steam exiting the turbine is condensed back to water in a shell and tube condenser before it is returned to the boiler. There is an increasing need to develop high performance and efficient condenser designs with reduced thermal resistance to increase the amount of power generated and lessen the impacts on water quality from thermoelectric power plants [1]. In water-stressed regions such as the southwestern US, there is also a greater impetus to using nontraditional water sources such as municipal or seawater for cooling in power plant condensers. Increased plant efficiency with reduced detrimental effects on water is critical to meet the Environmental Protection Agency (EPA) regulations for power plants [2]. Robust and durable superhydrophobic surfaces (SHS) or slippery liquid-infused porous surfaces (SLIPS) have a great potential for heat transfer enhancement [3-5], fouling rate reduction [6-8], and drag reduction [9]. Replacing plain tubes in a shell and tube condenser with textured tube surfaces can enhance overall condenser performance resulting in increased plant power output and higher plant efficiency by allowing condenser operation at lower pressures or stronger vacuum.

Superhydrophobic surfaces have been experimentally demonstrated to improve condensation heat transfer performance by effectively avoiding the formation of condensed liquid film and instead promoting dropwise condensation [3-5,10-12]. The combination of multiscale hierarchical morphology and low surface energy of textured surfaces leads to high contact angle and low roll-off angles for high droplet mobility and easy removal of condensate from the textured surfaces. In SLIPS, lubricant fluid of sufficiently low vapor pressure is infused (thus replacing air) within the roughness gaps of textured surfaces for performance enhancement even at larger supersaturations, thus eliminating flooding concerns of the surface structure while maintaining low droplet adhesion [13]. It is reported in the literature that the heat transfer coefficient for dropwise condensation is typically more than 5 to 10 times compared to the film wise condensation [3,14-16]. During a typical condenser operation under vacuum, non-condensable gases

(NCG) in the shell are observed to blanket the exterior plain tube surface and decrease the heat transfer rates between the steam and cooling water [17]. On the other hand, Ma et al. [18] showed that textured superhydrophobic surfaces in the presence of NCG can sustain effective dropwise condensation of steam even at high NCG concentrations.

In power plant condensers, the dissolved solids in cooling water flowing through the tubes cause deposition fouling on the interior surface of the tubes that lead to additional thermal resistance. This decreases the heat transfer rate between the steam and cooling water; and consequently, the efficiency and economics of the power plant are impacted [19]. Studies on textured surfaces have shown that textured surfaces delay fouling occurrence. It has been shown that superhydrophobic surfaces exhibit excellent repellency and low adhesion properties in comparison with plain surfaces [20-22]. In addition, Feng et al. [23] showed that the superhydrophobicity of textured surfaces subjected to precipitation fouling can be regenerated by removing the fouled particles through abrasion. Superhydrophobic surfaces also demonstrate characteristics that can be applied to drag reduction in laminar or turbulent flows [24-26]. The friction pressure drop for fluid flow through the tubes or channels with textured surfaces can be effectively reduced, and the convective heat transfer coefficient is also improved to a certain degree, which is attributed to the acceleration of fluid velocity [25]. However, Lv and Zhang [24] have shown that the heat transfer enhancement could be inhibited by the air cavities of the superhydrophobic surfaces in some scenarios.

The primary requirement for achieving superhydrophobicity is the texturing of surfaces to have hierarchical or multiscale asperity structures with low surface energy such that the water contact angles are greater than  $150^\circ$  [27-29]. Fabrication of SLIPS consists of first generating a micro/nano-porous surface into which a lubricant liquid is infused in a second step to achieve the non-wetting coating. While the liquid infusion step is relatively straightforward, critical in this fabrication process is the first step of producing a porous surface. The most common templating and micro-patterning techniques used in the literature are based on nanocasting, plasma etching, magnetron sputtering, or similar means [30-33]. Nevertheless, they typically require elaborate templating or patterning and are not easily scalable to high-volume production. In this study, fractal textured surfaces fabricated from a two-step industrially prevalent

electrodeposition process is considered [27-29]. Schematic of the sample of fractal textured surface and its morphology is depicted in Fig. 1. Since the superhydrophobic surfaces are generated inherently on the substrate material, the resulting surface integrity and durability are significantly higher than fabricated by other means [34,35]. Also, electrodeposition is applicable to a wide choice of metals and metal alloys than most of the other patterning techniques.

Several studies in the literature have investigated the effect of operating and design parameters on the condenser performance [36-42]. The numerical studies have mostly employed a lumped condenser performance model based on  $\epsilon$ -NTU approach for on-line fouling monitoring and performance optimization. These studies are limited to a condenser with plain tubes and thermal performance characterization. A system-driven technoeconomic approach that examines the lifetime cost of enhanced condensers with textured surfaces is necessary to evaluate its benefits for integration with thermoelectric power plants, which forms the focus of the present study. A thermo-economic model of novel condenser design with textured surfaces is developed and integrated with a performance model of a representative 550 MWe subcritical thermoelectric power plant [19]. A systematic parametric analysis is conducted to analyze the effect of various design and operating parameters of the condenser on the annual net electric energy output, number of outages, and levelized cost of the condenser (LCOC). The analysis is performed for a condenser with textured tube surfaces, hereby referred to as *enhanced condenser*, and compared against the baseline performance metrics obtained for a condenser with plain tubes, hereby referred to as *baseline condenser*. The LCOC metric developed in this study is defined as the ratio of the lifetime cost of the condenser to the total electric energy produced by the thermoelectric power plant. A numerical optimization procedure was incorporated to find the optimal design and operating configuration that provides the minimum LCOC for various reduction rates and dropwise heat transfer coefficient values. Based on the cost-benefit trade-off analysis, the design space for the enhanced condenser that provides an economically viable solution compared to the baseline condenser and the corresponding optimal parameters are identified.

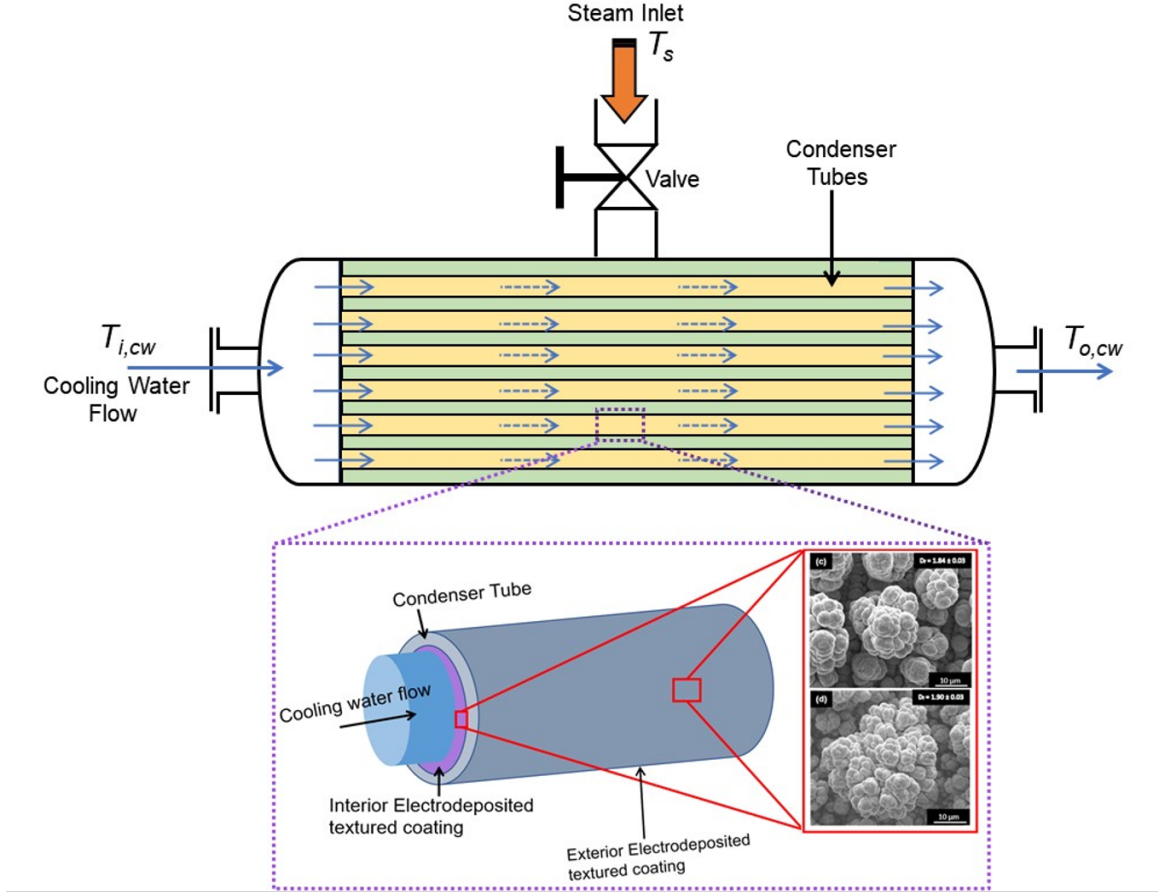


**Figure 1.** Schematic illustration of condenser with textured tubes and SEM morphologies of textured superhydrophobic surfaces fabricated by the electrodepositing process [27].

## 4.2 Model and Analysis Methodology

### 4.2.1 Condenser and Power Plant Performance model

A thermoelectric power plant with a constant condenser heat rejection rate ( $\dot{Q}_c$ ) is considered in this analysis. The commonly used condenser configuration is a horizontal shell and tube heat exchanger with steam condensing on the exterior of the tubes in the shell and cooling water flowing in the tubes (Fig. 1). The main governing equations used in the condenser performance predictions are:

$$(UA_o)N_t\Delta T_{lmt\Delta} = \dot{m}_{cw}c_{cw}(T_{o,cw} - T_{i,cw}) = \dot{Q}_c \quad (1)$$

where  $\Delta T_{lmt\Delta}$  is the logarithmic mean temperature difference between the cooling water flow and the condensing steam given by:

$$\Delta T_{lmt\delta} = \frac{(T_{o,cw} - T_{i,cw})}{\ln \left( \frac{T_s - T_{i,cw}}{T_s - T_{o,cw}} \right)} \quad (2)$$

In Eqs. (1) and (2),  $N_t$  is the number of tubes in the condenser,  $T_{i,cw}$  is the inlet temperature of cooling water,  $T_{o,cw}$  is the outlet temperature of cooling water from the condenser,  $T_s$  is the steam condensing temperature which is a function of the turbine back pressure ( $\Pi_s$ ) and  $UA_o$  is the overall thermal conductance given by:  $UA_o = 1/R_T$ . The total thermal resistance ( $R_T$ ) is obtained from:

$$R_T = R_{cw} + R_f + R_w + R_c \quad (3)$$

The convection resistance of the cooling water flow in tubes is given by:  $R_{cw} = 1/h_{fc}A_i$  and steam condensation resistance is given by  $R_c = 1/h_cA_o$ , where  $h_{fc}$  and  $h_c$  are the forced convection and condensation heat transfer coefficients, respectively.  $A_i = \pi d_i L_t$  and  $A_o = \pi d_o L_t$  are internal and external surface areas of the cooling water tube, respectively in which  $d_i$  and  $d_o$  are the inner and outer tube diameter, and  $L_t$  denotes the tube length.  $R_w$  is the conduction resistance due to the tube wall given by  $R_w = \ln(d_o/d_i)/2\pi L_t k_w$  where  $k_w$  is the thermal conductivity of the tube wall material. The internal convection heat transfer coefficient for the turbulent cooling water flow in tubes is calculated using the Dittus-Boelter correlation [43]:

$$h_{fc} = 0.023 \times Re_d^{4/5} \times Pr^{0.4} \quad (4)$$

where  $Re_d$  is the Reynolds number based on the tube inner diameter ( $d_i$ ) given by  $Re_d = \rho_{cw} V_{cw} d_i / \mu_{cw}$  and  $Pr$  is the Prandtl number of the cooling water flow given by  $Pr = \mu_{cw} c_{cw} / k_{cw}$ .  $\rho_{cw}$ ,  $\mu_{cw}$ ,  $c_{cw}$  and  $k_{cw}$  are the density, viscosity, specific heat and thermal conductivity of the cooling water. No improvement for convection heat transfer inside textured tubes has been considered for the enhanced condenser as revealed by Lv and Zhang's study [24].

The heat transfer coefficient for filmwise horizontal condensation outside the plain tubes in baseline condenser is calculated using the relationship developed by Nusselt [44]:

$$h_c = h_{fwc} = 0.725 \left[ \frac{k_l \rho_l (\rho_l - \rho_g) g \lambda^r}{\mu_l d_o (T_s - T_w)} \right]^{1/4} \times \frac{1}{N_r^{1/6}} \quad (5)$$

In Eq. (5) subscript ‘*l*’ refers to the liquid water phase, subscript ‘*g*’ refers to the vapor phase,  $g = 9.81 \text{ m/s}^2$  is the acceleration due to gravity,  $\lambda'$  is the modified latent heat of steam,  $d_o$  is the outer diameter of the tubes,  $T_w$  is the wall temperature and  $N_r$  is the number of tube rows in the condenser. The wall temperature is calculated from:

$$T_w = T_s - \left[ \frac{UA_o}{h_c A_o} \right] \quad (6)$$

The modified latent heat of steam is calculated as suggested by Rosenhow [44]:  $\lambda' = \lambda + 0.68c_l(T_s - T_w)$  where  $\lambda$  is the latent heat of steam which is a function of the steam condensation temperature ( $T_s$ ) or turbine backpressure. The number of tube rows ( $N_r$ ) is calculated from  $N_r = \frac{D_b}{p_t}$ . The bundle diameter ( $D_b$ ) is estimated using [45]:  $D_b = d_o(N_t/k_1)^{1/n_1}$  in which the constants  $k_1$  and  $n_1$  are functions of tube pitch layout and the number of tube pass. In this analysis, a square tube layout with tube pitch of  $p_t = 1.25d_o$  is considered and the number of tube pass is assumed to be 1 for which the constants are  $k_1 = 0.215$  and  $n_1 = 2.207$  [45].

The heat transfer coefficient for dropwise steam condensation outside the tubes in the enhanced condenser is calculated using the relationship recommended by Griffith [16,46]:

$$h_c = h_{dwc} = 51104 + 2044 \times T_s \quad (7)$$

The internal fouling resistance follows the asymptotic fouling resistance model developed by Nebot et al. [47] for power plant condensers cooled with seawater, which is representative of non-traditional water sources:

$$R_f(t) = \frac{R''_{f,\infty}}{A_i \left\{ 1 + \left[ \frac{R''_{f,\infty}}{R''_{f,i}} - 1 \right] \exp(-K_f R''_{f,\infty} t) \right\}} \quad (8)$$

where  $K_f$  is the fouling rate in  $\text{W/m}^2\text{-K-day}$ ,  $R''_{f,i}$  and  $R''_{f,\infty}$  are the area-integrated initial and asymptotic fouling resistance values in  $\text{m}^2\text{-K/W}$ , and  $t$  is time expressed in days.  $K_f$  and  $R''_{f,\infty}$  are dependent on the velocity of cooling water ( $V_{cw}$ ) and tube material. For the baseline condenser with plain tubes, the default values for fouling rate as obtained from Nebot et al [47] represented by  $K_{f,p}$  in Eq. (9) was used.

$$K_{f,p} = \{-0.074 \times V_{cw}^2 + 0.680\}; V_{cw} \leq 1.85 \frac{\text{m}}{\text{s}} \quad (9a)$$

$$K_{f,p} = \{0.750 \times V_{cw}^2 - 3.027V_{cw} + 3.573\}; V_{cw} > 1.85 \frac{\text{m}}{\text{s}} \quad (9b)$$

In enhanced condenser configuration, the interior textured surfaces are expected to reduce fouling rate [20,48,49]. Since the impact of a reduction in  $K_f$  for textured surfaces are not sufficiently characterized in the literature, a parametric study of the reduction factor on fouling rate from the baseline values,  $K_{f,p}$  was conducted to quantify its impact on the annual plant performance.

The turbine power output is calculated using the correlation proposed by Webb [50] as expressed in Eq. (8). It provides a simplified method to couple turbine and condenser performances without the need for comprehensive thermodynamic calculations for working fluid at each stage of the cycle.

$$P_e = \frac{\dot{Q}_c}{HR'(1+HR_c)} - \frac{\Delta\mathcal{P}_{cw}N_t}{\rho_{cw}\eta_p} \quad (10)$$

$HR' = 2.942 \text{ kW}_t/\text{kW}_e$  is the heat rate at the rated turbine back pressure of 3 in Hg abs for fossil plant and  $HR_c$  is the turbine heat rate correction factor obtained from Webb [50]. The second term on the right is the pump power consumption and  $\Delta\mathcal{P}_{cw}$  is the frictional pressure drop associated with cooling water flow in tubes which is calculated from  $\Delta\mathcal{P}_{cw} = f \frac{L_t}{2d_i} \rho_{cw} V_{cw}^2$ , where  $L_t$  is the length of the condenser tubes and  $f$  is the Darcy friction factor calculated using the Colebrook equation [51]. In Eq. (8),  $\dot{m}_{cw}$  is the mass flow rate of cooling water calculated from  $\dot{m}_{cw} = \rho_{cw} V_{cw} N_t \pi d_i^2 / 4$  and  $\eta_p$  is the pump efficiency which is assumed to be 0.6. It is to be noted that the pump electric energy consumption was less than 0.1% of the total electrical energy generated from the power plant. Since the total pumping power is negligible compared to the total power generation, the reduction in pumping power due to textured tubes is not considered in this study. The condenser effectiveness is calculated from:  $\varepsilon = 1 - \exp(UA_o N_t / \dot{m}_{cw} c_{cw})$ . From the net electric power calculated using Eq. (9), the cycle efficiency can be expressed as [50]:

$$\eta = \frac{P_e}{\dot{Q}_c} \times \left\{ 1 - \frac{1}{HR'(1+HR_c)} \right\} \quad (11)$$

#### 4.2.2 Cost model

A cost-modeling tool was developed and integrated with the condenser performance model (Section 2.1) to estimate the techno-economic benefits of enhanced condenser compared to baseline condenser. The total capital expenditure for the condenser ( $C_T$ ) can be expressed as the summation of heat exchanging condenser equipment cost ( $C_{HX}$ ) and the electrodeposition cost ( $C_E$ ):  $C_T = C_{HX} + C_E$ . For a baseline condenser, the electrodeposition cost,  $C_E = 0$ . Feng and Rangaiah [52] compared the predictions of several methods proposed in the literature for estimation of heat exchanger equipment cost and concluded that the methodology proposed by Seider et al. [53] closely agreed with the actual cost. Following the cost estimation method outlined by Seider et al. [53], the equipment cost for floating-head type heat exchanger can be expressed as:

$$C_{HX} = 3.291 \times F_p \times F_m \times F_l \times \exp\{11.667 - 0.8709 [\ln(A_o N_t)] + 0.0986[\ln(A_o N_t)]^2\} \quad (12)$$

where  $F_p$  represents pressure factor,  $F_m$  is the material factor, and  $F_l$  is the tube length factor. The value 3.291 in Eq. (12) is the bare module factor that includes the cost associated with equipment purchase, field materials used for installation, installation labor, and indirect expenses. The pressure factor is calculated from:  $F_p = 0.9803 + 0.018(\Pi_{max}/100) + 0.0017(\Pi_{max}/100)^2$ , where  $\Pi_{max}$  is the maximum steam pressure in the condenser. The condenser operation is limited to a maximum steam pressure (or turbine backpressure) of  $\Pi_{max} = 18.63$  kPa based on the value suggested in the literature [19,54]. The material factor ( $F_m$ ) is calculated from:  $F_m = a + \left(\frac{A_o N_t}{100}\right)^b$  where the values of constants  $a$  and  $b$  can be obtained from Seider et al. [53] for the various combinations of shell and tube material of construction.

In the enhanced condenser, both the interior and exterior surfaces of the tubes are textured through the electrodeposition process. The electrodeposition cost ( $C_E$ ) for textured tubes is calculated based on the method proposed by Mazzilli et al. [55], which involves the summation of coating material cost ( $C_{E,cm}$ ), labor cost ( $C_{E,l}$ ), and equipment cost ( $C_{E,eq}$ ). The material cost is given by:

$$C_{E,cm} = \rho_{cm} \times (A_o + A_i) \times N_t \times b_{cm} \times \bar{C}_{cm} \quad (13)$$

where  $\rho_{cm}$ ,  $b_{cm}$ ,  $\bar{C}_{cm}$  represents the density, thickness, and cost per unit mass of the coating material, respectively. The labor cost depends on hourly wages and the process

throughput time that includes the time employed for electrodeposition of the parts ( $t_d$ ) and the set-up time ( $t_s$ ). The set-up time involves time spent on part preparation, changing the baths or electrodes, and post-processing. The labor cost is calculated from:

$$C_{E,l} = N_t \left[ \dot{C}_d \times \frac{(A_o + A_i)}{A_b} \times t_d + \dot{C}_s \times t_s \right] \quad (14)$$

In Eq. (14)  $\dot{C}_d$  and  $\dot{C}_s$  are the hourly labor costs related to electrodeposition time and set-up time. The values obtained from Mazzilli et al. [55] are  $\dot{C}_d = 22.5$  \$/h and  $\dot{C}_s = 45$  \$/h.  $A_b$  represents the bath capacity and this study assumes the standard maximum industrial production capacity of 4 m<sup>2</sup> [55].  $t_s$  is the setup time per part and the standard value for industrial-scale large production batch is 4e<sup>-4</sup> h/part [55]. The time to electrodeposit ( $t_d$ ) depends on the coating thickness ( $b_{cm}$ ), density of the coating material ( $\rho_{cm}$ ), current intensity ( $I$ ), electrostatic equivalent ( $E$ ), and current yield ( $Y$ ):  $t_d = b_{cm}\rho_{cm}/I \times E \times Y$ . The typical values of  $I$ ,  $E$ ,  $Y$  for different coating materials can be found in Ref. [55]. In this study, electrodeposition of brass on aluminum-brass tubes ( $I = 200$  A/m<sup>2</sup>,  $E = 1.204e^{-3}$  kg/A-h,  $Y = 0.7$ ) and nickel on titanium tubes ( $I = 400$  A/m<sup>2</sup>,  $E = 1.04e^{-3}$  kg/A-h,  $Y = 0.95$ ) were considered. The coating thickness ( $b_{cm}$ ) was kept constant at 30 μm and the coating material cost ( $\bar{C}_{cm}$ ) for brass and nickel obtained from Mazzilli et al. [56] are 3 \$/kg and 12 \$/kg, respectively. The cost related to the use of electrodeposition equipment is calculated from:  $C_{E,eq} = \dot{C}_e N_t \left[ \frac{(A_o + A_i)}{A_b} \times t_d + t_s \right]$  where  $\dot{C}_e$  is empirically estimated to be 5.25 \$/h [55]. It is noted that the fabrication cost of SLIPS is also comparable with that of textured superhydrophobic surfaces as an additional step to infuse the porous structure with lubricant is accomplished by means of a simple dip-coating process, which has a negligible impact on the overall cost. Hence, the cost model developed here is applicable for both textured superhydrophobic and SLIPS surfaces.

To evaluate cost-benefit of patterned surface tubes on condenser performance, levelized cost of condenser (LCOC) that accounts for the capital cost, initial application cost, condenser maintenance or cleaning cost, reapplication cost, and related downtime is defined in Eq. (15):

$$LCOC = \frac{[C_T + (C_M \times N_o \times N_y) + (C_E \times \gamma \times N_y)]}{Q_e \times N_y} \quad (15)$$

$C_M$  is the condenser maintenance cost which includes the cost of condenser cleaning and is assumed to be \$13,500 as proposed by Walker et al. [19].  $N_o$  is the number of outages or downtime days and its calculation methodology is explained in Section 2.3 and shown in Figure 2.  $\gamma$  is the reapplication interval for electrodeposition of the condenser tubes which is set to be once per year and assumed to take place on the final day of the year as part of plant's annual maintenance procedure.  $Q_e$  is the net annual electrical energy generated by the power plant which is computed from  $Q_e = \sum_{n_d=1}^{n_d=365} P_e \times 24$  where  $n_d$  represents the day of the year and 24 is the number of hours in a day. The LCOC is calculated for a total system lifetime of  $N_y = 20$  years.

### 4.2.3 Numerical Procedure

The complete formulation—including the condenser performance model and the cost model—was implemented in Python [56]. A 550 MWe turbine design output power is considered in this analysis for which the condenser heat rejection at the rated turbine backpressure of 3 in Hg abs is  $\dot{Q}_c = 737.6$  MWt [50]. The annual simulations involve determining the steam condensation pressure in the shell and the cooling water outlet temperature for each day through an iterative process as illustrated in Figure 2. The influence of design parameters namely, tube diameter ( $d_{t,o}$ ), number of tubes ( $N_t$ ) on the annual plant performance is evaluated in this study. The tube was fixed at the standard length of 6 m. The sensitivity of operating parameters namely, the velocity of cooling water ( $V_{cw}$ ) in the tubes and condenser tube material of construction is also studied. The condenser shell material is constructed of carbon steel while the influence of tube materials namely, titanium and aluminum-brass for which Nebot et al. [47] characterized the fouling kinetics was considered in this study. Based on stress and fouling allowance considerations, a standard wall thickness of 0.71 mm and 1.254 mm was used for titanium and aluminum-brass tubes as suggested by Thulukkanam [57]. For a given set of design, operating and material parameters, the steam condensation pressure varies due to daily fluctuations in the cooling water inlet temperature and the transient evolution of fouling resistance in the condenser tubes. The data for daily variations of cooling water

inlet temperature was obtained from Walker et al. [19] that is representative of temperature profile typically observed in water-stressed regions such as southwestern US.

As outlined in Figure 2, the computation first involves solving for the cooling water outlet temperature and convection resistance for the fixed  $\dot{Q}_c$ . The next step involves an iterative procedure that determines the converged condensation heat transfer coefficient and steam pressure that satisfies Eq. (1) within an error tolerance of 5 %. If the predicted converged steam pressure exceeds the maximum turbine backpressure value of 18.63 kPa suggested in the literature [19,54], the plant is not operated for the day and shutdown for condenser cleaning operation. Consequently, the number of outages represented by  $N_o$  is incremented by one. This iteration procedure is carried out for all the days of the year and on the final day of the year, the plant is shutdown for annual maintenance on the condenser. The forced condenser maintenance outage on the final day of the year ensures periodicity in the annual plant performance as the initial condition of the transient fouling resistance model is set to  $R_{f,i}$  at the start of each year. The main performance outputs from the model are daily values for cooling water output temperature, steam temperature and pressure, net electric power output, and condenser effectiveness. At the completion of the annual performance simulations, the LCOC is calculated from the capital expenditure and maintenance costs for a system lifetime of 20 years.

## 4.3 Results and Discussion

### 4.3.1 Model Verification

As discussed in Section 2.3, the model involves an iterative update of the steam pressure at every time step to determine the converged operating condition of the condenser. Analogous to grid refinement study in finite element analysis, a systematic refinement study of the pressure increment ( $\Delta\Pi_s$ ) used in the iterative numerical algorithm (Fig. 2) was performed to obtain the best pressure increment step size for the computations. The analysis was conducted for the condenser with 30,000 titanium tubes of outer diameter 0.025 m at the default cooling water velocity of 1.85 m/s. Table 3.1 shows the net annual electricity energy output with progressively decreasing pressure increment step size. It is observed that as  $\Delta\Pi_s$  gets smaller, the solution converges to the

asymptotic region. The difference in  $Q_e$  predicted by  $\Delta\Pi_s = 100$  Pa and  $\Delta\Pi_s = 50$  Pa is 0.03 % which slightly reduces to 0.02% with reduction in  $\Delta\Pi_s$  to 10 Pa while the computational cost increases prohibitively. Hence, the final computations were performed using  $\Delta\Pi_s = 100$  Pa as highlighted by the bold-faced row in Table 3.1.

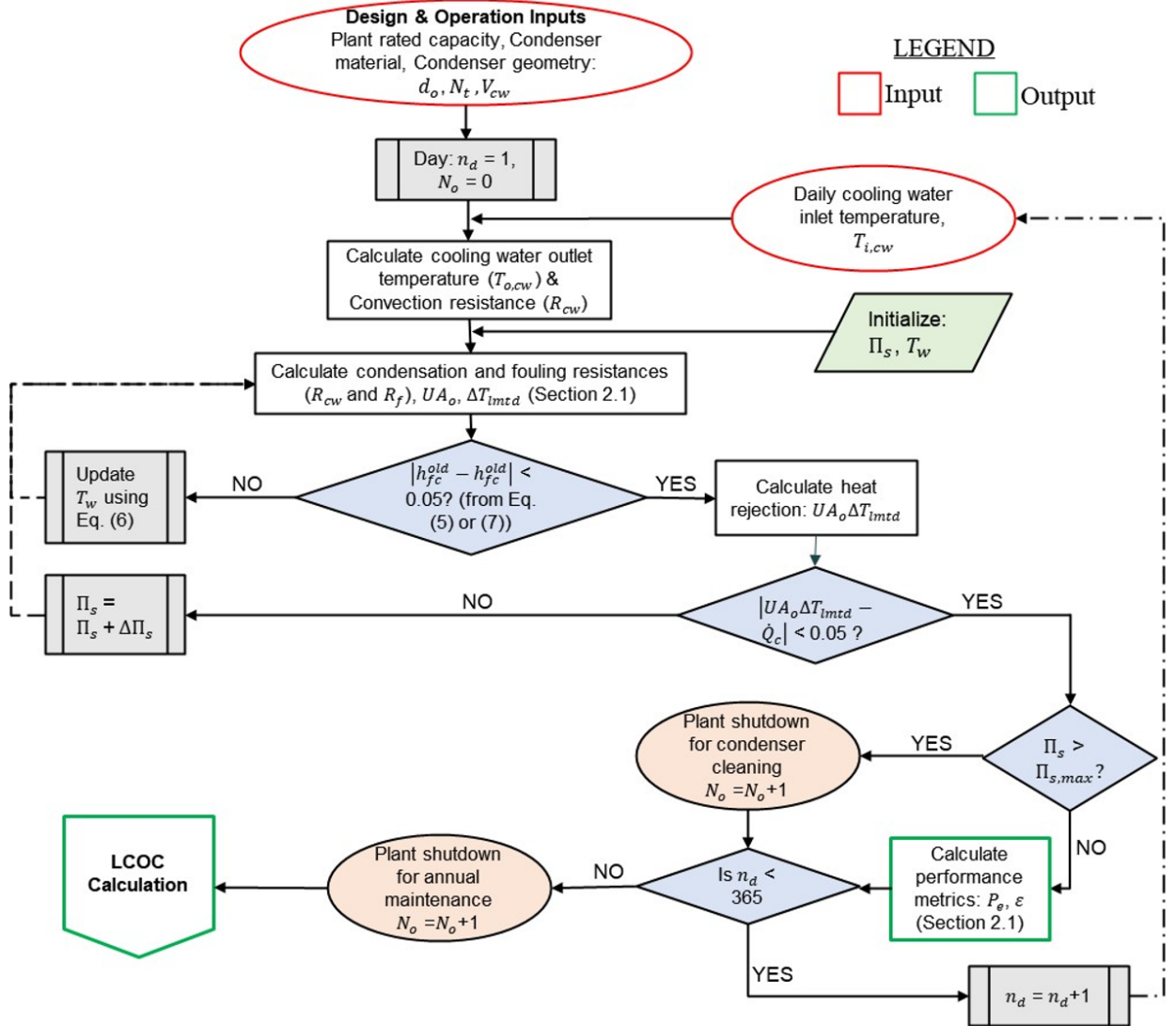


**Figure 2.** Flowchart of the computational procedure for annual thermoelectric power plant performance analysis.

**Table 3.1.** Results of pressure increment step size refinement study. The bold-faced row represents the adopted pressure increment step size in this study

| Pressure Increments, $\Delta\Pi_s$ [Pa] | Predicted Net Annual Energy Output, $Q_e$ [GWhe] | Computational Time [min] |
|---|--|--------------------------|
| 500                                     | 4100.67  | 0.477                    |
| 250                                     | 4438.22  | 0.896                    |
| <b>100</b>                              | <b>4449.39</b>                                   | <b>2.001</b>             |
| 50                                      | 4450.71  | 3.670                    |
| 10                                      | 4451.49  | 37.671                   |

The numerical model developed is validated with results obtained from literature and presented in Fig. 3. Figure 3 compares the predictions of the condensing steam pressure from the present numerical model with the results obtained from Pattnayak et al. [42] and Laskowski [41]. The design details of the shell and tube steam condenser used in a 210 MW thermal power plant are presented in Pattnayak et al. [42]. It consists of 15620 tubes made of cupronickel of outer diameter 0.03 m and 0.001 m wall thickness. The steam pressure (dashed line) obtained from the present numerical model are plotted along with the corresponding values obtained from the model predictions of Pattnayak et al. [42] which are denoted by open circles and measurement data obtained from Laskowski [41], which are denoted by open triangles. The exponential prediction of an increase in steam pressure with an increase in cooling water inlet temperature for the fixed cooling load is consistent with the results obtained from the literature. The average difference between the numerical model prediction and the literature data was calculated to be less than 2.7 % with a standard deviation of 1.3 %. The close agreement of the model prediction results with experimental and numerical data in the literature provides confidence in the validity of the model for detailed parametric studies.

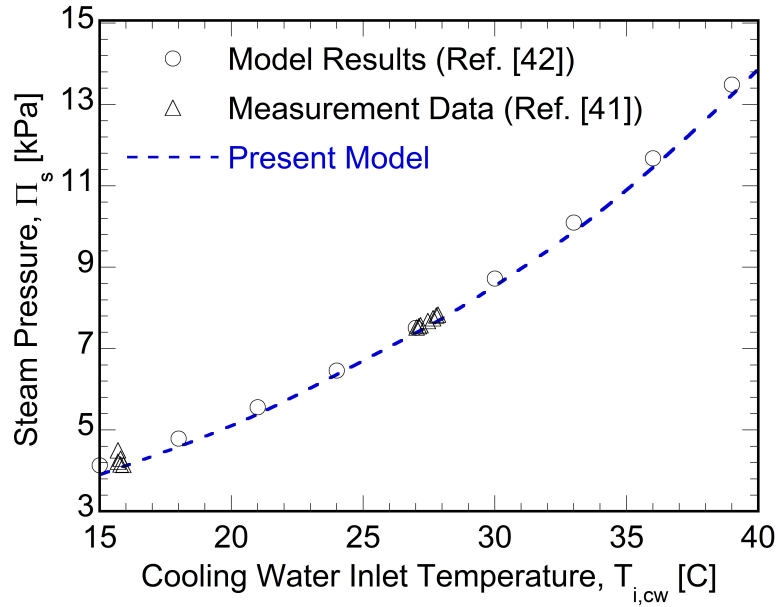


**Figure 3.** Validation of the present numerical model against numerical [42] and measurement [41] data in the literature.

### 4.3.2 Parametric Studies

The effect of change in number of tubes on daily performance outputs for plain titanium tubes is shown in Fig. 4 for the first 90 days of plant operation. The cooling water velocity and condenser tube diameter are fixed at 1.85 m/s and 0.025 m, respectively. Figure 4a depicts the daily variation in fouling resistance for the different number of tubes. The cooling water inlet temperature that is adopted from Walker et al. [19] and used as an input to the model is also shown in Fig. 4a. As the fouling resistance increases, the overall heat transfer coefficient in the condenser decreases that is compensated by an increase in steam pressure (Fig. 4b). For a given cooling water inlet temperature, the increase in steam pressure and the concomitant increase in steam condensation temperature (Fig. 4c) results in a higher temperature difference to meet the cooling load ( $\dot{Q}_c$ ) requirement. Nevertheless, the increase in turbine backpressure decreases net power output from the plant (Fig. 4d) due to reduction in enthalpy difference across the turbine which is calculated using the correlation proposed by Webb

[51] (Eq. (10)). It is observed that for  $N_t = 25,000$  and  $N_t = 30,000$ , the increase in fouling resistance (Fig. 4a) results in steam condensation pressure reaching the critical threshold of  $\Pi_{max} = 18.63$  kPa that leads to plant outage at frequent intervals for condenser maintenance. For instance, in the case of  $N_t = 25,000$  it is observed from Fig. 4d that the plant is shutdown for condenser cleaning on days 22, 45, 64, and 83 during the first 90 days of operation. Increase in number of tubes to  $N_t = 40,000$  increases the thermal conductance ( $UA_o$ ) of the condensing heat exchanger and the condenser can withstand higher fouling resistances while maintaining the steam pressure less than  $\Pi_{max}$  (Fig. 4a and b). Hence, the plant continues to generate power for a longer duration without triggering an outage for condenser cleaning (Fig. 4d). It is observed from Fig. 4d that the increase in thermal conductance or number of thermal units of the condenser with increase in number of tubes leads to a higher electric power generation from the plant. Referring to the curves for  $N_t = 40,000$  and  $N_t = 50,000$  in Fig. 4d, a dip is observed in the electric power generation on day 60. This is due to the increase in cooling water inlet temperature (Fig. 4a), which results in a corresponding increase in steam condensing pressure and temperature (Fig. 4b and c) to maintain the constant cooling duty.

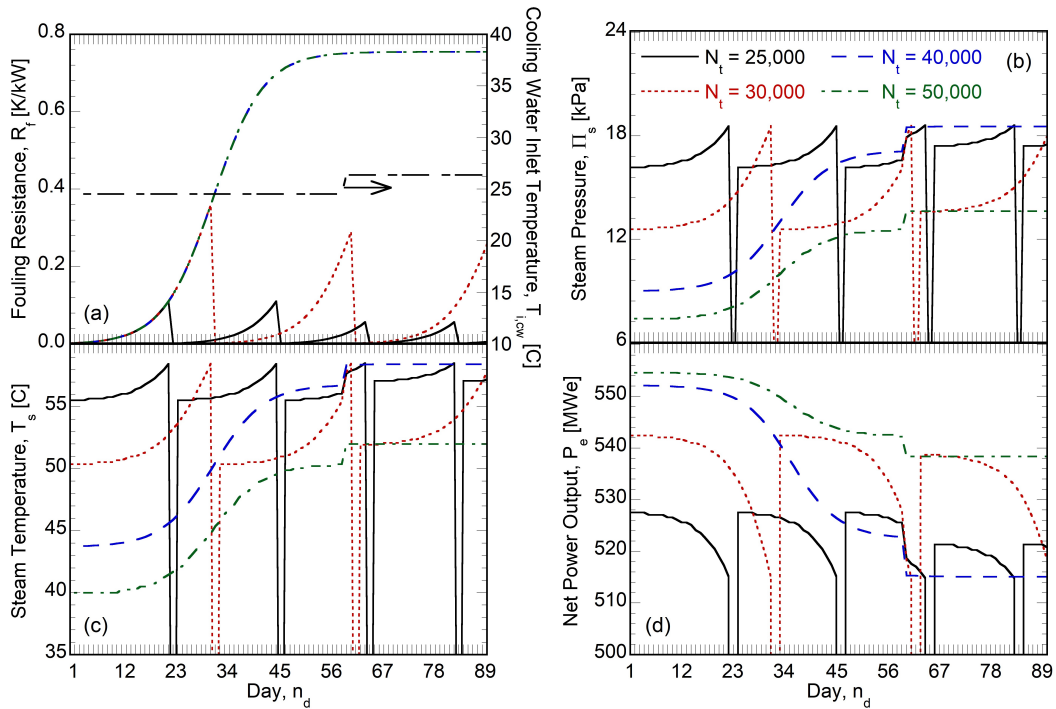


**Figure 4.** Daily variations in (a) fouling resistance, (b) steam condensing pressure and (c) steam condensation temperature, and (d) net electric power output from the plant.

Figure 5a and b depict the variations in monthly net electric energy output and monthly average cooling water outlet temperature from the plant, respectively for the same condenser configuration as used in Figure 4. The average cooling water inlet temperature, which is one of the inputs to the numerical model, is also plotted in Fig. 5b. For the condenser design with tube count of  $N_t = 25,000$ , the monthly net electric energy output during the summer months of mid-April to mid-October is zero (Fig. 5a). The rise in cooling water inlet temperature during these months (Fig. 5b) combined with the small surface area available for heat transfer between steam and cooling water limits the ability of condenser with  $N_t = 25,000$  tubes to meet the cooling duty while maintaining the steam condensation pressure less than  $\Pi_{max}$ . With an increase in the number of tubes, the monthly net energy output as shown in Fig. 5a increases due to the increase in thermal conductance. Figure 5c shows the monthly variation in the number of plant outages required for condenser cleaning. With increase in the number of tubes, the number of outages due to the steam condensation pressure exceeding the critical threshold steadily decreases. This is primarily due to the increase in surface area of the tubes that compensates for the transient increase in overall resistance due to foulant deposition in the inner wall of the tubes from the cooling water (Eq. (8)). The majority of outages are mainly distributed in the months of mid-April to mid-October when the cooling water inlet temperature is high (Fig. 5b). For  $N_t = 40,000$  tubes, in addition to the annual maintenance outage in December, one more outage in July is observed (Fig. 5c) when the cooling water inlet temperature is the highest (Fig. 5b).

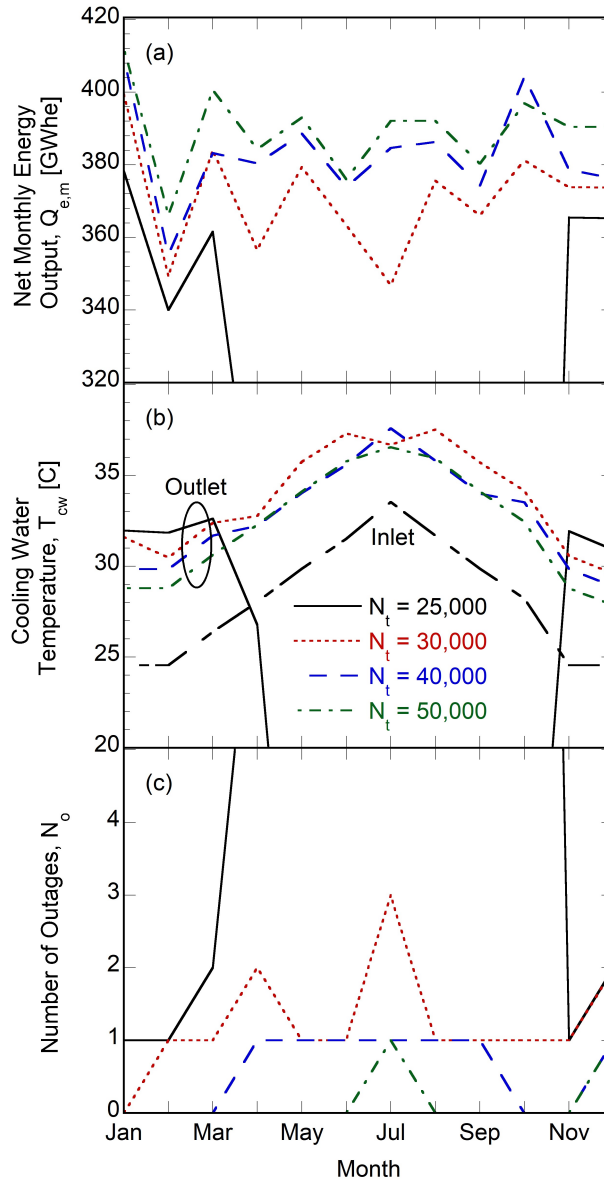


**Figure 5.** Monthly variations in (a) net electric energy output from the plant, (b) cooling water inlet and outlet temperature, and (c) number of plant outages

Figure 6 illustrates the influence of cooling water velocity, tube diameter, and number of plain titanium tubes in the baseline condenser configuration on the annual performance of the plant. The net annual energy output is calculated from the summation of the monthly net electric energy output. The net annual energy output increases with increase in the number of tubes due to the increase in surface area of the tubes (Fig. 6a and c). This is also reflected in the reduction in the number of total outages during the year as

shown in Fig. 6b and d. The drastic decrease in energy output below a certain number of tubes (Fig. 6a and c) is because the condenser is undersized to meet the cooling load, especially during the months when the cooling water inlet temperature is high. This is also observed from the ramp in the number of outages (Fig. 6b and d) below a certain tube number. The variation of plant performance with increase in cooling water velocity is depicted in Fig. 6a and b for the fixed tube diameter of 0.025 m. With increase in cooling water velocity, the fouling rate ( $K_{f,p}$ ) decreases slightly with increase in velocity from 1.50 m/s to 1.85 m/s and increases for water velocities higher than 1.85 m/s [47]. The asymptotic fouling resistance ( $R_{f,\infty}$ ) typically decreases due to higher fluid shear restricting the growth of biofilm. For a fixed tube diameter and number of tubes, an increase in cooling water velocity improves the convection heat transfer coefficient and increases the mass flow rate. For the fixed cooling load, the average temperature of the cooling water decreases with increase in mass flow rate that leads to a reduction in turbine backpressure or steam condensation temperature. Although pumping power consumption increases with increase in cooling water velocity, the impact is negligible compared to the overall power plant capacity. So, overall the increase in cooling water velocity leads to increase in net annual plant electric energy output (Fig. 6a) and decrease in the number of plant outages as observed in Fig. 6b. The fouling rate ( $K_{f,p}$ ) and asymptotic fouling resistance ( $R_{f,\infty}$ ) have a non-linear dependence on the cooling water velocity which results in non-linear increase in the net annual energy output as observed from Fig. 6a. Figure 6c and d shows the effect of tube diameter on plant's net annual energy output for the titanium plain tubes at cooling water velocity of 1.85 m/s. For the fixed velocity and number of tubes, an increase in tube diameter increases the total surface area and increases the mass flow rate of the cooling water for heat exchange with condensing steam. The combined benefits contribute to a decrease in the steam condensation pressure or turbine backpressure and enhance the power cycle efficiency. The number of outages (Fig. 6d) decreases as a result and the net annual energy output (Fig. 6c) increases with increase in tube diameter.

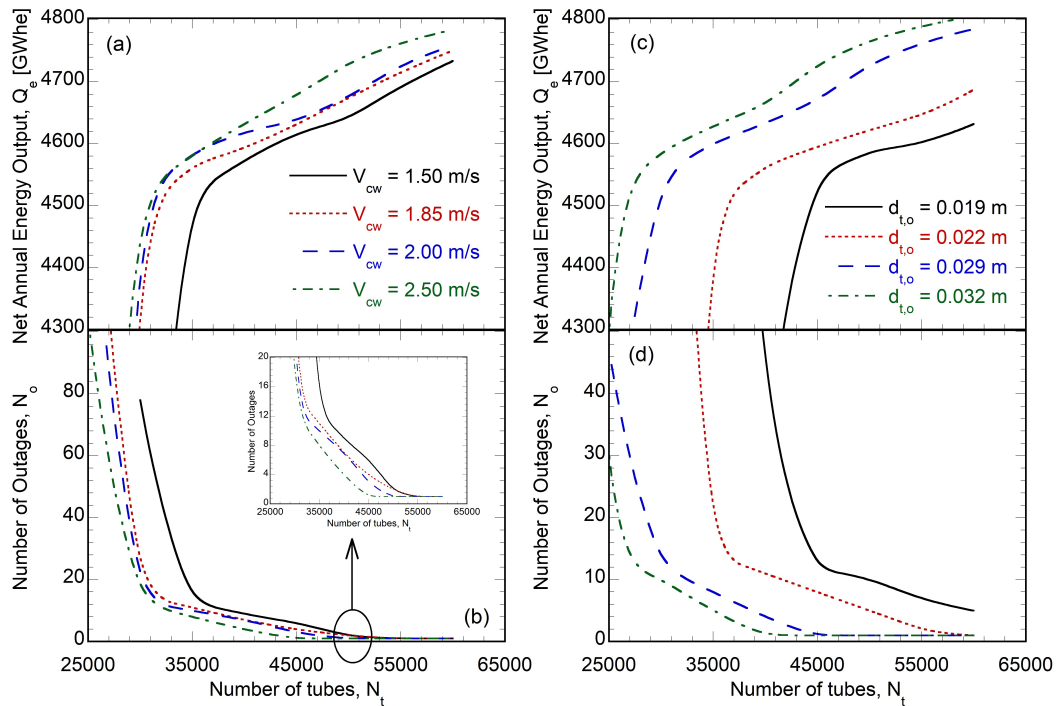


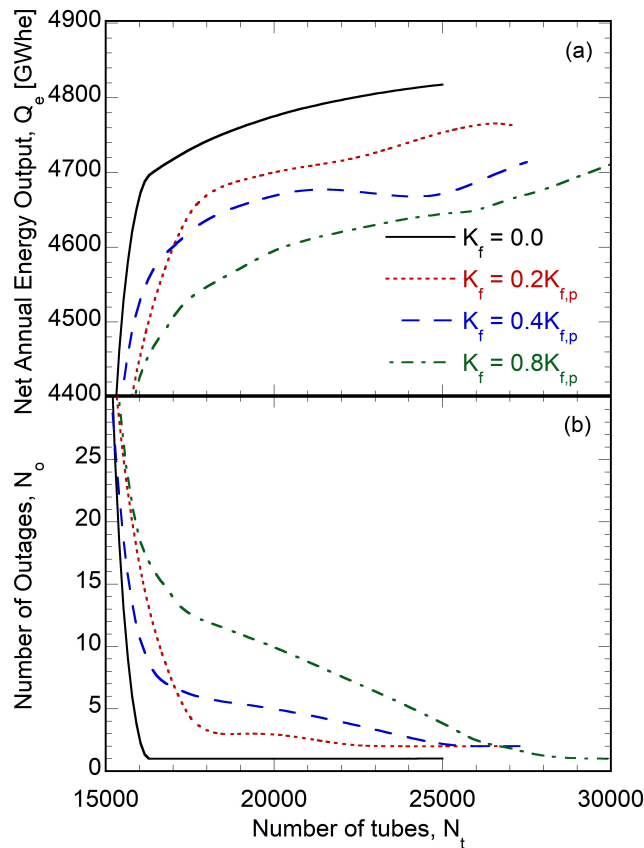
**Figure 6.** Influence of number of plain titanium tubes in the condenser on (a,c) net annual electric energy output from the plant and (b,d) number of plant outages for condenser cleaning and maintenance for various tube diameters and cooling water velocity is 1.85 m/s.

The plots in Fig. 7 are for textured tubes made of titanium material in the *enhanced condenser* configuration for the default tube diameter of 0.025 m and cooling water flow velocity of 1.85 m/s. As discussed in previous sections, since the reduction in fouling rate with textured surfaces is not adequately quantified in the literature, the influence of decrease in fouling rate with respect to the default fouling rate of plain tubes ( $K_{f,p}$ ) on the plant performance is portrayed. The textured tubes promote dropwise condensation on the steam side, which also improves the overall heat transfer performance in the condenser. As observed for the plain tubes, the slope of the decrease in plant output below a certain tube number drastically increases because the condenser is surface area constrained to meet the cooling load (Fig. 7a), which leads to a large number of plant outages (Fig. 7b). Comparing the annual energy output variations obtained for  $V_{cw} = 1.85$  m/s (dotted line) in Fig. 6a against the results for textured tubes in Fig. 7a, it is observed that annual energy output considerably increases at lower tube count in the enhanced condenser configuration. For instance, an annual energy output of 4700 GWhe is achieved with

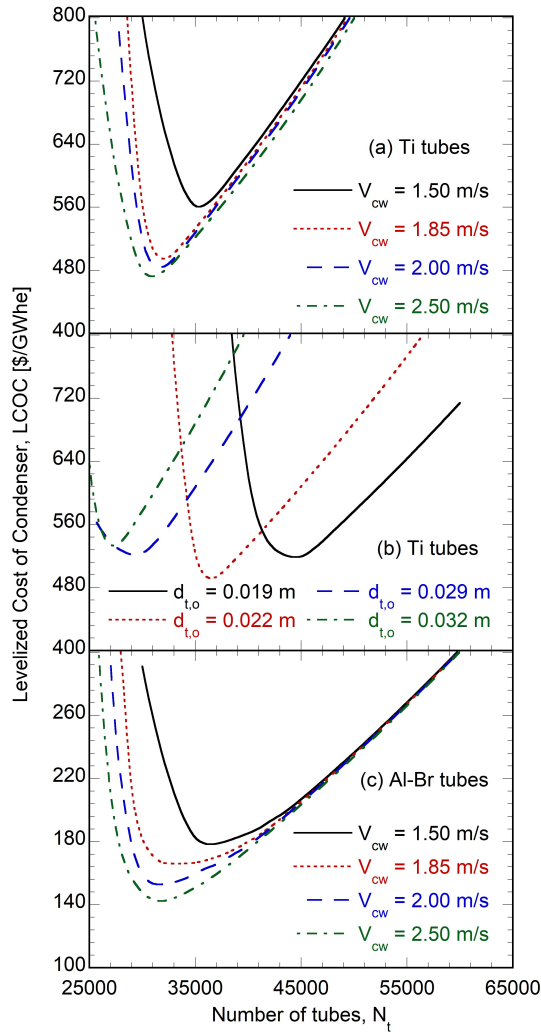
54,500 tubes in the baseline condenser with plain tubes (cf.  $V_{cw} = 1.85$  m/s in Fig. 6a) while the same energy output is obtained with 16,000 tubes and 29,000 tubes for  $K_f = 0$  and  $K_f = 0.8K_{f,p}$ , respectively in enhanced condenser configuration (Fig. 7a). Significant reduction in the number of tubes required between baseline and enhanced condenser for a given energy output is observed even for a marginal reduction in  $K_f$  from  $K_{f,p}$  (plain tubes) to  $0.8K_{f,p}$  due to the higher heat transfer coefficient of dropwise condensation compared to filmwise condensation. An interesting trend observed from Fig. 7a is that below a certain tube count, the net annual energy output increases with increase in  $K_f$  from  $0.2K_{f,p}$  to  $0.4K_{f,p}$  before it decreases again with further increase in fouling rate. This interesting trend is observed for lower number of tubes when number of outages is high (Fig. 7b). The trend reflects an interplay between the energy output difference due to the plant operating at lower cycle efficiency with less number of outages for  $0.2K_{f,p}$  since the turbine back pressure does not reach the cutoff pressure often and at higher efficiency for  $0.4K_{f,p}$  with frequent condenser cleaning. The number of days required for condenser cleaning is set to be 1 in this study based on the information obtained from Walker et al. [19] and increasing the number of cleaning days will change the observed trend.

Based on the results shown in Fig. 6 and the economic model discussed in Section 2.2, the levelized cost of condenser for baseline condenser configuration with plain tubes is illustrated in Fig. 8a and b. It is observed that the LCOC decreases with increase in number of tubes as net annual energy output increases (Fig. 6), reaches a minimum and increases with further increase in number of tubes as the exponential increase in condenser capital cost (Eq. (12)) outweighs the slow increase in energy output (Fig. 6). The minimum LCOC shown in Fig. 8a is achieved at higher cooling water velocities due to the increase in net annual energy output (Fig. 6c) as a result of lower asymptotic fouling resistance and higher cycle efficiency due to reduction in average turbine backpressure. The optimal tube count corresponding to the minimum LCOC for different cooling water velocity aligns with the tube count number corresponding to the change in slope of the increase (decrease) in energy output (number of outages) with respect to the number of tubes as observed in Fig. 6a(b). The variation in LCOC for various tube

diameters made of titanium tubes in Fig. 8b show that the minimum LCOC decreases with increase in tube diameter from 0.019 m to 0.022 m and increases again. The competing effect of increase in condenser capital cost due to increase in total surface area (Eq. (12)) and increase in net energy output with increase in tube diameter (Fig. 6) contributes to the trade-off, thus resulting in an optimum tube diameter around 0.022 m. Figure 8c illustrates the LCOC variation with number of tubes made of aluminum-brass material for different cooling water velocities. Compared to Fig. 8a, it is observed that LCOC for condenser made of aluminum-brass tubes is lower due to the reduced material cost, in spite of the higher fouling rate compared to titanium tubes. Similar to the trend obtained for titanium tubes, the minimum LCOC is obtained for higher cooling water velocities at smaller number of tubes.



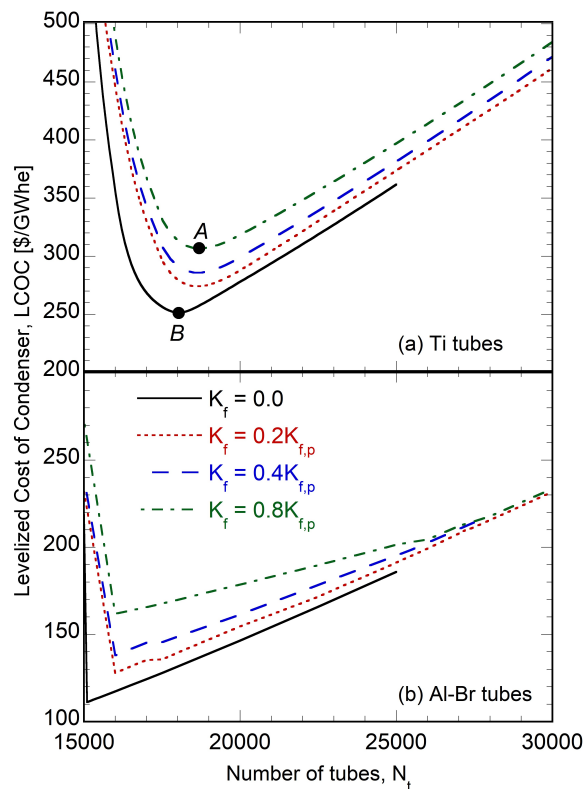
**Figure 7.** Influence of number of textured titanium tubes in the condenser on (a) net annual electric energy output from the plant and (b) number of plant outages for condenser cleaning and maintenance for various fouling rates. The default tube diameter is 0.025 m and cooling water velocity is 1.85 m/s.



**Figure 8.** Variation in levelized cost of condenser as a function of number of plain titanium tubes for various (a) cooling water velocity and (b) tube diameter. (c) Variation in levelized cost of condenser as a function of number of plain aluminum-brass (Al-Br) tubes for various cooling water velocity. The default tube diameter is 0.025 m and cooling water velocity is 1.85 m/s.

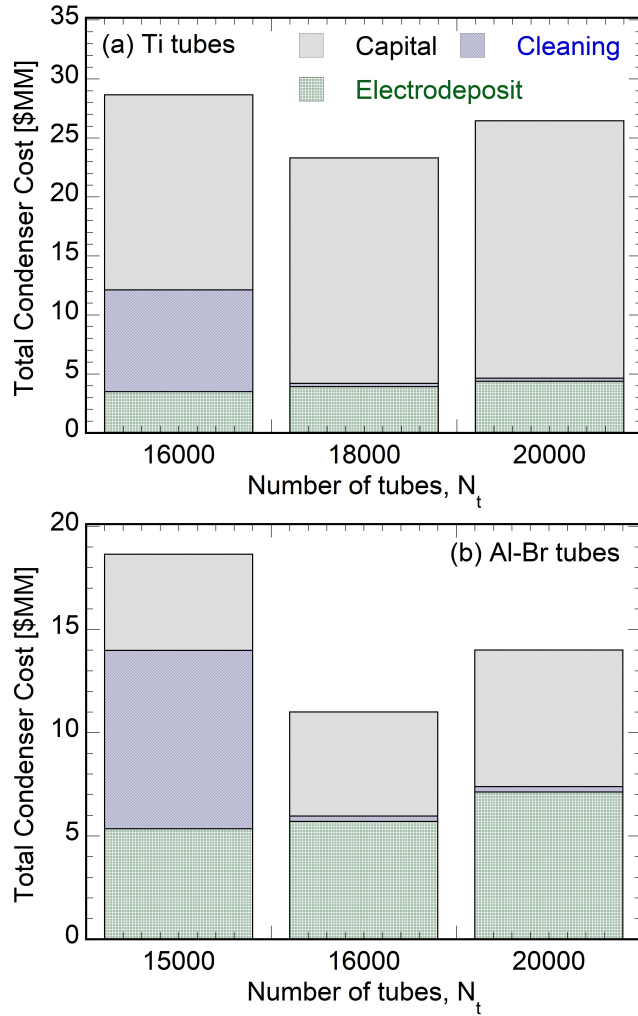
Figure 9a and b depicts the LCOC variations for textured tubes made of titanium and aluminum brass, respectively in enhanced condenser configuration. The tube diameter and cooling water velocity are kept fixed at 0.025 m and 1.85 m/s, respectively and the fouling rate ( $K_f$ ) is varied. Similar to the trends observed for baseline condenser with plain tubes (Fig. 8), there is an optimal number of tubes for different  $K_f$  values at which the minimum LCOC is obtained in Fig. 9. The fouling rate  $K_f = 0$  signifies the best-case

scenario and the lowest LCOC achieved are 250 \$/GWhe and 120 \$/GWhe for titanium and aluminum-brass tubes, respectively. As fouling rate decreases to  $K_f = 0$  the minimum LCOC as observed from Fig. 9a and b decreases due to lower overall thermal resistance for effective heat transfer between the cooling water and steam. In general, the minimum LCOC is achieved at smaller number of tubes for lower  $K_f$  values as observed from comparing the points 'A' and 'B' in Fig. 9a. The number of tubes corresponding to the minimum LCOC denoted by 'A' and 'B' in Fig. 9a decreases only slightly with decrease in  $K_f$  from  $0.8K_{f,p}$  to 0. This implies that the major contribution to the reduction in LCOC with decrease in fouling rate is the increase in plant net annual energy output due to improvement in condenser effectiveness and reduced number of plant outages and less effected by decrease in condenser capital cost. For instance, the annual net energy output for the design configuration referenced by points 'A' and 'B' are 4714.7 GWhe and 4507.8 GWhe, respectively.



**Figure 9.** Variation in levelized cost of condenser for various fouling rate factors and number of textured tubes of material (a) titanium (Ti) and (b) aluminum-brass (Al-Br). The default tube diameter is 0.025 m and cooling water velocity is 1.85 m/s.

Figure 10a and b demonstrate the breakdown of the total cost of the enhanced condenser for a various number of textured tubes made of titanium and aluminum-brass, respectively. The plots correspond to the curve shown for the fouling rate,  $K_f = 0$  in Fig. 9. The breakdown shows the initial capital expenditure, cumulative cleaning cost, and cumulative electrodeposition cost for the system lifetime of 20 years. Comparing Fig. 10a and b, it is observed that the capital expense of condenser made of titanium tubes is higher compared to aluminum brass tubes. As the number of tubes increases, the cleaning cost contribution to the total condenser cost decreases for both tube materials. The cleaning cost is a function of number of outages and increasing the number of tubes increases the condenser effectiveness that leads to less plant annual outages. On the other hand, both the yearly recurring electrodeposition cost and the initial capital cost are a function of tube surface area which are observed to increase with increase in number of tubes. In the case of textured titanium tubes, the total cost decreases with increase in number of tubes from 16,000 to 18,000 due to decrease in cleaning cost and increases again with increase in number of tubes to 20,000 due to increase in capital cost and electrodeposition cost. This suggests an optimal cost-effective design at  $N_t = 16,000$  which matches with the minimum LCOC point observed for  $K_f = 0$  in Fig. 9a. Similar trend is observed for the aluminum-brass tubes in Fig. 10b. Due to the high capital cost of condenser with titanium tubes, the percentage contribution from the yearly recurring electrodeposition cost is only 16.8% of the total cost compared to 51.8% for aluminum-brass tubes. Nevertheless, due to the low overall cost of condenser with aluminum-brass tubes, the LCOC obtained for aluminum-brass tubes in Fig. 9b are lower than the values obtained for titanium tubes in Fig. 9a.



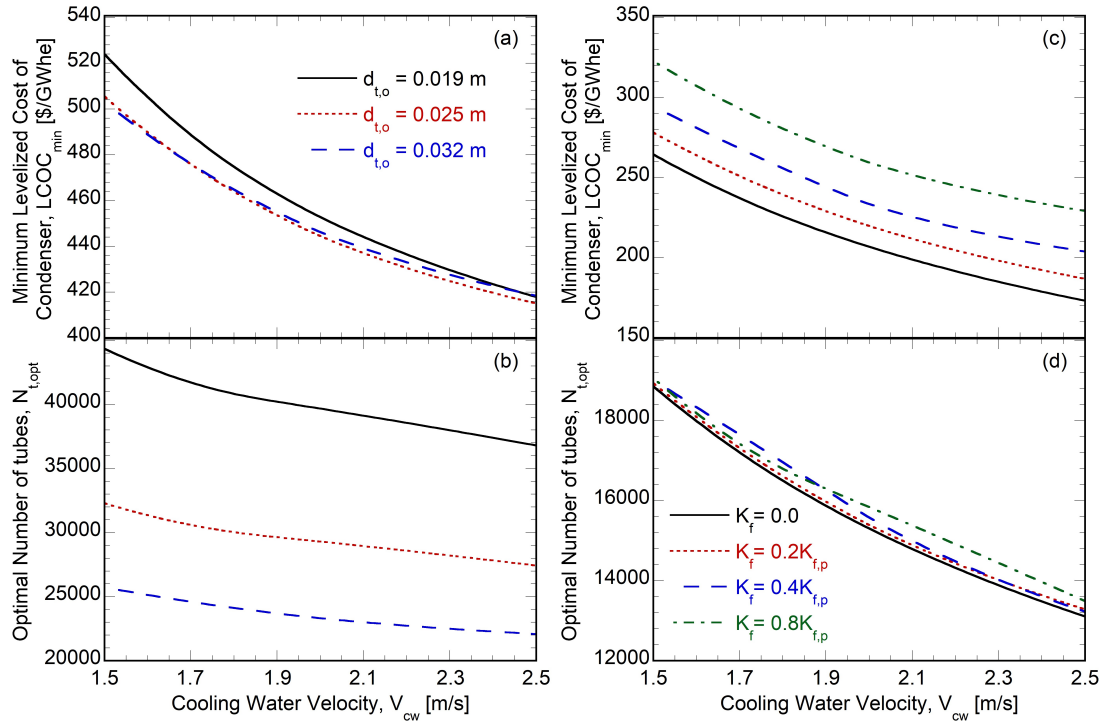
**Figure 10.** Breakdown of total condenser cost for various number of textured tubes fabricated by the electrodeposition process made of material (a) titanium (Ti) and (b) aluminum-brass (Al-Br).

Figure 11 illustrates the variation in minimum LCOC and the corresponding optimal number of tubes obtained from the parametric studies for various design and operating parameters. The results shown here are for titanium tubes and similar trends were obtained for aluminum-brass tubes. Figure 11a and b show the results obtained for the baseline condenser configuration with plain tubes. The minimum LCOC in Fig. 11a decreases with increase in cooling water velocity that follows the reduction in number of tubes corresponding to the minimum LCOC (Fig. 11b) and thus resulting in a lower capital cost investment. Since an increase in cooling water velocity increases the mass flow rate, the average cooling water temperature decreases resulting in lower turbine

backpressures and higher cycle efficiency. The resulting increase in efficiency with increase in cooling water velocity decreases the number of tubes or surface area requirement (Fig. 11b) for minimum LCOC. For instance, the net electricity generated for both  $V_{cw}$  of 1.5 m/s and 2.5 m/s and  $d_{t,o} = 0.025$  m is 4448 GWhe but the decrease in optimal number of tubes (Fig. 11b) leads to a reduction in the minimum LCOC (Fig. 11a). At lower cooling water velocity, the minimum LCOC is obtained for the largest diameter (Fig. 11a). This is attributed to the increase in filmwise condensation heat transfer coefficient as the number of tube rows decreases with increase in tube diameter for a fixed surface area. The net electricity generated for tube diameters of 0.019 m and 0.032 m at  $V_{cw} = 1.5$  m/s are 4450 GWhe and 4448 GWhe, respectively while the surface area corresponding to the optimal number of tubes shown in Fig. 11b decreases from 15,929 m<sup>2</sup> at  $d_{t,o} = 0.019$  m to 15,407 m<sup>2</sup> at  $d_{t,o} = 0.032$  m that reduces the capital cost and LCOC. At higher cooling water velocity, the increase in power cycle efficiency with increase in cooling water mass flow rate results the lowest LCOC obtained for smaller tube diameters that has lower capital cost (Fig. 11a). For all the cases in Fig. 11a and b, the number of annual plant outages was either 14 or 15.

Figure 11c and d illustrate the minimum LCOC and the corresponding optimal number of textured titanium tubes of diameter 0.025 m in enhanced condenser configuration for various fouling rates and cooling water velocities. Similar to the trends observed in Fig. 11a and b, the minimum LCOC and the corresponding optimal number of tubes decrease with increase in cooling water velocity. As expected the minimum LCOC is obtained for  $K_f = 0$  and increases with increase in the value of  $K_f$  (Fig. 11c). At higher cooling velocities, the optimal number of tubes shown in Fig. 11d increases with increase in fouling factor. At lower cooling velocities, the optimal number of tubes obtained for  $K_f = 0.8K_{f,p}$  is smaller than that obtained for  $K_f = 0.4K_{f,p}$  which can be explained by the trade-off between relative difference between the increase in electrodeposition reapplication cost and increase in net energy output with increase in number of tubes. Nevertheless, the decrease in minimum LCOC with decrease in fouling rate (Fig. 11c) is primarily due to the increase in annual net energy output. Compared to the minimum LCOC obtained for plain tubes in Fig. 11a, the minimum LCOC for textured tubes in Fig. 11c was considerably less due to the decrease in the capital cost

resulting from the reduction in number of tubes or surface area (compared Fig. 11d and Fig. 11c). The number of annual plant outages for textured tubes increased from 1 for  $K_f = 0$  to 14-15 for  $K_f = 0.8K_{f,p}$ .



**Figure 11.** Influence of cooling water velocity and tube diameter on (a) minimum leveled cost of condenser and (b) corresponding optimal number of plain titanium tubes. Influence of cooling water velocity and fouling rate factors on (a) minimum leveled cost of condenser and (b) corresponding number of textured titanium tubes. The default tube diameter is 0.025 m.

### 4.3.3 Numerical Optimization

The performance and cost models discussed in Section 2 were coupled with a numerical optimizer to determine the optimal design configuration that minimizes the LCOCC. The decision variables whose optimal values are sought to be determined are tube diameter, cooling water velocity, and number of tubes. The upper and lower bounds of the decision variables considered for the study are  $0.019\text{ m} < d_{t,o} < 0.032\text{ m}$ ,  $1.5\text{ m/s} < V_{cw} < 2.5\text{ m/s}$ ,  $N_t > 0$ . The optimization problem was solved using the Nelder–Mead simplex method [59]. The numerical optimization was conducted for both

titanium and aluminum-brass tubes in both baseline condenser (plain tubes) and enhanced condenser (textured tubes) configuration. As noted earlier, the baseline condenser configuration assumes filmwise condensation and  $K_f = K_{f,p}$ . In the case of textured tubes, the optimization simulations were done for different fouling rates with  $K_f$  varying between 0.0 to  $K_{f,p}$  in increments of  $0.2K_{f,p}$  while assuming the heat transfer coefficient corresponding to dropwise condensation (Eq. (7)) on the steam side. The dropwise heat transfer coefficient ( $h_{dwc}$ ) predicted by correlation provided by Griffith [16,46] in Eq. (7) is the maximum observed and other works in the literature [12] have reported values lower than that reported by Griffith [16,46]. To capture this variance, the optimization simulations were also performed for various multiplicative factors of  $h_{dwc}$ . For each optimization case, the runs were conducted using 10 different randomly chosen initial conditions on the decision variables to ensure that the optimum values reported are not local optima.

Figure 12 shows the numerical optimization results obtained for the objective of minimizing LCOC for both titanium and aluminum-brass tubes. The optimal cooling water velocity for both textured and plain tubes were obtained at the upper bound of 2.5 m/s since the surface area of the tubes required to meet the cooling load decreases with increase in cooling water velocity, which decreases the system cost. The inverse relation of filmwise condensation heat transfer coefficient to tube diameter favors smaller tube diameter while its inverse dependence on the number of tube rows favors larger tube diameters. Due to this contrasting effect, the optimal tube diameter was determined to be 0.025 m for the baseline condenser with plain tubes. The numerical optimizer predicted 0.032 m for enhanced condenser with textured tubes as dropwise condensation resistance decreases with increase in tube diameter. Figure 12a and b shows the minimum LCOC and the optimal number of tubes, respectively for titanium tubes. Compared to the LCOC of 415.1 \$/GWhe obtained for the baseline condenser with plain titanium tubes, the textured tubes show a considerable reduction (Fig. 12a). The variations in the minimum LCOC of textured tubes for various dropwise condensation heat transfer coefficient values are also shown in Fig. 12a. As expected, the minimum LCOC increases with decrease in  $h_c$  due to increase in condensation resistance. The optimal number of tubes for the baseline condenser with plain titanium tubes was obtained to be 27,437 while the

optimal number of tubes obtained for enhanced condenser with textured tubes for various fouling factor and condensation heat transfer coefficient values are shown in Fig. 12b. It is observed that the optimal number of tubes for textured titanium tubes reduces by more than half compared to plain tubes. Due to the high capital cost of titanium tubes compared to the recurring electrodeposition cost, texturing provides unequivocal advantage even if the textured tubes provide no fouling reduction while promoting dropwise condensation at lower heat transfer coefficient values due to reduction in tube surface area requirement ( $LCOC_{min}^* = 415.1$  \$/GWhe for plain tubes at  $K_f = K_{f,p}$  and  $h_c = h_{fwc}$  compared to  $LCOC_{min}^* = 285.8$  \$/GWhe for textured tubes at  $K_f = K_{f,p}$  and  $h_c = 0.1h_{dwc}$ ).

Figure 12c and d show the minimum LCOC and the optimal number of tubes, respectively obtained for aluminum-brass tubes from the numerical optimization study. The minimum LCOC for the baseline plain aluminum-brass tubes is 140 \$/GWhe (Fig. 12c) and the corresponding optimal number of tubes is 23,554. Depending on the fouling factor and condensation heat transfer coefficient values, the optimal number of textured tubes shown in Fig. 12d varies between 8,840 and 13,081. Due to the lower capital cost of aluminum brass tubes compared to titanium tubes, the percentage contribution of the recurring electrodeposition cost and the initial capital cost on the total system cost are nearly equal. Hence, the textured aluminum-brass tubes should achieve certain combination of condensation heat transfer coefficient improvement and fouling factor improvement so that they are cost competitive against plain tubes. The cost-competitive performance space for textured aluminum brass tubes is shown as shaded area in Fig. 12c. From Fig. 12c, it is observed that the aluminum-brass tubes should reduce the fouling factor to below 0.9 for  $h_c = h_{dwc}$  (point A in Fig. 12C) or 0.5 for  $h_c = 0.1h_{dwc}$  (point B) to be cost-competitive against the baseline condenser with plain aluminum-brass tubes.

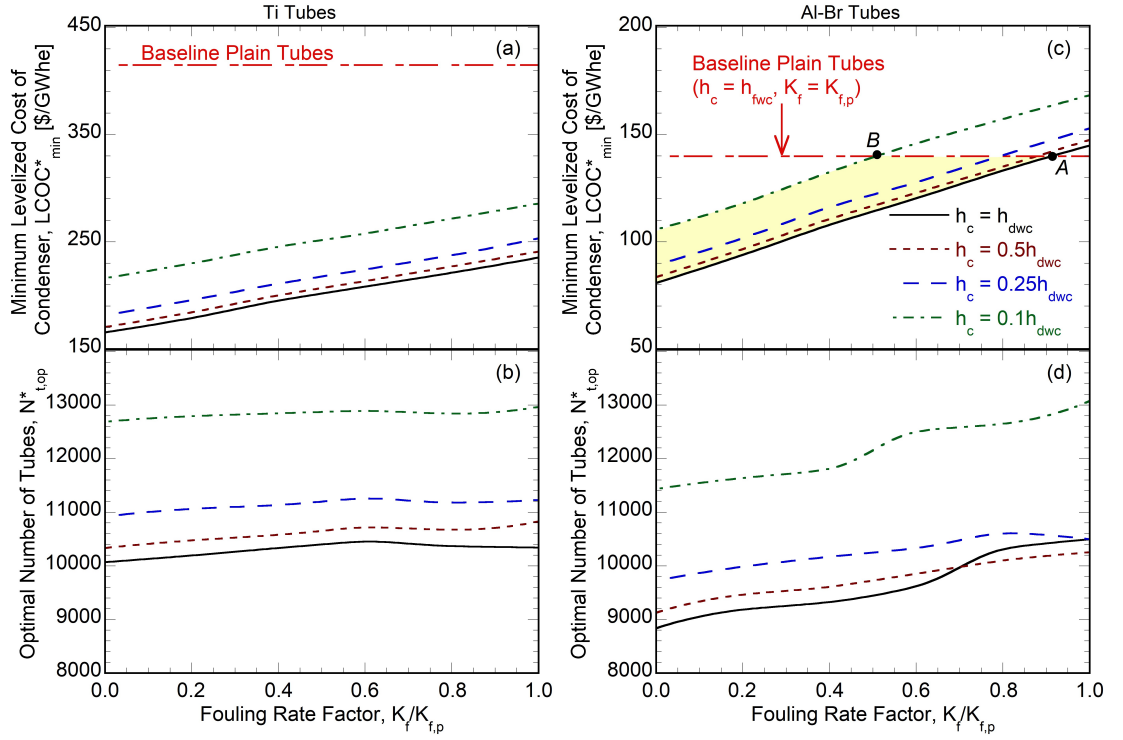


**Figure 12.** Variation in (a,c) minimum leveled cost of condenser and (b,d) optimal number of tubes obtained for titanium and aluminum-brass tubes from numerical optimization studies for various fouling rate factors and dropwise heat transfer coefficient values. The minimum leveled cost of condenser obtained for plain tubes is also shown. The shaded area in Fig. 12c denotes the cost-competitive performance space for textured aluminum-brass tubes.

A simple payback period based on  $N_{pb} = \frac{C_T}{Q_e \times C_{e,p} - C_M \times N_o - C_E \times Y}$  where  $C_{e,p}$  is the difference between the retail price of electricity (9.87 ¢/kWh) and cost of electricity production (6.84 ¢/kWh), the values for which were obtained from Walker et al. [19]. The definition for all the other variables that appear in the above equation can be found in Section 2.2. Based on the above definition, the payback period for the optimal baseline condenser (Fig. 12) with plain titanium and aluminum-brass tubes are 88 days and 29 days, respectively. The payback period for optimal enhanced condenser configurations (Fig. 12) with textured titanium tubes varied between 32 days obtained for  $h_c = h_{dwc}$ ,  $K_f = 0$  and 46 days obtained for  $h_c = 0.1h_{dwc}$ ,  $K_f = K_{f,p}$ . The corresponding values calculated for textured aluminum brass tubes are 9 days and 14 days. Future studies will focus on the investigation of time-dependent efficacy degradation of textured surfaces,

various fouling resistance evolution profiles corresponding to different water chemistry, and cooling water inlet temperature profile corresponding to different geographic locations on the system technoeconomics.

#### 4.4 Conclusions

An integrated thermal resistance network model was developed to study the annual performance of condenser with textured tubes fabricated using an electrodeposition process in thermoelectric power plant. The influence of time-dependent fouling resistance evolution, daily variations in cooling water inlet temperature, fouling rate, condenser tube diameter, cooling water velocity and number of condenser tubes for two different condenser tube materials (titanium and aluminum-brass) on the system performance were investigated. The condenser thermal performance model determined the daily variations in the steam condensing temperature or turbine backpressure and the net energy output for the above design and operating parameters. The constraint on the turbine backpressure or condensing steam pressure in the condenser established the number of plant outages required for condenser cleaning. The overall system performance was quantified in terms of net annual energy output and number of outages. A cost modeling tool and new levelized cost of condenser (LCOC) metric defined as the ratio of condenser lifetime cost to the total electric energy produced by the thermoelectric power plant was introduced. LCOC is a powerful tool to characterize and compare the feasibility of different condenser configurations for thermoelectric power generation applications. Higher cooling water flow rate and larger tube diameters increased the net annual energy output for textured tubes due to decrease in average turbine backpressure. There was an optimal tube count in the condenser that minimized the LCOC for various cooling water velocity and tube diameters.

Numerical optimization studies revealed that the minimum levelized cost of condenser was obtained for the upper bounds of cooling water velocity (2.5 m/s) and tube diameter (0.032 m) in the case of textured tubes that promote dropwise condensation. For plain tubes characterized by filmwise condensation, the optimal tube diameter was determined to be 0.025 m. The minimum LCOC for textured tubes was characterized for different multiplicative factors of the maximum possible dropwise heat transfer

coefficient and the fouling rate established for plain tubes. The optimal number of textured tubes required in the condenser for minimum LCOC was less by more than half compared to plain tubes. The minimum LCOC for condenser made of plain titanium tubes was 415.1 \$/GWhe compared to 140 \$/GWhe for aluminum-brass tubes. Since the capital cost of titanium tubes is high compared to the recurring electrodeposition cost, textured tubes provide considerable reduction in LCOC ranging between 165.8 \$/GWhe and 285.8 \$/GWhe for various combinations of fouling rate and dropwise heat transfer coefficient values. In the case of aluminum-brass tubes, texturing should reduce the fouling factor to below 0.9 and 0.5 for the highest and lowest dropwise condensation heat transfer coefficient values, respectively for it to be cost-competitive against optimal baseline condenser design with plain tubes. The best-case minimum LCOC for textured aluminum-brass tubes was obtained to be 80.9 \$/GWhe, which is reduction by more than half compared to plain tubes. Overall, the study serves as a design guideline for enhanced steam condenser with textured tubes.

#### 4.5 Nomenclature

|           |   |
|-----------|---|
| $a$       | constant                                      |
| $b$       | constant or wall thickness [m]                |
| $A$       | surface area [m <sup>2</sup> ]                |
| $c$       | specific heat [J/kg-K]                        |
| $C$       | cost [\$]                                     |
| $\dot{C}$ | cost per unit time [\$/h]                     |
| $\bar{C}$ | cost per unit mass [\$/kg]                    |
| $d$       | tube diameter [m]                             |
| $D$       | bundle diameter [m]                           |
| $E$       | electrostatic equivalent [g/A-h]              |
| $f$       | friction factor                               |
| $F$       | cost factor                                   |
| $HR$      | heat rate [kW <sub>t</sub> /kW <sub>e</sub> ] |

|                     |  |
|---------------------|--|
| $HR_c$              | heat rate correction factor                      |
| $h$                 | heat transfer coefficient                        |
| $I$                 | current intensity [ $A/m^2$ ]                    |
| $k$                 | thermal conductivity [ $W/m-K$ ]                 |
| $k_l$               | constant   |
| $K_f$               | fouling rate [ $W/m^2-K-day$ ]                   |
| $L$                 | length [m]                                       |
| $LCOC$              | levelized cost of condenser [ $$/GWh$ ]          |
| $\dot{m}$           | mass flow rate [kg/s]                            |
| $n_d$               | day number                                       |
| $N$                 | number count                                     |
| $N_y$               | system lifetime [years]                          |
| $p$                 | tube pitch [m]                                   |
| $P$                 | power [MW]                                       |
| $\Delta\mathcal{P}$ | frictional pressure drop [Pa]                    |
| Pr                  | Prandtl number                                   |
| $Q_e$               | annual electric energy output [GWhe]             |
| $\dot{Q}_c$         | cooling rate [MWt]                               |
| $R$                 | thermal resistance [K/W]                         |
| $R''$               | area-integrated thermal resistance [ $m^2-K/W$ ] |
| Re                  | Reynolds number                                  |
| $t$                 | time [day]                                       |
| $t_d$               | electrodeposition time per part [h/part]         |
| $t_s$               | labor set-up time per part [h/part]              |
| $T$                 | temperature [K]                                  |
| $U$                 | overall heat transfer coefficient [ $W/m^2-K$ ]  |
| $V$                 | velocity [m/s]                                   |
| $Y$                 | current yield                                    |

*Subscripts and Superscripts*

|             |   |
|-------------|---|
| <i>c</i>    | condensation                            |
| <i>cm</i>   | coating material                        |
| <i>cw</i>   | cooling water                           |
| <i>dwc</i>  | dropwise condensation                   |
| <i>f</i>    | foul                                    |
| <i>fc</i>   | forced convection                       |
| <i>fwc</i>  | filmwise condensation                   |
| <i>e</i>    | electric                                |
| <i>eq</i>   | equipment usage                         |
| <i>E</i>    | electrodeposition                       |
| <i>g</i>    | gas                                     |
| <i>HX</i>   | heat exchanger                          |
| <i>i</i>    | initial or inner or inlet               |
| <i>l</i>    | liquid or labor or length factor        |
| <i>lmtd</i> | Logarithmic Mean Temperature Difference |
| <i>m</i>    | material factor                         |
| <i>M</i>    | maintenance                             |
| <i>o</i>    | outages or outer or outlet              |
| <i>p</i>    | plain or pump                           |
| <i>pb</i>   | payback                                 |
| <i>r</i>    | rows                                    |
| <i>s</i>    | steam                                   |
| <i>t</i>    | tube                                    |

|     |               |
|-----|---------------|
| $T$ | total         |
| $w$ | wall          |
| *   | global optima |

### *Greek Symbols*

|               |   |
|---------------|---|
| $\gamma$      | reapplication interval [1/year]                           |
| $\varepsilon$ | effectiveness   |
| $\eta$        | efficiency  |
| $\lambda$     | latent heat of vaporization [kJ/kg]                       |
| $\lambda'$    | modified latent heat of vaporization [kJ/kg]              |
| $\mu$         | dynamic viscosity [Pa-s]                                  |
| $\Pi$         | turbine back pressure or steam condensation pressure [Pa] |
| $\rho$        | density [kg/m <sup>3</sup> ]                              |
| $\infty$      | asymptotic  |

### *Acronyms*

|       |   |
|-------|---|
| DWC   | dropwise condensation                   |
| FWC   | filmwise condensation                   |
| LCOC  | levelized cost of condenser             |
| NCG   | non-condensable gas                     |
| SHS   | superhydrophobic surface                |
| SLIPS | slippery liquid infused porous surfaces |

## 4.6 References

1. Pan, S.Y., Snyder, S.W., Packman, A.I., Lin, Y.J. and Chiang, P.C., 2018. Cooling water use in thermoelectric power generation and its associated challenges for addressing water-energy nexus. *Water-Energy Nexus*, 1(1), pp. 26-41.
2. Nowling, U., 2015. Best Practices for Maximizing Condenser Efficiency. *Power*, 159(5), pp. 56-58.
3. Miljkovic, N. and Wang, E.N., 2013. Condensation heat transfer on superhydrophobic surfaces. *MRS bulletin*, 38(5), pp. 397-406
4. McNeil, D.A., Burnside, B.M. and Cuthbertson, G., 2000. Dropwise condensation of steam on a small tube bundle at turbine condenser conditions. *Experimental Heat Transfer*, 13(2), pp. 89-105.
5. Dietz, C., Rykaczewski, K., Fedorov, A.G. and Joshi, Y., 2010. Visualization of droplet departure on a superhydrophobic surface and implications to heat transfer enhancement during dropwise condensation. *Applied physics letters*, 97(3), p. 033104.
6. Shen, J., Ming, P., Zhang, X., Yan, L., Zheng, X. and Wang, W., 2019. Broad Spectrum Anti-Fouling, Photocatalytic Antibacterial and Superamphiphobic Coating Fabricated by Composite Electrodeposition Process. *Journal of The Electrochemical Society*, 166(16), p. E564.
7. Daniel, D., Mankin, M.N., Belisle, R.A., Wong, T.S. and Aizenberg, J., 2013. Lubricant-infused micro/nano-structured surfaces with tunable dynamic omniphobicity at high temperatures. *Applied Physics Letters*, 102(23), p. 231603.
8. Tesler, A.B., Kim, P., Kolle, S., Howell, C., Ahanotu, O. and Aizenberg, J., 2015. Extremely durable biofouling-resistant metallic surfaces based on electrodeposited nanoporous tungstite films on steel. *Nature communications*, 6(1), pp. 1-10.
9. Daniello, R.J., Waterhouse, N.E. and Rothstein, J.P., 2009. Drag reduction in turbulent flows over superhydrophobic surfaces. *Physics of Fluids*, 21(8), p. 0851.
10. Ölçeroğlu, E. and McCarthy, M., 2016. Self-organization of microscale condensate for delayed flooding of nanostructured superhydrophobic surfaces. *ACS applied materials & interfaces*, 8(8), pp. 5729-5736.

11. Zhang, P. and Lv, F.Y., 2015. A review of the recent advances in superhydrophobic surfaces and the emerging energy-related applications. *Energy*, 82, pp. 1068-1087.
12. Enright, R., Miljkovic, N., Alvarado, J. L., Kim, K., & Rose, J. W. (2014). Dropwise condensation on micro-and nanostructured surfaces. *Nanoscale and Microscale Thermophysical Engineering*, 18(3), pp. 223-250.
13. Anand, S., Paxson, A.T., Dhiman, R., Smith, J.D. and Varanasi, K.K., 2012. Enhanced condensation on lubricant-impregnated nanotextured surfaces. *ACS nano*, 6(11), pp. 10122-10129.
14. Rose, J.W., 2002. Dropwise condensation theory and experiment: a review. *Proceedings of the Institution of Mechanical Engineers, Part A: Journal of Power and Energy*, 216(2), pp. 115-128.
15. Carey, Van P. *Liquid-vapor phase-change phenomena: an introduction to the thermophysics of vaporization and condensation processes in heat transfer equipment*. CRC Press, 2020.
16. Griffith, P. and Lee, M.S., 1967. The effect of surface thermal properties and finish on dropwise condensation. *International Journal of Heat and Mass Transfer*, 10(5), pp. 697-707.
17. Sparrow, E.M. and Lin, S.H., 1964. Condensation heat transfer in the presence of a noncondensable gas.
18. Ma, X., Wang, S., Lan, Z., Peng, B., Ma, H.B. and Cheng, P., 2012. Wetting mode evolution of steam dropwise condensation on superhydrophobic surface in the presence of noncondensable gas. *Journal of heat transfer*, 134(2).
19. Walker, M.E., Safari, I., Theregowda, R.B., Hsieh, M.K., Abbasian, J., Arastoopour, H., Dzombak, D.A. and Miller, D.C., 2012. Economic impact of condenser fouling in existing thermoelectric power plants. *Energy*, 44(1), pp. 429-437.
20. Zhang, H., Lamb, R. and Lewis, J., 2005. Engineering nanoscale roughness on hydrophobic surface—preliminary assessment of fouling behaviour. *Science and Technology of Advanced Materials*, 6(3-4), pp. 236-239.

21. Kim, D., Park, M., Park, J. and Hwang, W., 2009, May. Cell adherence and growth on a fabricated superhydrophobic surface. In 2009 IEEE International Conference on Computational Intelligence for Measurement Systems and Applications, pp. 230-233. IEEE.
22. Radwan, A.B., Abdullah, A.M. and Hassan, M.K., 2018. The missing piece of the puzzle regarding the relation between the degree of superhydrophobicity and the corrosion resistance of superhydrophobic coatings. *Electrochemistry Communications*, 91, pp. 41-44.
23. Feng, L., Yang, M., Shi, X., Liu, Y., Wang, Y. and Qiang, X., 2016. Copper-based superhydrophobic materials with long-term durability, stability, regenerability, and self-cleaning property. *Colloids and Surfaces A: Physicochemical and Engineering Aspects*, 508, pp. 39-47.
24. Lv, F.Y. and Zhang, P., 2016. Drag reduction and heat transfer characteristics of water flow through the tubes with superhydrophobic surfaces. *Energy Conversion and Management*, 113, pp. 165-176.
25. Enright, R., Eason, C., Dalton, T., Hodes, M., Salamon, T., Kolodner, P. and Krupenkin, T., 2006, January. Friction factors and Nusselt numbers in microchannels with superhydrophobic walls. In *International Conference on Nanochannels, Microchannels, and Minichannels (Vol. 47608)*, pp. 599-609.
26. Kant, K. and Pitchumani, R., 2020. Laminar Drag Reduction in Microchannels with Liquid Infused Textured Surfaces. *Chemical Engineering Science*, p. 116196.
27. Haghdoost, A. and Pitchumani, R., 2014. Fabricating superhydrophobic surfaces via a two-step electrodeposition technique. *Langmuir*, 30(14), pp. 4183-4191.
28. Haghdoost, A., Pitchumani, R. and Kargar, M., Virginia Tech Intellectual Properties Inc, 2015. Fabricating Porous Metallic Coatings Via Electrodeposition and Compositions Thereof. U.S. Patent Application 14/765,930.
29. Jain, R. and Pitchumani, R., 2017. Fractal model for wettability of rough surfaces. *Langmuir*, 33(28), pp. 7181-7190.
30. Teshima, K., Sugimura, H., Inoue, Y., Takai, O. and Takano, A., 2005. Transparent ultra water-repellent poly (ethylene terephthalate) substrates

- fabricated by oxygen plasma treatment and subsequent hydrophobic coating. *Applied Surface Science*, 244(1-4), pp. 619-622.
31. Thieme, M., Frenzel, R., Schmidt, S., Simon, F., Hennig, A., Worch, H., Lunkwitz, K. and Scharnweber, D., 2001. Generation of ultrahydrophobic properties of aluminium-A first step to self-cleaning transparently coated metal surfaces. *Advanced engineering materials*, 3(9), p. 691.
  32. Ebert, D. and Bhushan, B., 2012. Durable Lotus-effect surfaces with hierarchical structure using micro-and nanosized hydrophobic silica particles. *Journal of colloid and interface science*, 368(1), pp. 584-591.
  33. Li, G., Wang, B., Liu, Y., Tan, T., Song, X., Li, E. and Yan, H., 2008. Stable superhydrophobic surface: fabrication of interstitial cotton-like structure of copper nanocrystals by magnetron sputtering. *Science and technology of advanced materials*, 9(2), p. 025006.
  34. Jain, R. and Pitchumani, R., 2018. Fabrication and characterization of zinc-based superhydrophobic coatings. *Surface and Coatings Technology*, 337, pp.223-231.
  35. Jain, R. and Pitchumani, R., 2017. Facile fabrication of durable copper-based superhydrophobic surfaces via electrodeposition. *Langmuir*, 34(10), pp. 3159-3169.
  36. Anozie, A.N. and Odejebi, O.J., 2011. The search for optimum condenser cooling water flow rate in a thermal power plant. *Applied Thermal Engineering*, 31(17-18), pp. 4083-4090.
  37. Wang, W., Zeng, D., Liu, J., Niu, Y. and Cui, C., 2014. Feasibility analysis of changing turbine load in power plants using continuous condenser pressure adjustment. *Energy*, 64, pp. 533-540.
  38. Saari, J., Kaikko, J., Vakkilainen, E. and Savolainen, S., 2014. Comparison of power plant steam condenser heat transfer models for on-line condition monitoring. *Applied thermal engineering*, 62(1), pp. 37-47.
  39. Li, J., Zhai, Z., Wang, J. and Huang, S., 2016. On-line fouling monitoring model of condenser in coal-fired power plants. *Applied Thermal Engineering*, 104, pp. 628-635.

40. Laskowski, R., Smyk, A., Rusowicz, A. and Grzebielec, A., 2020. A useful formulas to describe the performance of a steam condenser in off-design conditions. *Energy*, p. 117910.
41. Laskowski, R., 2016. Relations for steam power plant condenser performance in off-design conditions in the function of inlet parameters and those relevant in reference conditions. *Applied Thermal Engineering*, 103, pp.528-536.
42. Pattanayak, L., Padhi, B.N. and Kodamasingh, B., 2019. Thermal performance assessment of steam surface condenser. *Case Studies in Thermal Engineering*, 14, p. 100484.
43. Dittus, F.W. and Boelter, L.M.K., 1930. University of California publications on engineering. *University of California publications in Engineering*, 2, p. 371.
44. Bergman, T.L., Incropera, F.P., DeWitt, D.P. and Lavine, A.S., 2011. *Fundamentals of heat and mass transfer*. John Wiley & Sons.
45. Coulson, J.M., Sinnott, R.K. and Richardson, J.F., 1983. *An introduction to chemical engineering design (Vol. 6)*. Elsevier Science & Technology.
46. Griffith, P., 1983. Dropwise condensation. *Heat exchanger design handbook*, 2, p. 5.
47. Nebot, E., Casanueva, J.F., Casanueva, T. and Sales, D., 2007. Model for fouling deposition on power plant steam condensers cooled with seawater: Effect of water velocity and tube material. *International Journal of Heat and Mass Transfer*, 50(17-18), pp. 3351-3358.
48. Zhang, H., Lamb, R. and Lewis, J., 2005. Engineering nanoscale roughness on hydrophobic surface—preliminary assessment of fouling behaviour. *Science and Technology of Advanced Materials*, 6(3-4), pp. 236-239.
49. Zhang, X., Wang, L. and Levänen, E., 2013. Superhydrophobic surfaces for the reduction of bacterial adhesion. *Rsc Advances*, 3(30), pp. 12003-12020.
50. Ferrari, M. and Benedetti, A., 2015. Superhydrophobic surfaces for applications in seawater. *Advances in colloid and interface science*, 222, pp. 291-304.
51. Webb, R.L., 2011. Enhanced condenser tubes in a nuclear power plant for heat rate improvement. *Heat transfer engineering*, 32(10), pp. 905-913.

52. Clamond, D., 2009. Efficient resolution of the Colebrook equation. *Industrial & Engineering Chemistry Research*, 48(7), pp. 3665-3671.
53. Feng, Y. and Rangaiah, G.P., 2011. Evaluating capital cost estimation programs. *Chemical Engineering*, 118(8), pp. 22-29.
54. Sieder, W.D., Seader, J.D. and Lewin, D.R., 2004. *Product and process design principles: synthesis*. John Wiley & Sons.
55. Putnam, R.E. and Putman, R.E., 2001. *Steam Surface Condensers: Basic Principles, Performance Monitoring, and Maintenance*. Amer Society of Mechanical.
56. Mazzilli, A., Lenau, T. *Electroplating Costs Calculation*. Available at: <http://polynet.dk/ingpro/surface/elecomk.htm> (Accessed: July 6, 2020).
57. Van Rossum, G. & Drake Jr, F.L., 1995. *Python reference manual*, Centrum voor Wiskunde en Informatica Amsterdam.
58. Thulukkanam, K., 2013. *Heat exchanger design handbook*. CRC press.
59. Nelder, J.A. and Mead, R. A simplex method for function minimization. *The computer journal*, 7(4), pp. 308-313.

## Chapter 5. Conclusions and Future Work

Nonwetting surfaces offer a variety of features with exceptional application opportunities such as drag reduction, fouling reduction, corrosion resistance, anti-fogging, anti-icing, and condensation enhancement. There has been considerable interest and research in the fabrication of these surfaces during the last decade leading to substantial advancements in this field. However, further in situ testing is required to ensure the performance of these surfaces in the actual desired environment. Also, to evaluate the capabilities of the proposed surface, systematically standardized testing processes should be developed to measure the durability and performance of these surfaces.

In this study, the recent advancements and researches about nonwetting surface features have been reviewed. To establish how realistically these features could enhance the real-life applications a thermo-economic performance model was developed for a powerplant condenser. The influence of using textured tubes on the plant's performance and its economy was investigated. A cost modeling tool and new levelized cost of condenser (LCOC) metric defined as the ratio of condenser lifetime cost to the total electric energy produced by the thermoelectric power plant was introduced. The common condenser tubes are modified through a simple, scalable, and cost-effective electrodeposition process to achieve textured tubes with superhydrophobic properties. Taking in to account the promising characteristics of these SHS, it was shown that for the best-case condensers with textured tubes could reduce the optimal number of textured tubes required for minimum LCOC by more than half compared to plain tubes. Also, the minimum LCOC for a condenser made of textured tubes was considerably lower than the case for plain tubes demonstrating a promising opportunity for the application of nonwetting surfaces in power plants' condensers.

In addition to heat transfer area reduction, the textured tubes have the potential to decrease the pump work due to the drag reduction feature of the surface. Also, the textured surface could promote corrosion resistance properties of the tubes lowering the plant's maintenance costs. Although, these features present a lower order of overall enhancement for plants' economy in comparison with the influence of enhanced condensation heat transfer and fouling reduction.

Future studies to expand the developed technoeconomic model in this project will focus on the investigation of time-dependent efficacy degradation of textured surfaces, various fouling resistance evolution profiles corresponding to different water chemistry, and cooling water inlet temperature profile corresponding to different geographic locations on the system technoeconomics.

Moreover, the established methodology for the technoeconomic evaluation of nonwetting surfaces in this study could be implemented in other applications such as water distillation systems or HVAC systems to investigate the real significance of implementing these surfaces.